Drill – Drive Installation of Monopile in Rock by using the Monopile as Casing

MSc Thesis

Georgios Kleisiaris

TU Delft

Van Oord
Marine ingenuity

Drill – Drive Installation of Monopile in Rock by using the Monopile as Casing

by

Georgios Kleisiaris

in partial fulfilment of the requirements for the degree of

MSc Civil Engineering

Track: Structural Engineering

at the Delft University of Technology

April, 2022

University Supervisors: Prof. dr. M. Veljkovic
Dr. F. Kavoura
Dr. P.C. Meijers
Van Oord Supervisor: Ir. R.J.N.J. Luiken

TU Delft

Van Oord
Marine ingenuity

Abstract

The need for sustainable solutions in the energy sector has led to the rapid increase of windfarms around the globe. The areas with ideal soil conditions are gradually being occupied, pushing the offshore wind industry to search for methods of installing wind turbines in hard terrain. So far, the installation of monopiles in weak rock, if successful, required the use of additional casings and grouting. In this thesis project, an alternative installation method is investigated, in which the monopile itself is used as casing, avoiding the waste of extra material.

The 'drill-drive' installation method under investigation consists of an initial drill-out of the rock from the inside of the pile and its subsequent driving into the seabed with a hydraulic hammer. No casing is used and a cutting toe is equipped in the bottom circumference of the pile, being responsible for breaking through the rock. The feasibility of the proposed method is evaluated for a seabed made of granite, limestone or sandstone. Shock resisting steel and cemented carbide were considered as possible materials for the toe and a diameter-over-thickness ratio of 100 was chosen for the monopile of S355 steel grade.

Finite element analysis is used in order to investigate the structural integrity both of the monopile and the toe during the 'drill-drive' process. Failure of the toe is proven to be the probable cause for an unsuccessful termination of the operation. According to a wear propagation analysis, cemented carbide can be utilised for preventing catastrophic damage to the cutting toe. On the other hand, the monopile appears to have sufficient resistance, without experiencing instability or excessive deformation.

A driveability analysis was conducted, which showed that granite and limestone rock properties are unfavourable for the proposed installation method, resulting in premature driving refusal. However, the embedment of the monopile in the desired depth is possible in weak sandstone, deeming the drill-drive installation by using the monopile as casing successful. A cost analysis should be made, in order to ensure that the final solution proposal can be utilised in real practice.

A number of assumptions were made throughout the research, defining the boundaries of the conclusions. More specifically, the detailed fracture analysis of rock is out of the scope of this thesis. More elaborated simulation techniques and on-site testing are recommended for the realistic representation of the toe-rock interaction. Finally, the response of the monopile was determined using static analysis. A dynamic analysis could provide more accurate results and is left for future research.

Acknowledgements

Reaching the end of my educational path, I am keeping both the good and bad moments, and definitely the valuable lessons I acquired throughout this journey. From a curious teenager that wanted to be an engineer, to a master's degree holder in structural engineering, things definitely did not come easy. However, the ups and downs throughout this process shaped my personality and who I am today, and I would not wish to have it another way. Of course, none of these would be possible without the help and support of the people around me.

I want to sincerely thank Ralph Luiken and Ferdy Hengeveld for putting their trust in me, allowing me to work on this thesis topic and welcoming me in their team in Van Oord. Working on this research project solidified my interest in offshore engineering and now, more than ever, I am ready to become an active part of this industry. Something that I am grateful for. Specifically to Ralph, thank you for the guidance, the insightful weekly meetings and the support throughout this thesis. Realising this project would not be possible without your help.

Also, I want to express my gratitude towards my TU Delft committee. A big thank you to Prof. dr. M. Veljkovic for accepting to supervise me in this project and for being always open to my questions. Your advice in the kick-off meeting to start simple and build up in complexity was crucial for finding the right path in a rather disappointing start in this project. A very special thank you to Dr. F. Kavoura for the guidance and for always finding the time for a progress meeting. Your support, both mental and scientific, was more than important to me. Finally, thank you Dr. P.C. Meijers for agreeing to be part of this committee without a hint of hesitation. Although the dynamic part of the thesis came to be really limited, I hope the project was interesting for you.

A big thank you to Karel Karsen, study advisor at TU Delft, for listening to what I had to say and helping me reach my goal of obtaining this degree.

I could not leave my friends out of this thanking note. To the Simons people, thank you for the two years that I will always remember. To Camera, your support has been incredible, thank you. To the Greek crew, thank you for everything, you made being away from home really easier. A special thank you also to my friends back in Greece, who were always there to hear me complain and lift me up.

Most importantly, I cannot express in words how grateful I am to my family. Eleni, keep going. My lovely parents, thank you all these years for your unconditional support, allowing me to make my dreams come true.

Georgios Kleisiaris
Delft, April 2022

Table of Contents

Terminology and Abbreviations

The terms ‘rock breaking’ and ‘rock cutting’ are used interchangeably.

The terms ‘cutting toe’ and ‘toe’ are used interchangeably.

The terms ‘rake angle’ and ‘cutting angle’ are used interchangeably.

The terms ‘monopile’ and ‘pile’ are used interchangeably.

‘FEM’ refers to finite element modelling, ‘FE’ refers to finite element and ‘FEA’ refers to finite element analysis.

‘GMNIA’ refers to geometric and material nonlinear analysis with imperfections included.

‘EDP’ refers to the Extended Drucker Prager yield criterion.

‘MPS’ refers to the Maximum Principal Stress theory.

The drill-drive installation method by using the monopile as casing is mentioned as ‘drill-drive installation’ in the upcoming chapters.

The nodes that come in contact between the tip of the cutting toe and the rock surface below it, as the toe is pressed into the rock, are designated as ‘indentation point’.

List of Symbols

Symbol	**Description**
Greek	
α	cutting angle
α_b	Biot constant
A	cross-section area
β	shear breaking angle
γ_M	material partial factor
ε	strain
ε_d	distributed damping coefficient
E	Young’s Modulus
Z	pile impedance
Z_w	depth under water
ν	Poisson’s ratio
ρ_b	bulk density of rock
ρ_{ma}	solid density of rock
σ	stress
σ_1	maximum principal stress
σ_3	minimum principal stress
σ_v	Von mises stress
σ_c	compressive strength
σ_t	tensile strength
τ_0	Shear strength
σ_m	hydrostatic mean stress

σ_{cr}	Critical buckling stress
φ	friction angle between rock and tool
φ_p	porosity

Latin

c	wave speed
C_w	rock cohesion under water
C	rock cohesion
D	pile diameter
f_y	yield strength
F_c	rock cutting force according to Evans
i	rock internal friction angle
I	section inertia of pile
k_d	distributed spring stiffness coefficient
l	pile length
I_1	first invariant of the Cauchy stress
J_2	second invariant of the deviatoric part of the Cauchy stress
p	water pressure
r	pile radius
t	pile wall thickness
T_0	tensile strength of rock
UCS_w	uniaxial compressive strength of rock under water
UCS	uniaxial compressive strength of rock

1 Introduction

1.1 Current Practice & Motivation

Pile tip damage has already been documented for various offshore projects in Australia, the North Sea and the Netherlands (Great Britain. Health and Safety Executive. & MSL Engineering., 2001; Randolph, 2018). Even with a diameter to wall thickness ratio as small as 40, open-ended piles have been proven to be prone to tip buckling when hard soil or weak rock is encountered during driving. The asymmetrical response of stratified soil sediments was found to exaggerate this instability that the pile experiences (Jafari et al., 2019; York, n.d.). In some cases, the inwards distortion of the tip has led to premature driving refusal and immediate termination of the installation operation. Even more dangerous can be the case of an undetected, during the installation, damage in the pile (Randolph, 2018). The latter would cause the in-service performance to deteriorate significantly and unwanted implications to come in light long after the installation process is finished. Design codes do not include regulations and guidelines for analysing the response of a tubular pile in hard rock driving conditions, imposing another obstacle in offshore monopile installation of such nature (R. F. Stevens & Westgate, 2019). For the reasons mentioned above, it is of great importance to extend the research on pile driving in rock and develop tools that would enable the engineers to predict the possible failure on monopiles during an offshore installation in rock.

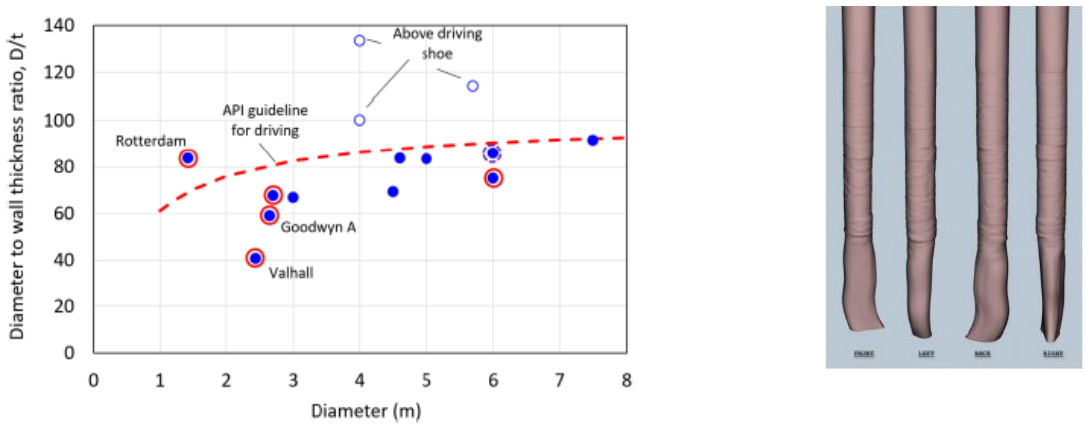

(a) (b)

Figure 1.1: Documented projects where pile tip extrusion buckling occurred (a). Pile tip buckling modes (b). ***(Randolph, 2018)***

In the offshore industry, installation of monopiles is currently done in sandy soils and clay. Rarely, drilling operations have been used for the penetration in soft rocks (Spagnoli & Weixler, 2013), mainly for jacket pin piles. In these operations, a hole is drilled in the seabed with a slightly bigger diameter than the monopile. The drilling equipment is mounted on a floating platform or vessel and performs the operation by imposing both torque and vertical forces to the rock. A casing is used for preventing the rock material from falling inside the borehole. The drill is placed inside the casing and underreams the casing shoe until the desired penetration depth. The cut rock chips are removed using air or water ejectors or mud circulation techniques. Then, the drill is removed, the monopile is placed in the casing and the void between them is grouted (Spagnoli & Weixler, 2013).

Most of the times the casing is left behind in the seabed. This procedure involves additional costs because of the use of the casing and grout, making it a less efficient installation method, especially when a bigger penetration depth is required.

An installation method that does not result in waste of materials is investigated in this research project. It will be referred to as 'drill-drive monopile installation in rock using the monopile as casing'.

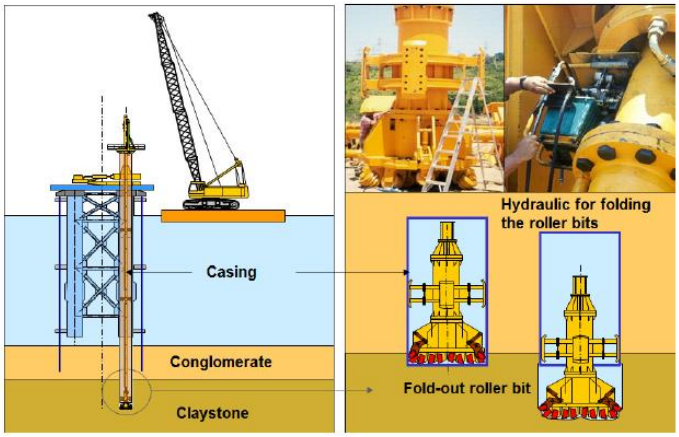

Figure 1.2: Drill operation scheme for offshore pile installation. ***(Spagnoli & Weixler, 2013)***

1.2 Drill-Drive Monopile Installation by using the Monopile as Casing

The procedure of drill-drive installation in rock using the monopile as casing is a novel method that has not been studied or used before. A drill is placed inside the monopile and drills out the rock from the internal diameter up to a certain depth. That means that a ring of rock material, with thickness equal to the pile shell thickness (t), remains intact below the monopile foundation. The rock fragments from the drilling operation are assumed to get removed by an appropriate air lift system to avoid causing a soil plug.

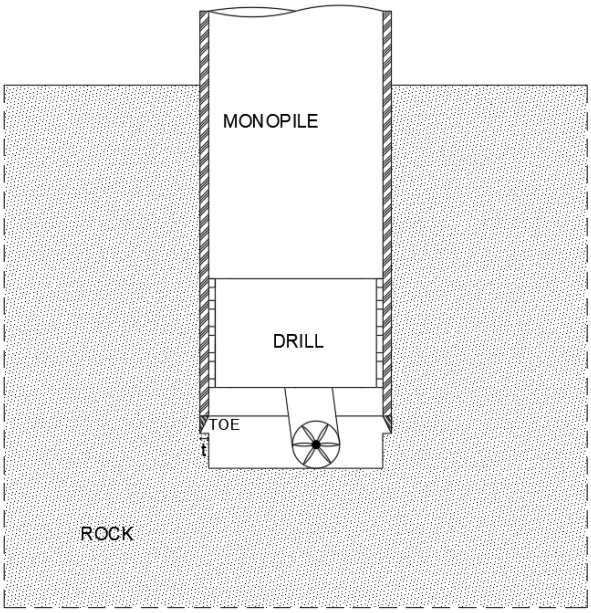

Figure 1.3: Borehole drilling as part of the Drill-Drive installation using the monopile as casing.

Then, with the use of a hydraulic hammer the monopile is driven through the rock, breaking the remaining rock material below the pile rim. For that to be feasible, a cutting toe is equipped in the bottom of the monopile. The drilling succeeds the driving, and the procedure is continued in a recursive manner until the desired penetration depth is reached.

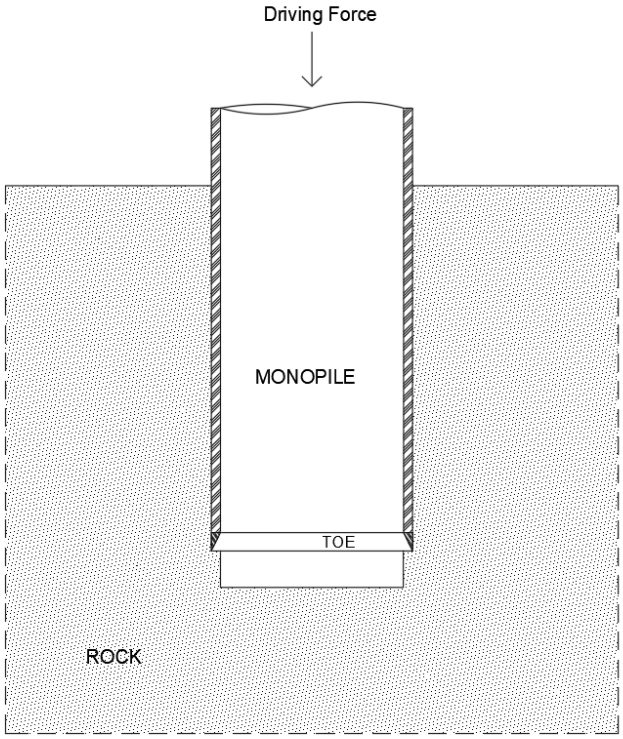

Figure 1.4: Driving the monopile in rock.

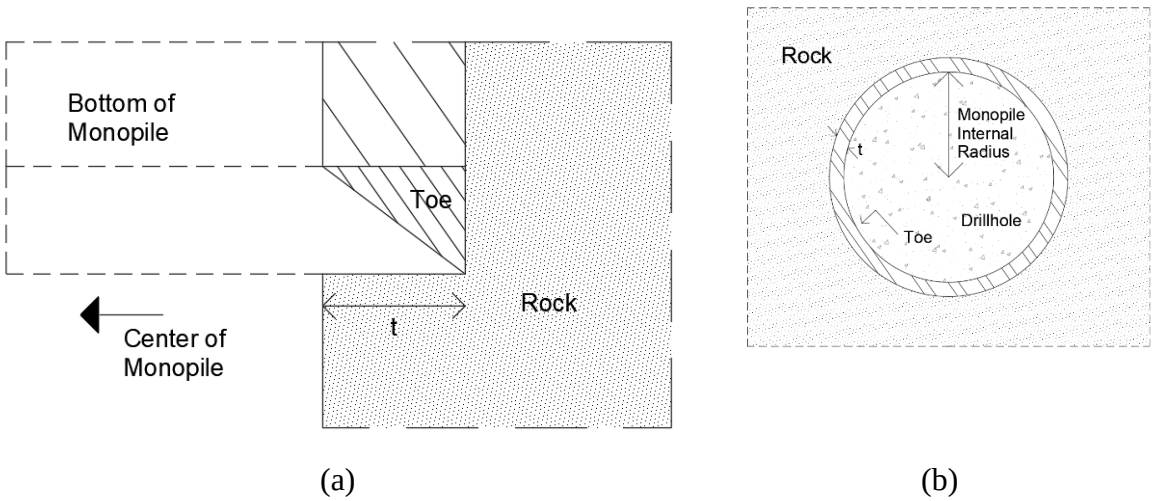

Figure 1.5: Cross-section of the continuous cutting toe (a). Plan view of the continuous cutting toe (b).

1.3 Scope of the Thesis & Research Goals

The MSc Thesis focuses on the feasibility study of the installation method described in chapter 1.2. The installation operation will not be successful if the desired penetration depth is not reached. To determine a premature driving refusal, a driveability analysis is carried out. The inability to embed the pile in the desired depth is a result of the damage to the monopile structure or the cutting toe. Therefore, the structural integrity of both is investigated by numerical simulation of the cutting toe-rock interaction and the monopile's stability. A link of the toe damage and its cutting performance is created. The pile and toe failure are judged to be the critical parts of a drill-drive installation. Other sources of failure are not investigated, e.g. borehole instability, weld failure, fatigue damage.

The cutting toe-rock interaction is investigated taking into consideration the most important parameters that the existing literature has to suggest. The detailed modelling of the rock mass response is out of the scope of this thesis. Discontinuities and micro-cracks in its structure are not included in the rock model. Instead, homogeneous, isotropic properties are assumed and the crack propagation in failure is not attempted to be predicted realistically.

The main research question that will be answered in this research project is:

Can a drill-drive operation, using the monopile as casing, be used for the successful completion of an offshore monopile installation in rock?

Other research questions that will be addressed are:

What is the potential damage to the monopile, as a result of the drill-drive installation in rock?

What are the main parameters influencing the cutting performance of the cutting toe?

What is the maximum penetration depth using a drill-drive installation, for different types of rock and level of wear on the cutting toe?

1.4 Research Approach

The answer to the research questions will be searched by following the research approach below:

1. Understand the pile driving mechanism, the rock cutting mechanics and the potential monopile deformations through literature study.
2. Get familiar with Finite Element analysis through self-study, the available ANSYS tutorials and ANSYS help manual and by consulting the employees of Van Oord.
3. Investigate the rock cutting performance of the toe by performing numerical simulation on models with different cutting angles and rock properties.
4. Investigate the pile damage during the drill-drive installation by performing static FEA of the monopile foundation, considering the rock-structure interaction, the rock resistance in breaking and material and geometric non-linearities.
5. Investigate the wear on the cutting toe for different rake angles by performing FEA and using the appropriate material law.
6. Perform a driveability analysis for determining the maximum penetration depth that can be reached in seabed of different rock properties.
7. Reach conclusions by critically interpretating the results.

2 Literature Review

The literature study on installing monopiles offshore in rocky seabed yields one certain outcome, that there is a shortcoming of available literature or data for the installation of that nature. However, there is available literature for installation of (offshore) monopiles in sand, clay or chalk and in soil layers that contain weak rock, which can be used for spotting the critical parts for failure. Additionally, current regulations and codes do not provide guidelines for designing or analysing an installation of monopile in rock. The, highly probable, pile tip integrity concerns during driving in hard conditions are not covered either, falsely assuming that typical pile geometries would not create threats for the integrity of the pile tip (Great Britain. Health and Safety Executive. & MSL Engineering., 2001).

Regarding the installation in sand, clay or weak rock, the soil resistance is mobilised as skin friction resistance along the shaft of the pile and as base resistance in the bottom of the pile (Irvine et al., 2015). Analytical solutions can be found in literature for the soil resistance and force-displacement curves describing the response of the pile. Unfortunately, those curves cannot be utilised to a monopile driving analysis in rock, due to the uncertainty of the behaviour of the rock during that process.

Points of attention for the abovementioned cases would be the soil plug that is formed inside the monopile during the installation, the soil set-up and premature refusal that can be caused by either the soil plug or the extensive damage of the pile tip (R. S. Stevens, 1982). As mentioned in chapter 1.2, soil plug is out of the scope of this thesis, assuming that the successful removal of the shattered rock from drilling precedes the driving operation. Therefore, the main concern is focused on the integrity of the pile tip and is thoroughly analysed in the following chapters. It can be easily understood that an inadequacy in successfully breaking the rock also translates to premature driving refusal and failure of the installation process. Such is defined the second focus point of the thesis, that of succeeding in breaking the rock with the use of available toe materials and driving equipment. The literature study yielded once again that these are under-developed research topics.

The literature findings are not directly applicable to the project of this thesis. Knowledge from geology and the mining industry must be combined with findings from the installation of monopiles in hard soils for coming up with a solution to the problem of drill-drive installation of monopile in rock, using the monopile as casing. This thesis is regarded by the author as a first attempt in ‘testing the waters’ of such installation method, and therefore additional research should be followed.

2.1 Rock Mechanics

As many petrologists say, ‘seabed rocks can reveal Earth’s history’ (Hekinian, n.d.). Studying and understanding their origin, their process of formation and their geochemical and mineralogical evolution over the years, researchers can get a clearer view of the chronological and geological events that led to the formation of Earth’s crust the way we know it today. The relative movement of tectonic plates, the volcanic activity of the planet and the interference of water have created a petrological composition of the seabed consisting mainly of volcanic rocks (e.g., basalt, dolomites) and sedimentary rocks (e.g., sandstone).

It needs to be noted that the limited access to formations in greater depths creates an uncertainty in the observation of Earth's seabed petrological map (Hekinian, n.d.).

The density of the solid body and the density of pore fluids are the parameters that determine rock's bulk density, as shown in expression 2.1. Moreover, regarding underground rocks, the density increases with depth because the hydrostatic compression increases, reducing the level of saturation of rock (Peng & Zhang, n.d.).

$$\rho_b = (1 - \varphi_p)\rho_{ma} + \varphi_p \rho_f \qquad 2.1$$

The effect of depth is also depicted in the Poisson's ratio value of rock, with experiments yielding an empirical relationship that correlates the two. Again, the increased compaction at a greater depth below the seabed causes an increase in the rock mechanical properties (Peng & Zhang, n.d.).

$$v = 0.0582 \ln Z - 0.0174 \qquad 2.2$$

where, Z is the depth measured in meters

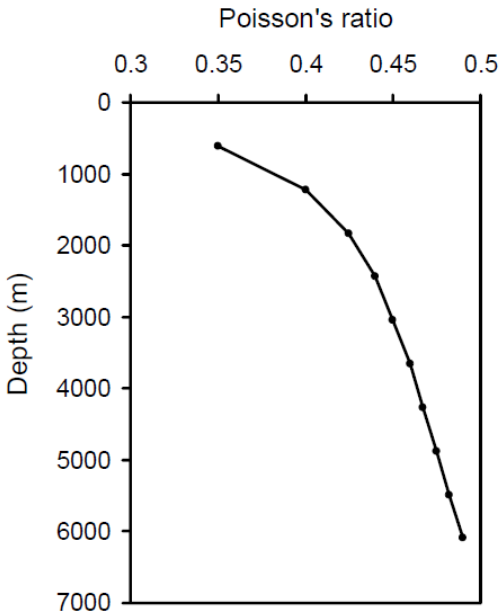

Figure 2.1: Poisson's ration vs depth from experiments in the Gulf of Mexico. ***(Peng & Zhang, n.d.)***

The most important parameters for the geo-mechanical analysis of rock are the uniaxial compressive strength (*UCS*), the rock cohesion (c) and the internal friction angle (φ) (Bilgin et al., n.d.; Peng & Zhang, n.d.). Most of the times these parameters are determined from in situ tests, but in the absence of those, empirical relationships can be used that are formulated for the different type of rocks. Moreover, the determination of the pore pressure is crucial for calculating the stresses and failure of rock and empirical models are suggested in the literature. The level of saturation of rock directly affects its mechanical behaviour. Due to its porosity, the effective stress should be used for the calculation of rock's behaviour under loading, by subtracting the fluid pressure from the total induced stress, taking into account that way that the solid and fluid part experience different levels of deformation.

The UCS of the rock is reduced due to the water pressure, with the following formula being recommended (Peng & Zhang, n.d.):

$$UCS_w = UCS - \frac{(2\alpha p * \sin\varphi)}{1 - sin\varphi} \quad 2.3$$

where, α is the Biot constant

The behaviour of rocks is by nature not linear. However, for most rocks the approximation of an elastic linear stress-strain curve before failure, namely $\sigma = E * \varepsilon$, is experimentally proven adequate. The dynamic Elastic Modulus can be calculated both experimentally and analytically, with the latter considering the compressional and shear wave velocities. The static modulus is mostly determined through experiments, preferably under triaxial stress state (Peng & Zhang, n.d.).

One of the most important characteristics of rock is its tendency to acquire higher strength as the confining pressure increases, meaning when it is subjected in three-dimensional compressive stress condition. Same follows for the Young's Modulus, for which non-linear experimental formulas have been proposed for the prediction of its increase with higher confinement. The failure type also depends on the confinement (fig. 2.2). For unconfined compression irregular splitting is observed, while for high confinement the rock behaves in ductile manner experiencing shear fractures and plastic deformation. Finally, for normal levels of confinement, regular shear failure occurs with a single plane of fracture, inclined by 45° in respect to the higher principal stress (Peng & Zhang, n.d.).

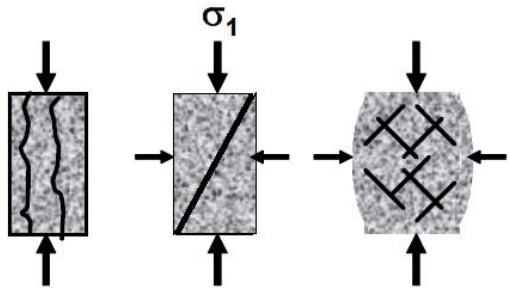

Figure 2.2: Failure of rock for different levels of confinement: splitting, shear failure, ductile failure (from left to right). ***(Peng & Zhang, n.d.)***

Although the behaviour of rock prior to failure can be adequately described with a linear stress-strain behaviour, the prediction of the behaviour of the rock mass post-failure is a rather complex one. For that responsible is the anisotropic, heterogeneous intrinsic nature of rocks and the discontinuities and 'web' of fractures that can be present in its structure. It is clear from experiments and observations that this fractured, discontinuous state of rock can have a significant impact in the strength analysis of rock masses and should be taken into account.

The Hoek Brown criterion (expression 2.4) is an empirical failure criterion that accounts for these discontinuities and is widely accepted in the industry. It is used for describing the failure of intact rock in rock excavation applications (Hoek & Brown, 1997). Additional modifications have been made that make it valid for the cases of jointed rock (Shah, 1992). The criterion contains parameters representing the quality of the intact rock and the in-situ mass under examination.

The former are the uniaxial compressive strength of rock and the material constant m, and the latter are the geological strength index (GSI) and the disturbance factor D:

$$\sigma_1' = \sigma_3' + UCS * \left(\frac{m\sigma_3'}{UCS} + s\right)^a \quad 2.4$$

where, a is a constant that depends on the rock mass characteristics

m, s are constants that depend on the rock properties and the quality of the rock

The constants of the Hoek Brown failure criterion can be determined as follows:

$$m = m_i * e^{\frac{GSI-100}{28-14D}} \quad 2.5$$

$$s = e^{\frac{GSI-100}{9-3D}} \quad 2.6$$

where, D is the disturbance factor, from 0 for undisturbed rock mass to 1 for heavily disturbed

GSI is the Geological Strength Index introduced by Hoek as determined from fig. 2.3

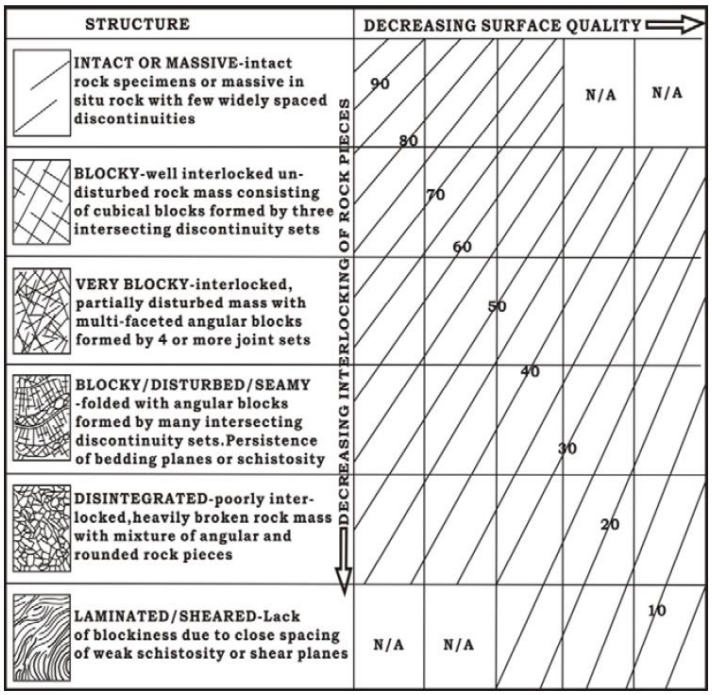

Figure 2.3: GSI values according to Hoek. ***(Shah, 1992)***

Although the Hoek – Brown failure criterion is implemented in commercial software used by geotechnical engineers, such as RockLab and PLAXIS, it is not yet available to most conventional FEM software and, therefore, classic stress failure criteria should be used for analysing the behaviour of rock in failure.

In the past, rock was assumed to behave in an elastic-brittle manner. Recent studies suggest that rock does exhibit limited plastic deformation prior to rupture and its failure can be described by the following stages (Bieniawski, 1967):

- *Crack Initiation*, meaning the formulation of cracks in a previously uncracked rock mass
- *Fracture Initiation*, which marks the start of crack expansion
- *Fracture Propagation*, which can be distinguished in stable and unstable. At a stable fracture propagation, the crack extension is a function of the loading and can be controlled and predicted. On the contrary, at the stage of unstable fracture propagation, cracks extend in a pattern and speed not only depending on loading but also other factors, making the fracture process uncontrollable.
- *Rupture*, namely the breaking of rock in pieces

According to Griffith, the pre-existing cracks in a material's structure will expand and propagate when the load application causes stresses that exceed the tensile strength at the tip of those cracks. The failure is expressed from the following formulas:

$$(\sigma_1 - \sigma_3)^2 = 8T_0(\sigma_1 + \sigma_3) \quad \text{for } \sigma_1 + 3\sigma_3 > 0 \tag{2.7}$$

or

$$\sigma_3 = -T_0 \quad \text{for } \sigma_1 + 3\sigma_3 < 0 \tag{2.8}$$

Assuming a state of uniaxial compression, the Griffith criterion yields $UCS = 8T_0$, proving that the dominant failure mode of rock is in tension (Bieniawski, 1967).

The Mohr-Coulomb failure criterion can determine the shear failure of cohesive materials but does not take into account the intermediate principal stress. As already mentioned, rock strength increases under hydrostatic confinement and therefore the intermediate principal stress needs to be part of the derivation. More than that, ductility of rocks is considered to be proven by the fact that despite the significant amount of cracks in their structure, rock masses can still maintain their load bearing capacity (Alejano & Alonso, 2005; Salehnia et al., 2017). Ductility increases with confinement, and therefore the failure criterion used to characterise rock behaviour should capture this behaviour.

This dependence of rock strength in compressive confinement can successfully be represented with the Drucker-Prager yield criterion (Peng & Zhang, n.d.). The Drucker-Prager yield criterion is expressed as:

$$\sqrt{J_2} = A + BI_1 \tag{2.9}$$

where, I_1 is the first invariant of the Cauchy stress

J_2 is the second invariant of the deviatoric part of the Cauchy stress

A, B are constants determined with experiments

Moreover, the criterion expressed in terms of Von Mises stresses and hydrostatic stress has the following form:

$$\sigma_v = a + b\sigma_m \tag{2.10}$$

Where, a, b are material constants

Essentially, the Drucker-Prager yield criterion is an extension of the Mohr-Coulomb criterion, and their relationship can graphically be represented in the principal stress space as shown in fig. 2.4. Depending on the choice of the envelope enclosing the Mohr-Coulomb criterion, different conversion formulas are derived for the transformation of the Mohr-Coulomb material parameters to the ones used in Drucker-Prager.

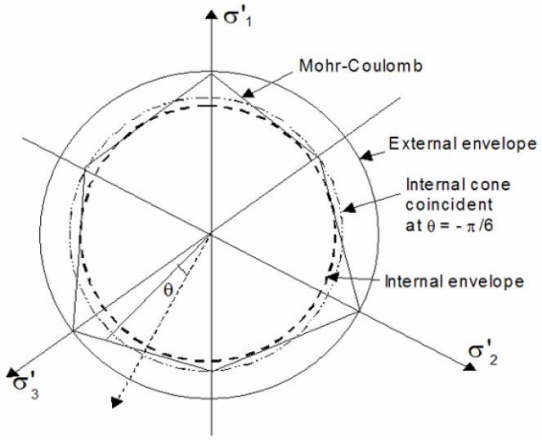

Figure 2.4: Graphical representation of the Drucker-Prager criterion in the principal stress space. ***(Peng & Zhang, n.d.)***

Furthermore, the Extended Drucker-Prager (EDP) criterion allows for the definition of a potential flow that determines the behaviour of rock after failure, accounting for a certain level of ductility. The EDP criterion is further explained in the designated chapter of the analysis.

2.2 Rock Cutting

Rock breaking can be performed with either explosive or non-explosive methods. It is obvious that for avoiding damaging the monopile structure, a non-explosive method must be chosen. Some of the latter methods include hydraulic rock splitting, expansive chemical agents and mechanical rock cutting. Mechanical rock cutting tools can either be drag bits/picks or indenters. The difference between the last two lies in the way they operate, as can be seen in fig. 2.5. The indenter breaks the rock by being pressed normally to the rock surface, essentially crushing the rock. An elliptical crushed zone is formed under the tip of the indenter that imposes tensile stresses to the rock while it expands, forming cracks. On the other hand, the drag bit slides across the rock surface, in parallel to the direction of cutting. The principal force is in the moving direction of the tool, while the normal to the rock surface force is considerably smaller if there is no significant blunting of the tool (Ramezanzadeh, 2010). The selection between the two mining tools is closely related to the strength of rock that needs to be cut. In general, for performing an operation on soft rock, drag bits are the better choice with less energy required for breaking the same amount of rock, compared to indenters.

In hard rock, though, the durability to wear development is the main parameter for choosing the appropriate tool. Indenters will experience an even loss of material during rock cutting, possibly giving an advantage to the use of this type of tool.

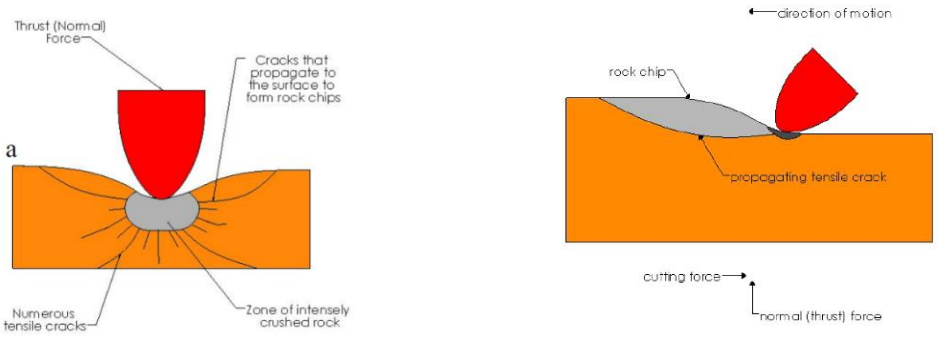

Figure 2.5: Rock cutting by indenter (a). Rock cutting by drag tool (b). ***(Ramezanzadeh, 2010)***

Both drag tools and indenters use the same principle: generating tensile stresses, utilizing the significantly lower tensile strength than the compressive one of rock. Examining the rock breakage mechanism in a microstructure level, it can be said that the breaking process is the same independently of the used tool. As can be seen in fig. 2.6, an indentation consists of a crushing and chipping phase, with the first including fragmentation and increase of applied force and the second, the ejection of the crushed material and force reduction due to strain energy release (Pang et al., n.d.). The crushing phase ends when the critical load is reached and then the chipping phase begins. In the end of the chipping phase, the energy transfer is zero and a new cycle begins. The magnitude of the critical force for breaking the rock changes at each cycle due to the 'chipping process, the brittle nature of rock and its inhomogeneous, fractured structure' (Bilgin et al., n.d.). The shape of the indenter dictates the resistive force as a function of the indentation depth, with the relationship being linear for a wedge and quadratic for a conical tip.

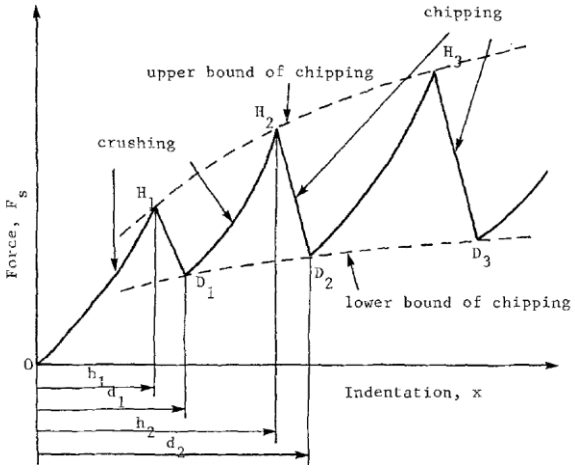

Figure 2.6: Rock chipping process. ***(Pang et al., n.d.)***

Investigating the rock breaking mechanism at a distance from a free surface of rock, a similar process is observed. The penetration of the mining tool in the rock creates an elliptical crushed zone below its tip.

This zone of high compression generates tensile hoop stresses that exceed rock's tensile strength, creating radial cracks which propagate to the free surface and form brittle rock chips (Bilgin et al., n.d.).

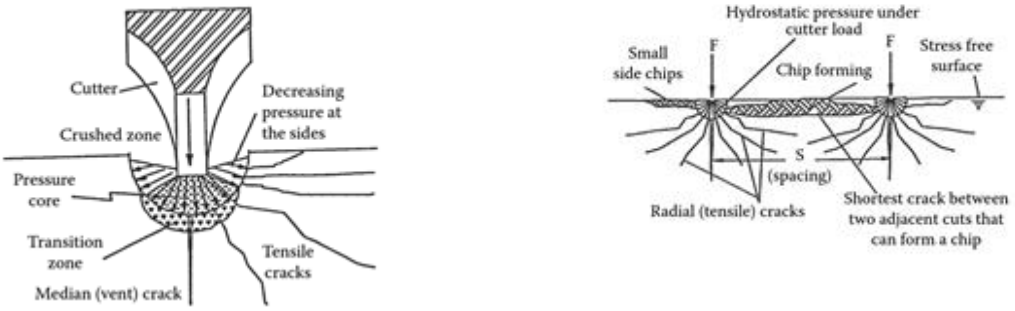

(a) (b)

Figure 2.7: Breaking mechanism at a distance from a free surface of rock. No tool interaction (a). With interaction (b). ***(Bilgin et al., n.d.)***

Two are the main theories, used in the mining industry, for analytically determining the required force for breaking a part of rock at a distance from a free surface, namely the Evans and Nishimatsu models. The fundamental difference between the two is that the Evans model assumes tensile stresses to be the critical stresses leading to rock failure, while Nishimatsu's model is based on shear failure (Ouyang et al., 2020).

Considering the Evans theory, the force required to detach rock material at a certain distance from a free surface depends on the geometry of the cutting tool, the friction between the rock and the tool's material, the tensile strength of rock and the distance from the free surface, called 'depth' of cut. Failure occurs along a circular arc, propagating towards the free surface, when the tensile strength of rock is exceeded (Vlasblom, n.d.). This model can successfully describe the rock cutting operation with the use of a chisel tool, as it was developed from experimental research on mining equipment of that geometry. Formulas for both a symmetrical and an asymmetrical wedge were derived from Evans, with the first case representing an indentation scenario and the second a, more realistic, continuous rock cutting process (Ouyang et al., 2020).

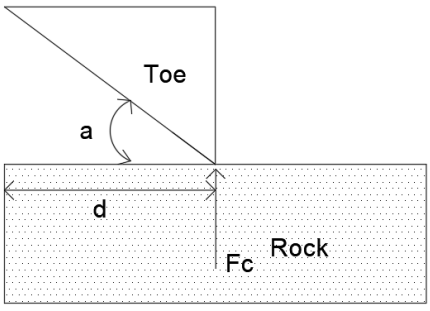

Figure 2.8: Evans theory parameters.

The force required to cut the rock, according to Evans, is expressed from the following formula:

$$F_c = \frac{2\sigma_t * d * w * \sin\left(\frac{\pi}{4} - \frac{\alpha}{2} + \varphi\right)}{1 - \sin\left(\frac{\pi}{4} - \frac{\alpha}{2} + \varphi\right)} \quad 2.11$$

where, d is the penetration depth

w is the width of the tool

φ is the friction angle between rock and tool

The model confirms that smaller cutting angle a leads to smaller required cutting force (F_c), as the literature suggests (Bilgin et al., n.d.; Pang et al., n.d.; Ramezanzadeh, 2010; Vlasblom, n.d.).

Nishimatsu (1972) assumed that rock fails in the brittle regime following a straight failure plane, under an angle β with the cutting direction. The failure satisfies the Mohr-Coulomb criterion and both the shear and normal stresses distribution along the failure plane are considered with the use of the stress distribution factor n:

$$n = 11.3 - 0.18a \quad 2.12$$

Using the minimum work hypothesis, the cutting force for a chisel pick can be determined as follows:

$$F_c = \frac{2\tau_0 * w * d * \cos i \cos(\varphi - \alpha)}{(n+1) * (1 - \sin(i + \varphi - a))} \quad 2.13$$

where, τ_0 is the shear strength of rock

i is the rock internal friction angle

Evans model can accurately predict the peak cutting force but may overestimate the average forces assuming maximum tensile stress at the entire failure plane. On the other hand, Nishimatsu's theory considers the possibility that failure can occur even though the strength of the rock is not exceeded everywhere in the failure plane but may fail to predict the peak cutting force required for breaking the rock (Miedema, 2019).

2.3 Cutting Tool Wear

As discussed in the previous chapters, the wear in the cutting toe plays a significant role, if not the most important, in successfully completing the driving operation and installing the monopile in the desired penetration depth. High strength rocks generate highs stresses on the cutting tools that cause fracture, cracking and in some cases collapse (Hurt & Macandrew, 1985). The latter would obviously mean failure of the installation method. Excessive wear in the cutting toe should be avoided as this would lead to higher required cutting forces, that either cannot be delivered by the available hydraulic hammers or can lead to the compromise of the monopile's structural integrity. The general rule suggests that increasing the depth of cut results in reduction of tip wear but increasing the rake angle causes an increase of wear.

Choosing the right material for the cutting toe is a function of both structural performance and cost. Considering the fact that the cutting tool equipped in the bottom of the pile will only be used once, using expensive materials for its construction creates a scenario that would not be appealing to the companies considering utilizing the drill-drive operation in investigation. Possible materials would be steel, tungsten carbide, cemented carbide or polycrystalline diamond (PCD), with the last two being the most expensive choice (Ramezanzadeh, 2010). Each material showcases different advantages and disadvantages that are closely related to the cutting operation. In a drag-force cutting operation (sliding) tungsten carbide or PCD would experience less wear compared to steel and their brittle nature would possibly not hinder the cutting operation (Doğruöz, 2010). On the contrary, in an indentation rock breaking operation where impact is involved, steel or cemented carbide appears to be the best choice of material as ductility is required for surviving the cutting process. A combination of materials is possible as often used in cutter head design of cutter suction dredgers (CSD). This combination can include a cutting tool made of steel with a tungsten carbide tip and/or PCD grains in the functional parts. Close attention should be given in properly joining the different materials and the problems that may arise from this process. It is worth mentioning that steel inserts or bolts can be avoided, and brazing can be used instead for joining steel and tungsten carbide.

As already mentioned, although steel exhibits a beneficial ductile behaviour during indentation, lacks in hardness and wear resistance. In order to overcome these drawbacks and combine high strength, hardness and impact fracture resistance, shock resisting steels have been developed.

The addition of silicon as an alloying element reduces the risk of fracture, while manganese, molybdenum, chromium and carbide provide the required hardness levels for a cutting operation. Shock resisting steel specifications are included in the AISI (American Iron and Steel Institute) standards and are divided in six grades, namely S1, S2, S4, S5, S6 and S7. Each grade has a different composition that makes it suitable for specific operations. The S2 grade would perform the best in situations where high impact stresses are expected to occur, having the highest toughness and yield strength of all, namely $f_y = 2131\ MPa$. Following the heat treatment, S2 steel develops a hard case and tough core that makes it suitable for chisels and punch tools. The shock resisting steels can be welded using a filler metal with similar composition to the alloy and following the inert-gas-shielded and shielded-metal-arc processes (Harvey, 1982).

Although sufficient research has been carried out regarding rock breaking operations and the performance of various types of tools, the effect of tool wear on this performance still remains and under-researched topic. That is because wear is a system-dependent process with varying characteristics that make the task of creating analytical formulas and solutions to particular problems a challenging one. The so-called ‘tribosystem’, whose wear is part of, is closely related to the frictional, lubrication and environment conditions (Verhoef, 1997). Different materials and surfaces will exhibit different frictional behaviour, the existence of debris or crushed rock as an interfacial medium between tool and rock will alternate the wear process and conducting the breaking operation under water will give rise to additional uncertainties. For all these reasons, to describe the wear process accurately extensive data are necessary from the physical and chemical conditions of the tool’s material, the rock and their interaction.

A classification of the wear process based on the types of motion and material phases has been carried out by various researchers (Figure 2.9). Four basic mechanisms can be assumed to be the base of all possible wear mechanisms: tribochemical reaction, adhesive wear, abrasion and surface fatigue. Rock cutting operations are governed by two main wear mechanisms, namely adhesion and abrasion. The first describes the increase of wear due to the high temperatures on the wearing surface that will eventually lead to plastic deformation and 'thinning' of the steel tool to a failure mode identified as 'wear flat' (Verhoef, 1997). The second wear mechanism is closely related to the hardness of the materials in contact and describes the gradual material loss of a cutting tool during the relative sliding motion against the asperities of rock. Additionally, the driving of the monopile in rock and the impact that it will cause due to the dynamic loading on the steel tool, will potentially lead to localised surface fatigue failure.

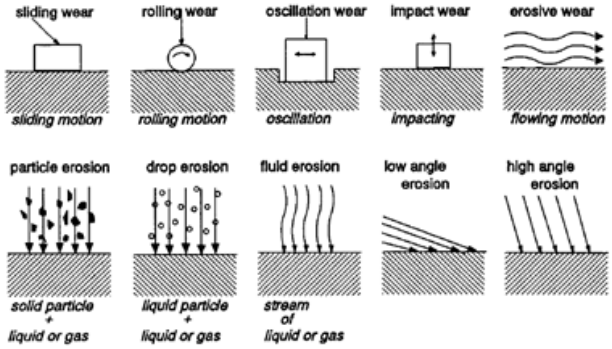

Figure 2.9: Concepts of wear processes from tribology. ***(Verhoef, 1997)***

As mentioned already, rock cutting is an especially complicated process from a mechanical point of view, and so is wear development in rock cutting tools. Important rock engineering parameters have to be taken into account when predicting the wear mechanism and its extent during an operation. The specifics of the operation will affect the wear propagation, such as the material of the tool, the geometry of the tool and the velocity of cutting. Furthermore, the rock properties and condition play a decisive role in the wear process and tests on site should be carried out for the accurate determination of their influence. In general, increased hardness of rock will increase the abrasive wear while a reduced ductility of rock or the existence of extensive microcracks will cause some relief in the wear process (Hurt & Macandrew, 1985). The rock strength, the roughness of its surface, the abrasion and the grain size of minerals all have an impact in the blunting mode. For some type of rocks, e.g. sandstone, also the penetration depth of the tool affects the wear, with most damage happening in the initial stage of penetration (Verhoef, 1997).

Only few millimetres of wear flat can cause a substantial increase in the required cutting force due to the change in geometry of the tool. For example, a 4mm wear flat can cause a 2-3 times increase in the required cutting force and 4-5 times increase in the specific energy needed to break the rock (Dogruoz et al., 2016; Dogruoz & Bolukbasi, 2014). In theory, if the tool could keep its initial shape, no increase of required force would occur. Unfortunately, the eventual blunting of the sharp edge of a cutting tool against rock cannot be avoided and, therefore, the decrease of the cutting performance needs to accurately be defined.

Some of the first research projects on the effect of tool tip wear suggest a half-power law relationship between the fracture force and the width of the blunt flat but could not be confirmed by experiments and subsequently get broadly accepted by the research community. However, what is clear is that the wear flat perpendicular to the rake face has a considerably greater effect that the blunting in the parallel, to the cutting, direction (Verhoef, 1997).

Extensive experimental research on the effect of wear flat on the cutting force of chisel tools was carried out by Bilgin et al. (2012) who tested the cutting performance of wedge-shaped tools on various type of rocks and cutting distances. The results of this study were expressed as a multiplication factor for the Evans rock cutting theory, taking into account the increase of the force required for breaking a piece of rock as wear develops in the tool. The analytical formula that can be used for correlating the wear flat (WF) and cutting force can be seen in Figure 2.10. It can be seen that a wear flat of just 2mm causes the required rock cutting force to double. These results were in agreement with previous studies and were acceptedby the research community.

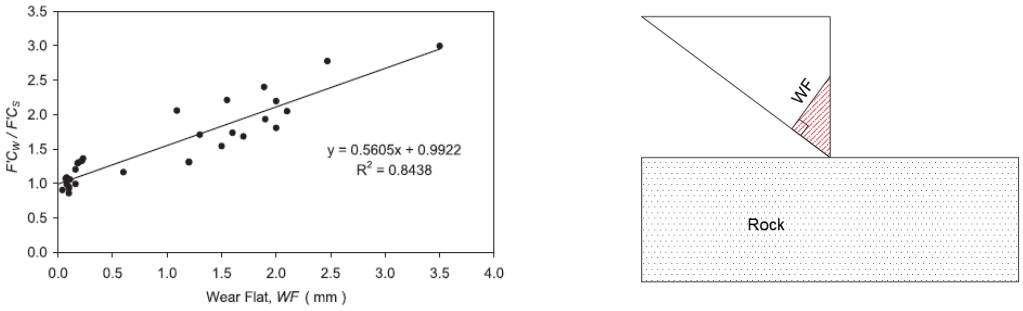

Figure 2.10: Increase in required rock cutting force as a function of wear flat in the tool. ***(Bilgin et al., 2012)***

The wear flat on the tool is related to the required cutting forces, for blunt and sharp conditions, according to the formula:

$$WF = \frac{\frac{FC_w}{FC_s} - 0.9922}{0.5605} \qquad 2.14$$

where, WF is the wear flat of the tool perpendicular to the rake face

FC_w is the required cutting force for a blunt tool

FC_s is the Evans cutting force assuming sharp tip conditions

2.4 Contact mechanics

The work of Hertz and Boussinesq is widely considered as the fundamental theories for contact mechanics problems. Based on their research, closed form analytical solutions can be found in literature, mostly for axisymmetric problems of contact between solid bodies of various geometries. It is clear that analytical solutions cannot be developed without assumptions and simplifications and the direct translation of these models to reality comes with a certain degree of abstraction.

Omitting these assumptions in an analytically solved contact mechanics problem, requires a recursive iteration procedure, numerically evaluated integrals and functions and the adoption of a non-exact solution that lacks comprehensiveness (Popov et al., 2019).

'Boussinesq problems' refer to frictionless normal contact problems where no adhesion is to be expected. Normal non-adhesive contact is defined as a contact between two elastic bodies of Young's Modulus E_1 and E_2, Poisson's rations ν_1 and ν_2 and an axisymmetric difference of their profiles expressed with the function $z = f(r)$, with r being the polar radius in the contact area (Hertz, 1882). The same problem can be translated to the case of a rigid body with profile z, penetrating an elastic half-space with effective Young's Modulus of:

$$\frac{1}{E'} = \frac{1-\nu_1^2}{E_1} + \frac{1-\nu_2^2}{E_2} \qquad 2.15$$

The boundary conditions include the normal force F_z that brings the two bodies in contact and an assumed material linearity. The solution of the normal contact problem yields the penetration depth d, the contact radius a and the pressure distribution in the contact area. The Boussinesq Problem can be solved exactly with the MDR method, that transforms the 3D contact problem to one-dimensional contact with a series of independent springs. The solution steps include (Popov et al., 2019):

- The replacement of the elastic bodies with a Winkler foundation, with springs of stiffness $\Delta k_z = E'\Delta x$.
- The transformation of the three-dimensional profile z to a plane profile $g(x)$.

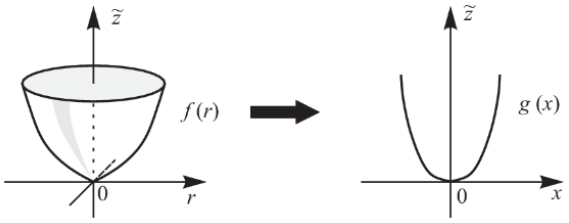

Figure 2.11: MDR method – 3D to 2D transformation. ***(Popov et al., 2019)***

The new arrangement leads to the solution of the normal contact problem by solving the one-dimensional problem of the plane profile pressed into the spring foundation under the force F_z.

The abovementioned solution approach can be used for solving the classical Hertz problem, of a paraboloid/sphere penetrating a half-space (Hertz, 1882). The shape of the contact profile, which can be seen in Figure 2.11, is defined by the expression of the parabola:

$$f(r) = \frac{r^2}{2R} \qquad 2.16$$

The plane profile is then characterised by:

$$g(x) = \frac{x^2}{2R} \qquad 2.17$$

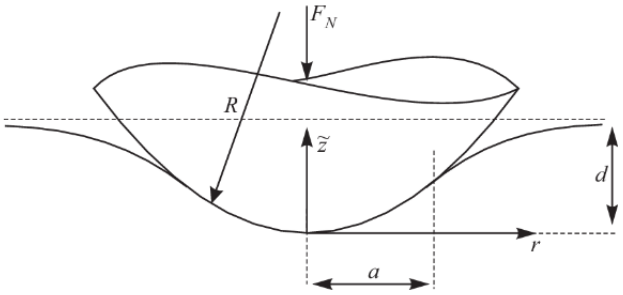

Figure 2.12: Hertz contact problem of a paraboloid penetrating an elastic half space. (Popov et al., 2019)

The penetration depth d and the contact radius a can be calculated from the expressions below:

$$d(a) = \frac{a^2}{R} \tag{2.18}$$

$$F_N(a) = \frac{4}{3} * \frac{E' a^3}{R} \tag{2.19}$$

The maximum contact pressure is located at $r = 0$ and an average contact pressure for the entire contact radius can be defined as shown in expression 2.20.

$$p_0 = \frac{4E'a}{3\pi R} \tag{2.20}$$

The derivation of the formulas that are provided in this chapter can easily be found in literature and the provided references.

2.5 Dynamic Loading & Impact Propagation

The dynamic response of piles from driving operations is analysed with considering the pile as an elastic rod in which a stress wave propagates. Numerical modelling has been used for years according to the wave theory of Smith, that is characterised, though, by certain limitations, mainly in representing accurately the damping and soil properties.

In order to bypass those limitations, a full dynamic analysis of the pile driving can be executed with the 3D modelling of the hammer-pile-soil system. This multidimensional model requires extensive computational resources and that is why, in search of an approximative solution, a simplified 1D model of a propagating axial stress wave in an elastic rod may be used, with the soil response being represented by spring/dashpot systems along the length and at the tip of the pile (Metrikine & Vrouwenvelder, n.d.).

The equation of motion of the axial response of an elastic rod according to one-dimensional wave dynamics theory, when no external loading is considered, is:

$$\frac{\partial^2 u}{\partial t^2} = c^2 \frac{\partial^2 u}{\partial x} \tag{2.21}$$

where, u is the axial displacement of the rod

$c = \sqrt{\frac{E}{\rho}}$ is the wave speed

t is the time

x is the coordinate along the length of the rod

Mathematically, the longitudinal wave motion in thin rods and the transverse defections of strings are equivalent (Metrikine & Vrouwenvelder, n.d.). That means that the D'Alembert solution of the abovementioned equation can be searched as the combination of a travelling 'f' and reflected wave 'g':

$$u = f(t - z/c) + g(t + z/c) \qquad 2.22$$

When a compressive wave travels to the end of a fixed rod, a compressive wave of the same shape will reflect upwards causing the stress to double at the fixed end. This doubling of the stress can cause serious damage to the pile tip and has to be taken into account when driving is performed in hard soil conditions, such as rock. On the contrary, the velocity will reflect with a negative sign, meaning that it is zero at the fixed end.

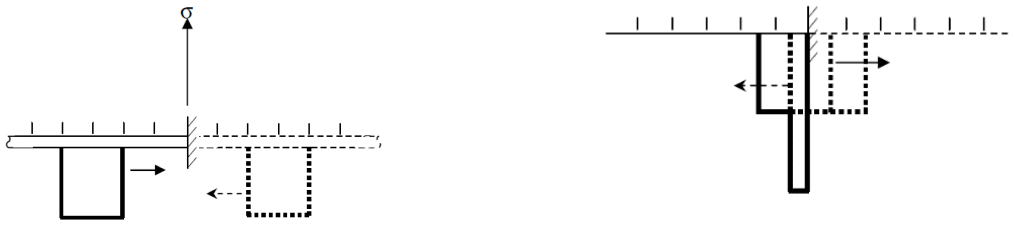

(a) (b)

Figure 2.13: Compressive propagating wave in a fixed rod (a). Stress pulse multiplication at the fixed end (b). ***(Metrikine & Vrouwenvelder, n.d.)***

In the case of a free end, a tensile reflected wave of the same shape will be generated, leading to zero stress at the pile tip. The displacement field will get doubled.

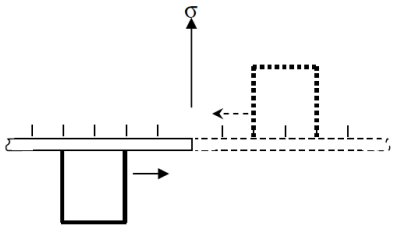

Figure 2.14: Stress pulse reflection from a free end. ***(Metrikine & Vrouwenvelder, n.d.)***

Of course, the reality lies somewhere between a perfectly fixed and a free end. Soil or rock will provide resistance to the pile's vertical movement, which can be transferred in the 1D model with springs of finite stiffness that will cause the stress pulse to deform at the pile tip. The deformed, now, wave will propagate upwards.

However, reflected waves with irregular shape can also be generated along the pile due to changes in the cross-section, discontinuities or defects. The sign and magnitude of the reflected wave depends on one of the most important parameters in impact propagation, the pile's impedance (Z):

$$F(t) = \frac{EA}{c} * v(t) = Z * v(t) \qquad 2.23$$

where, $F(t)$ and $v(t)$ are the force and velocity field, respectively

This parameter dictates how the force is transferred in the pile, with high impedance leading to transmission of forces with lower stresses and velocities than lower impedance would require. Going back to reflected waves from points of discontinuity at a pile, the sign and shape of those waves depend both on the ratio of impedances of the two segments and the properties of the interface condition (spring or dashpot) (Metrikine & Vrouwenvelder, n.d.; Parola, 1970).

The D'Alembert solution assumes that the incoming wave retains a constant shape until it reaches the pile tip. Hence, it is valid for a linear elastic system with no distributed springs or dashpots along the pile length, that would allow for skin friction resistance from the soil to be considered. If this shaft resistance is considered, wave dispersion occurs and a different solution has to be investigated. The solution, in this case, will have to satisfy the following equation of motion:

$$c^2 \frac{\partial^2 u}{\partial x} = \frac{\partial^2 u}{\partial t^2} + \frac{k_d}{\rho A} u + \frac{\varepsilon_d}{\rho A} \frac{\partial u}{\partial t} \qquad 2.24$$

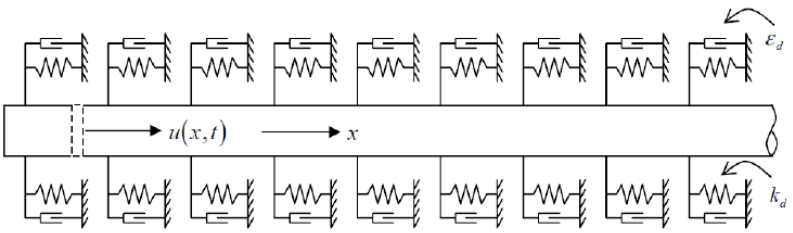

Figure 2.15: Distributed spring-dashpot systems along the elastic rod. ***(Metrikine & Vrouwenvelder, n.d.)***

Force and velocity decrease due to the reflective waves from the soil, as can be seen in Figure 2.16, with significant shaft friction translating to smoother decrease along the pile length.

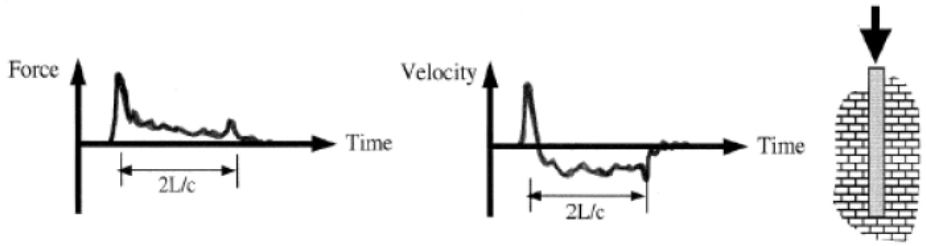

Figure 2.16: Force and velocity decrease in pile due to shaft friction resistance. ***(Jorna, 2018)***

The representation of the pile's response with the one-dimensional structural dynamics theory is done under specific assumptions:

- the material is elastic and homogeneous
- no variations in the cross section of the pile
- no body forces in the pile
- stress is uniformly distributed over the rod
- lateral inertia is ignored

Those assumptions cannot be seen as negligible and can lead to inaccurate results. To bypass those assumptions, numerical analysis and the wave equation of Smith has been used extensively in the offshore industry. Software like GRLWEAP can perform such numerical analysis.

According to the driveability numerical method developed by Smith, the pile is discretised into a series of individual masses that are connected with each other via linear springs (Hamdi, n.d.). The resistance of the soil is expressed with a shaft resistance and base resistance, both modelled with a system of springs, dashpots, and sliders. A small incremental step is chosen, and the propagation of the impact wave is analysed at each node of the pile considering changes arising from the change of pile impedance or soil-pile interaction. The hammer is also part of the analysis, using the displacement method approach for determining the force that is transferred to the pile.

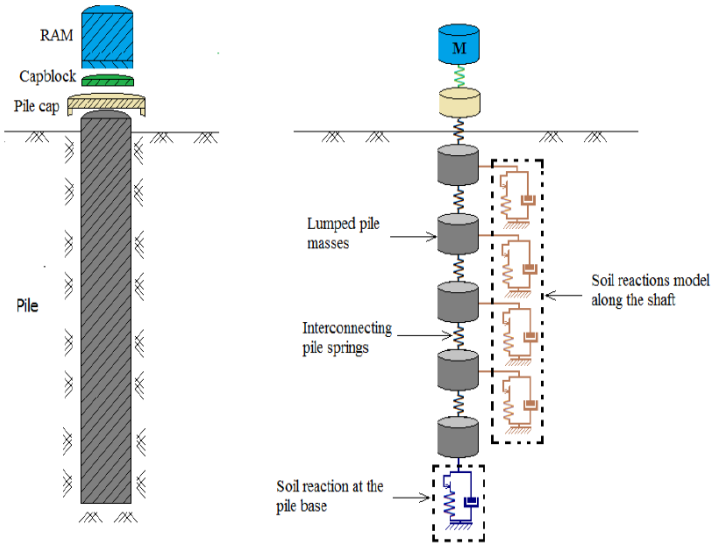

Figure 2.17: Smith's model for dynamic pile driving analysis. ***(Hamdi, n.d.)***

GRLWEAP software is able to perform driveability analysis of piles using the wave equation numerical analysis procedure. The user can choose from a big database of soil and hammer types, and providing those and the pile geometry, an output of the total blow-count and the associated penetration depth is given, determining if premature refusal occurs or not. Additionally, the driving resistance, the pile stresses and the total driving time is given by the software.

Although the analytical solutions and the numerical approach has been proven to work, difficulties in accurate determination of stiffness and damping parameters and the need of including material non-linearities, large displacement effects or residual stresses in the pile, point out to FE modelling as the favoured analysis tool for accurately describing the response of a monopile during driving. In this study, the analysis will be conducted by modelling the monopile and the rock around it with finite elements in the software ANSYS. The soil-structure interaction, and more specifically, the base resistance will be implemented into the model using spring elements with the appropriate stiffness. Sub-modelling will be used for deriving this stiffness, investigating the cutting process between cutting toe and rock with a different FE model.

2.6 Pile Tip Damage

Steel piles are used in offshore applications due to their good bending stiffness and ease of installation (Randolph, 2018). The diameter to shell thickness ratio is continuously increasing making the monopile susceptible to pile tip deformations, especially when it encounters layers of hard soil, that may lead to early refusal during driving. A common pile tip failure is extrusion buckling in which progressive elliptical distortion occurs, starting from the tip (Randolph, 2018). This distortion sometimes can go undetected hindering the in-service performance of monopiles, causing unexpected problems even years after the installation procedure took place. Cases of extrusion buckling have already been confirmed in projects around the world, as in Rotterdam, Goodwyn A, in Australia, and Valhall, in the North Sea (Alm & Jacket, 2004; Great Britain. Health and Safety Executive. & MSL Engineering., 2001; Hamdi, n.d.). Current guidelines seem unable to predict this kind of failure, due to correlating the pile tip damage with excessive axial stresses in driving but not accounting for the gradual, propagating damage that extrusion buckling is characterised for (Randolph, 2018). In other cases, an early refusal during driving indicates possible distortion of the pile at its tip, which bends inwards leading to higher resistance in driving. In general, reports of damage during installation have been published for projects in soft rock and they point out to local buckling, rather than global pile collapse.

Figure 2.18: Pile tip extrusion buckling. (Randolph, 2018)

A driving shoe is usually welded in the bottom of the pile to increase the end bearing resistance or reduce the internal skin friction and thus reduce the resistance to driving, without though guaranteeing structural integrity. The driving shoe is recommended to provide a local increase in thickness of at least half of the pile wall, at length of one diameter from the tip (Great Britain. Health and Safety Executive. & MSL Engineering., 2001).

The fact that the piles that were reported to have experienced damage were equipped with driving shoes, should encourage the industry to search for other, more sophisticated, solutions for ensuring a safe installation by monopile driving.

Several factors can lead to local buckling of the pile tip during driving. Firstly, the possible increase of the stress propagating pulse, generated by the hammer, when it reaches the soil or rock in the tip of the pile should be investigated and taken into consideration during the design phase. Heterogeneous soil conditions and local hard spots can produce an asymmetrical soil reaction force and high difference between external and internal pressure acting on the pile wall, capable of initiating a tip distortion. Additionally, the reports on incidents of pile damage during driving suggest that considering initial imperfections is crucial when a realistic pile behaviour is analysed during the design stage (Randolph, 2018). The DNV codes provide guidelines about such imperfections, namely an initial deviation from the nominal radius of 0.5% of the pile radius, among others. Excessive plastic deformation on the tip due to high stresses should be avoided, with a maximum plastic strain in the end of the driving operation of, approximately, 1% being accepted as safe.

Although, pile tip failure during driving is not covered in official guidelines, reports on pipeline buckling and the current literature of classical mechanics are utilised for describing possible failure modes of piles, that occur individually or in combination, during installation by driving (Great Britain. Health and Safety Executive. & MSL Engineering., 2001). These failure modes are discussed further in this chapter.

Pile tip local buckling (crimping) due to high tip stresses can occur if the critical classic elastic axial buckling stress is exceeded (Brush & Almroth, 1975):

$$\sigma_{cr} = \frac{2E\left(\frac{t}{D}\right)}{\sqrt{3(1-\nu^2)}} \qquad 2.25$$

This failure mode is assumed to be governing in driving installation procedures in rock, due to the high bearing resistance of rock.

Ring or shell buckling of a perfect cylinder under a critical radial pressure can be initiated according to Bresse (1866):

$$p_e = \frac{3EI}{\left(\frac{D}{2}\right)^3} \qquad 2.26$$

where, p_e is the critical Bresse pressure

During driving in sandy soil or clay, the passive earth pressure exerted on the pile can yield such failure mode. On the other hand, failure during installation in rock by driving is expected not to be governed by ring buckling, unless collapse of the rock borehole around pile occurs.

Ovalisation of initially imperfect piles is likely to occur under lateral pressure and excessive membrane and bending stresses, both for out-of-roundness and out-of-circularity imperfections.

Timoshenko (1961) introduced the following formula for this critical pressure:

$$\left(\frac{p}{p_p}\right)+\left(\frac{p}{p_p}\right)\left(\frac{p_e}{p_e-p}\right)\left(\frac{6\beta_0 R}{t}\right)-1=0 \qquad 2.27$$

where, p is the collapse pressure

p_p is the hoop yield pressure

p_e is the Bresse pressure

$\beta_0=\frac{w}{R}$ is the ovalisation angle

The imperfections are considered with the equivalent imperfection factor:

$$w=\frac{w_0}{1-\frac{p}{p_e}}+\frac{c}{4\left(\frac{p_e}{p}-1\right)} \qquad 2.28$$

where, w_0 is the initial out-of-circularity imperfection and c is the initial out-of-roundness

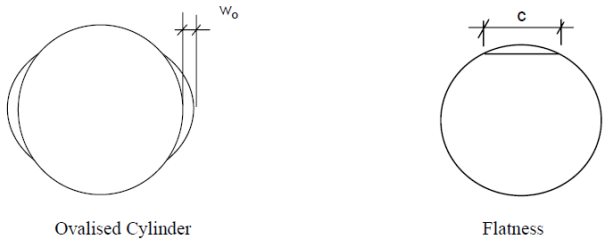

Figure 2.19: Out-of-circularity imperfection (left). Out-of-roundness imperfection (right). ***(Great Britain. Health and Safety Executive. & MSL Engineering., 2001)***

Denting damage or further enlargement of an initial dent can occur during a pile driving operation in rock. Without initial denting, the critical load reaching the tip that would initiate damage, according to the literature, is:

$$Q_{tip}=4.65 f_y t^2\sqrt{\left(\frac{\delta}{D}\right)} \qquad 2.29$$

where, δ is the dent depth

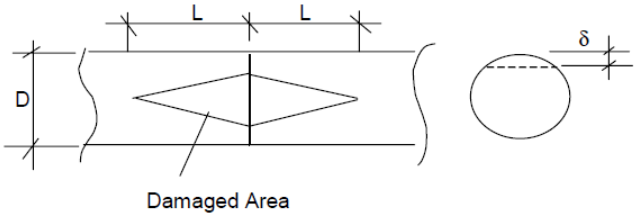

Figure 2.20: Denting damage in pile. ***(Great Britain. Health and Safety Executive. & MSL Engineering., 2001)***

Reckless handling operations or fabrication mistakes can create an initial dent in the pile, δ_0, that will expand during additional loading (ΔQ_i) in driving according to the expression:

$$\delta_I = \frac{\delta_0}{1 - \frac{2\Delta Q_i}{Q_0}} \quad 2.30$$

where, δ_I is the dent depth after the load increment and Q_0 is the initial load

This failure mode is assumed to be critical for early penetration refusal, because the cycling loading in a driving installation procedure could lead to excessive deformation even with a small initial damage on the monopile's structure.

Finally, fatigue damage is of great concern in the case of monopiles which are not accessible for inspection. The cycling loading could prove to be especially dangerous since the fluctuating stress waves during the installation phase can limit significantly the fatigue life of monopiles and cause incremental damage. The fatigue resistance can be determined using the appropriate S-N curves, proposed in guidelines such as the DNV codes or EN1993-1-9, and the information of the driveability analysis, in particular the blow counts and stress ranges.

In general, the procedure to conduct the fatigue analysis would be (Great Britain. Health and Safety Executive. & MSL Engineering., 2001):

- The stress ranges and blow counts versus depth can be evaluated with the wave equation analysis
- Careful selection of stress concentration factors (SCF) and S-N curves for the calculation of fatigue damage
- Determination of driving damage at each blow and subsequent calculation of the total damage using the Miner's Rule.

Fatigue damage is out of the scope of this thesis.

2.7 Cemented Carbide

Cemented carbide (CC) has gained popularity in a big range of applications, from metal machining to rock mining and drilling, due to its extraordinary set of mechanical properties. Specifically, the combination of extreme hardness and substantial impact resistance, distinguishes cemented carbide from all of the other hard metals available in the market for the construction of tools (SANDVIK, n.d.). It is made of a tungsten carbide phase (WC) and a metallic binder phase, mostly cobalt (Co), with the latter adding ductility to the material. The final properties of cemented carbide depend on the carbide grain size, the percentage content of binder and the existence of other metal additives (e.g. nickel, chromium, molybdenum), but also the working conditions. The fact that the desired mechanical characteristics can be given to the material during its manufacturing, makes it appropriate for a variety of engineering projects.

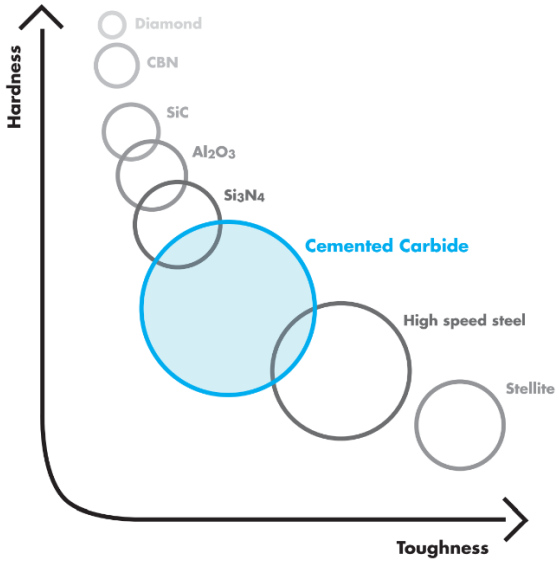

Figure 2.21: Cemented carbide compared to other hard metals and diamonds. ***(SANDVIK, n.d.)***

In general, the tungsten carbide phase ranges in 70-97% of the entire material mass, with a grain size of 0.2-20 μm. The compressive strength of cemented carbide can reach up to 7GPa, with this value reducing for increasing binder content and grain size. The hardness follows the same trend, while fracture toughness tends to increase with increasing the binder phase and grain size. In particular:

- Binder content of 3-10% and grain size smaller than 1μm leads to material with high compressive strength and great wear resistance, appropriate for metal machining
- Binder content of 6-30% and grain size between 1-3μm gives CC improved fracture toughness, suitable for using in wear parts of cutting tools
- Binder content of 6-15% and grain size bigger than 3μm results in cemented carbide with good impact resistance and excellent performance against abrasive wear, making it the best solution for mining applications

The wear of cemented carbide and its eventual failure is a complicate process because of the duality of its nature, having both a brittle part and a ductile part. Besides its composition, the cutting technique and speed, the rock properties and surface conditions and the heat generated during excavation will determine the failure mode of a cutting tool made of CC (Nahak et al., 2018). To elaborate, although brittle in nature, as the temperature in the tool-rock interface increases, the metallic phase of cemented carbide gets 'activated' and the material demonstrates capability of plastic deformation. Regarding the rock properties, cutting or drilling in harder rock with larger grains will result in an increased wear rate on the cemented carbide tool (Beste, 2004).

During rock breaking by indentation, the cemented carbide experiences crack generation. These cracks tend to open as the tool hits repeatedly the rock, resulting in rock chips penetrating the CC structure, a phenomenon called rock intermixing. The rock debris gets integrated in the metallic binder, creating a new binder phase with undesirable characteristics in terms of impact performance and ductility (Nahak et al., 2018).

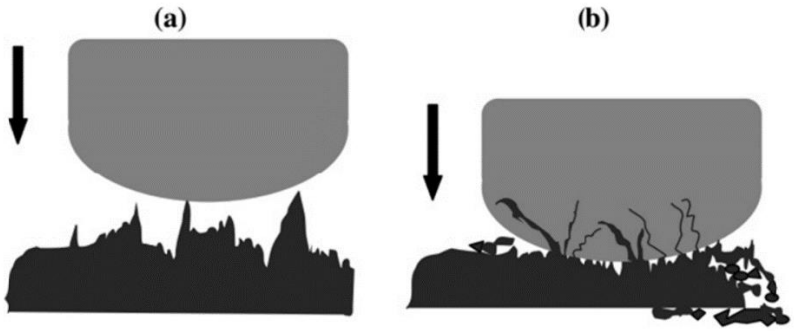

Figure 2.22: Rock intermixing. (a) Tool pressed into rock. (b) Rock chips penetrating CC ***(Nahak et al., 2018)***

The corrosive degradation or high impact stresses can result in fragmentation, with the carbide or binder phase completely getting detached from the material structure. Repeated impact could lead to carbide grains getting crushed and the entire carbide phase getting easily removed or relocated (Nahak et al., 2018). Corrosion imposes an even bigger threat to cemented carbide, with the binder phase mostly being affected. Cases have been documented, in which using CC under water resulted in a chemical reaction that caused the rupture strength of the material to decrease and the binder phase to be completely removed. Using nickel in the binder phase or special anti-corrosive CC grades, available in the market, can significantly increase the tool's corrosion resistance. Lastly, the more continuous the cutting is, more gradually wear develops in the cemented carbide tool.

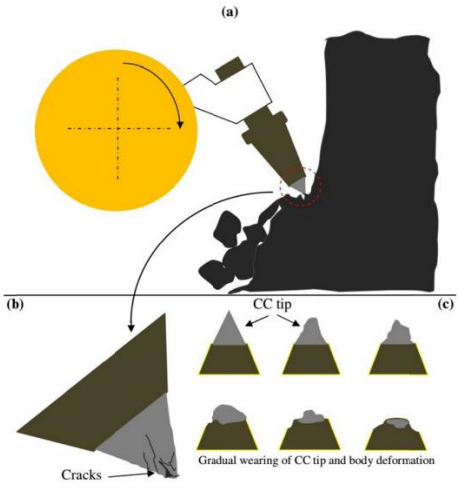

Figure 2.23: CC wear in continuous cutting. ***(Nahak et al., 2018)***

3 Simulation Approach Outline

Considering the limitations of analytical solutions, FE modelling is proven to be the most reliable method in analysing complex problems, where a full three-dimensional representation of the reality is required. More than that, FEM provides the advantage of having the ability to take non-linearities into account. These non-linearities can be material plasticity and yielding, large displacement effects and contact at the interface of different bodies, which allows for updating the stiffness matrix of the system at each iteration of load application. The non-linear relationship between applied forces and displacements is considered, yielding more accurate results of the stress distribution and produced strains in the structures under investigation. For the reasons mentioned above, FE analysis using the software ANSYS is carried out for successfully fulfilling the research goals of this thesis.

The simulation sequence follows an approach of 'sub-modelling', according to which the details of interest are analysed with different smaller models, and their results are used as input in a 'global' model. The 'sub-models' in this project are two, namely a model of the cutting toe breaking the rock and a model of the cutting toe undergoing plastic deformation as a result of the interaction with the rock. The first 'sub-model' gives the stiffness of the rock breaking operation, therefore the resistance of rock in the attempt to drive the monopile into the seabed. This stiffness is, later, represented in the 'global' model with a series of springs. The 'global' model in this research is the FE model of the monopile. The second 'sub-model', namely the cutting toe under yielding model, provides the applied load – wear flat relationship that is used for the driveability analysis. As will be discussed thoroughly in chapter 5.4.1, only part of the monopile's length was simulated for analysing the response under static loading. The simulation sequence can be seen in Figure 3.1. The models that were used are explained in detail in the following chapters.

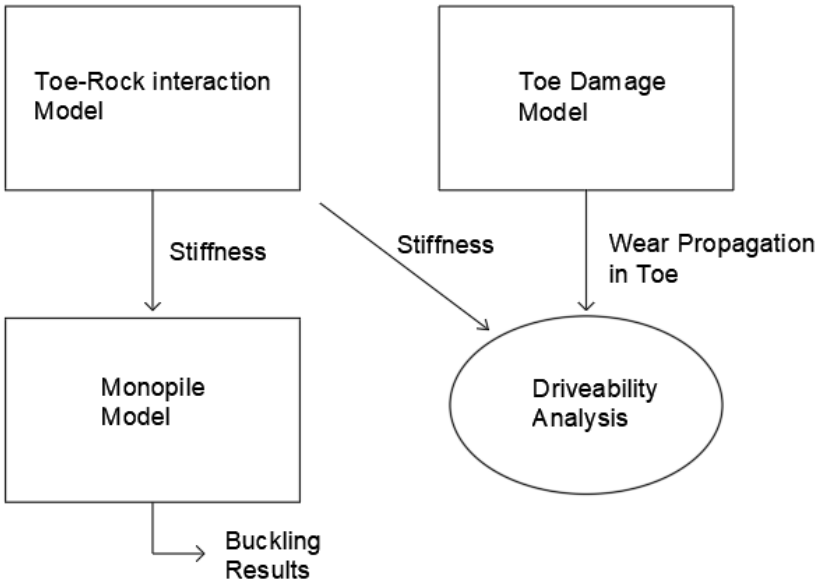

Figure 3.1: Simulation sequence.

4 Cutting Toe – Rock Interaction

4.1 Introduction to the Model

The cutting toe is modelled with a ring-shape continuous geometry, as seen in Figure 4.1. ANSYS was used for simulating the rock breaking process. In order to take advantage of the cyclic symmetry of the cutting toe, the boundary conditions and its loading in respect to the centre of the drillhole, axisymmetric solid elements were chosen for the simulation. By doing that, only one plane of the cutting toe – rock system is modelled in 2D and ran, reducing significantly the computational time. The reduction of the analysis time was proven to be necessary for granting the ability to perform the parametric investigation of the rock cutting process. The software is able to derive the solution for the full 360° model.

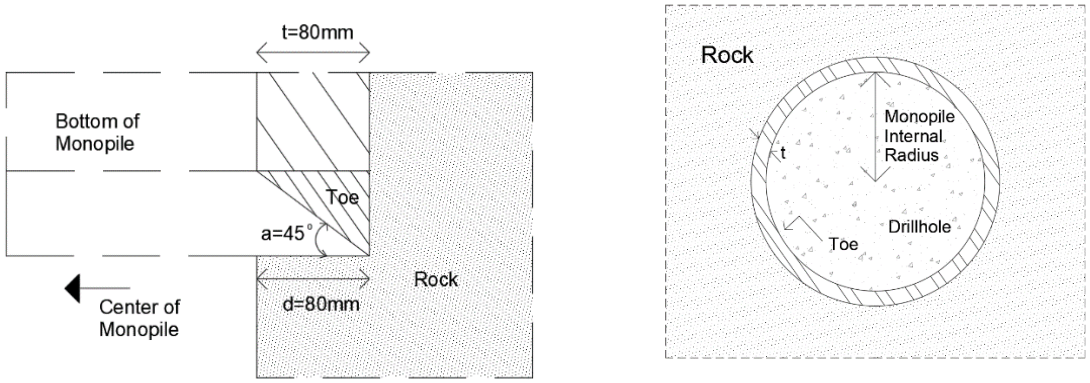

(a) (b)

Figure 4.1: Continuous cutting toe. Cross-section (a). Plan view (b).

Attention should be given to the correct application of loads in an axisymmetric model, with the concentrated forces imposed on a full 360° basis. The constraints, surface loads, line pressure, and Y-direction accelerations are applied as they would in the case of a non-axisymmetric 3D model. In ANSYS, the model should be in the global X-Y plane, with the Y-axis being the axis of symmetry and the entire modelled structure lying in the positive X quadrants.

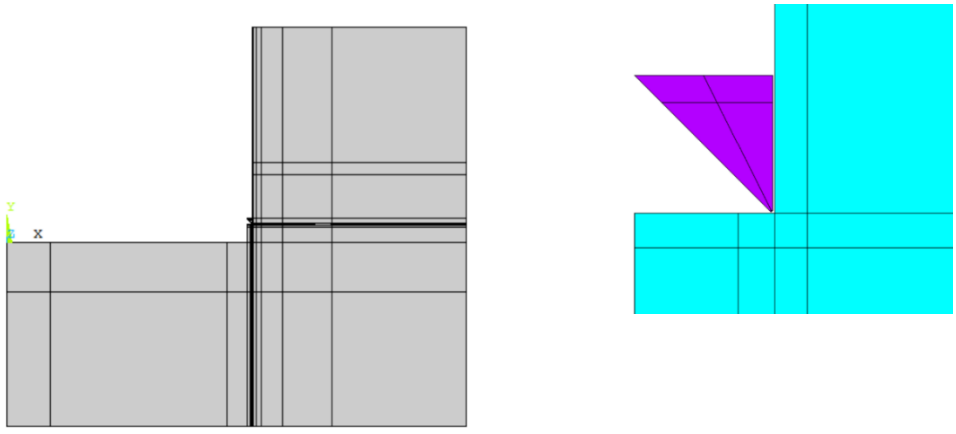

(a) (b)

Figure 4.2: Axisymmetric model of cutting toe-rock interaction (a). Close-up view in cutting toe (b).

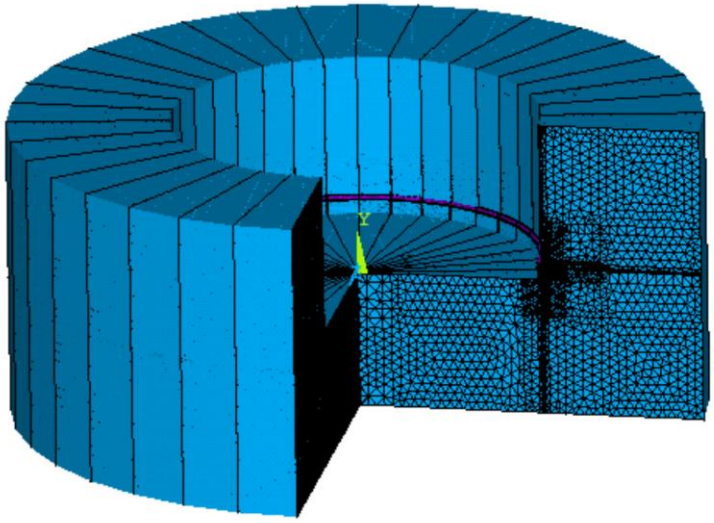

Figure 4.3: Full 360° model of cutting toe-rock interaction. Toe depicted in pink colour. Rock depicted in blue colour.

The axisymmetric elements are of second order, with either 8 or 6 nodes per element. In the areas of higher strains, namely the part of the rock close to the indentation point and the tip of the cutting toe, quadrilateral elements with 8 nodes were used. Those provide a more accurate representation of the strain evolution and deformation when using a coarser mesh. In the areas of less interest, 6-node triangular elements were modelled.

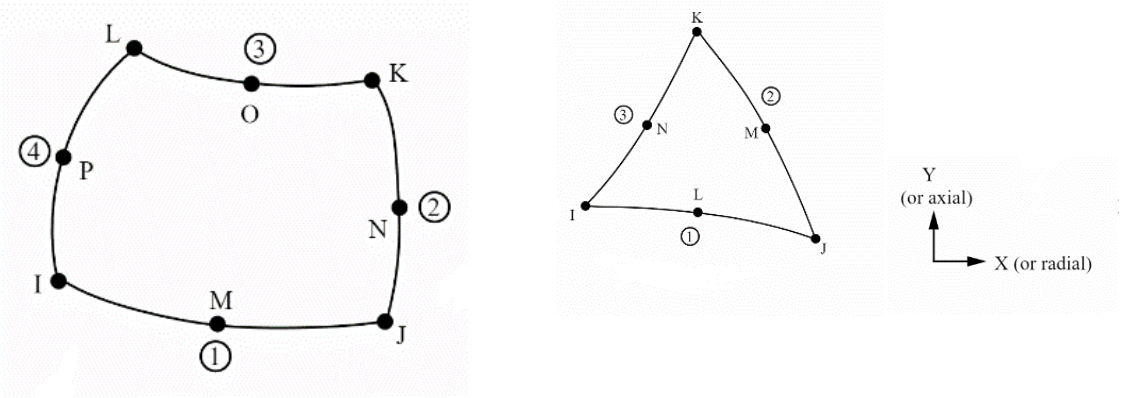

(a) (b)

Figure 4.4: Axisymmetric elements: quadrilateral (a), triangular (b).

In order to avoid singularities, the sharp tip of the cutting toe was replaced with an arc of radius 1mm. A finer mesh was used in the areas of high strains, with a favourable aspect ratio. For the rock, the aspect ratio is 1. For the tip of the cutting toe, due to the irregular geometry a unit aspect ratio could not be maintained, but rather an aspect ratio smaller than 3 was chosen for all elements. Following a mesh sensitivity analysis, a mesh size for the rock of 0.5x0.5 mm was chosen (Appendix B8). ANSYS is dimensionless, but the entire model was created considering mm as the unit of length.

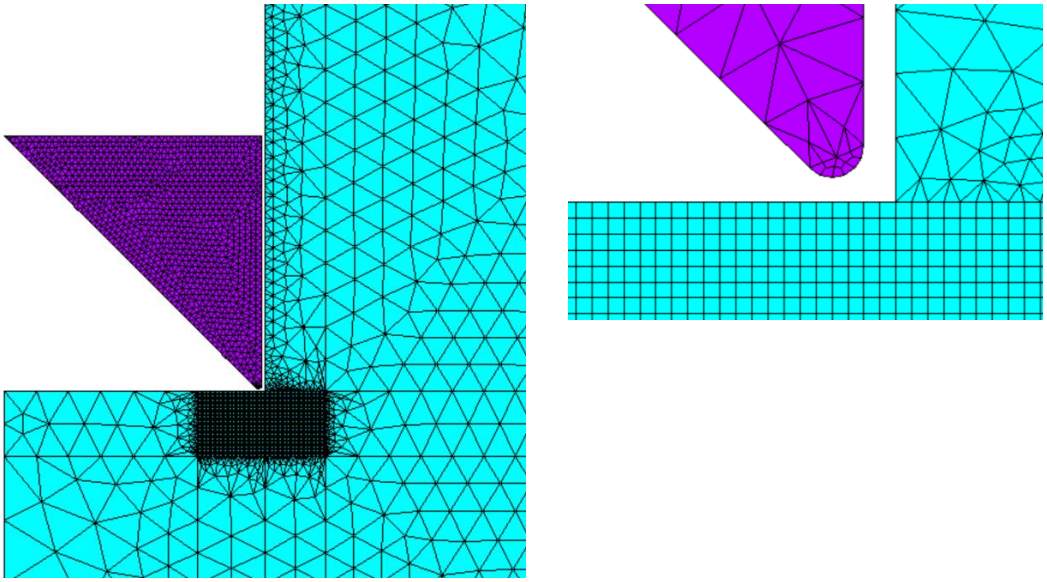

(a) (b)

Figure 4.5: Cutting toe-rock model mesh (a). Close-up view (b)

Contact is defined both between the tip of the cutting toe and the rock, and between the side face of the cutting toe and the rock. Standard frictional contact is established assuming that both contacting bodies are deformable, an option that in the environment of ANSYS is described as 'flexible-to-flexible' contact. Each contact consists of two sets of elements, namely contact and target elements, with each set being assigned at one of the two contacting faces. The contact is established when the nodes of the contact elements meet the face of the target elements.

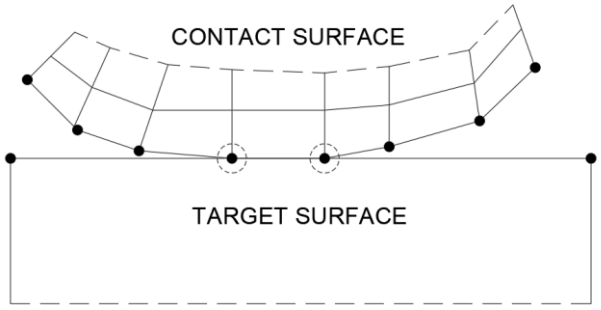

Figure 4.6: Contact between 'contact' and 'target' surface.

When each face has only one set of elements, meaning only contact or target elements, then the contact is defined as 'asymmetric'. In the case that each face has both sets of elements, the contact is characterised as 'symmetric'. In the model of the cutting toe breaking the rock, the contact between the two bodies is assumed to be asymmetric. Attention should be given for the correct assignment of the target and contact face in the contact pair in order to avoid unexpected behaviour at the interface of the contacting bodies and excessive penetration. Understanding the physics of the contact problem under investigation is crucial for making the correct decision about this assignment and achieving the desired accuracy.

The ANSYS manual provides guidelines that can help the user make the appropriate designation in the two contacting faces, such as:

- When a curved surface comes in contact with a flat surface, the flat surface should be designated as the target surface.
- If the one surface is significantly larger than the other, then the larger surface should be the target one.
- When a surface moves towards a second surface, the latter should be designated as the target.

Because the cutting toe is pressed into the rock, designating the cutting toe as the contact body and the rock as the target body represents more realistically the given problem.

In FE modelling, contact definition introduces non-linearities that require significant computer resources and lead to bigger analysis times, with the possibility of convergence problems. To avoid these problems, the faces of each contact pair demonstrate a similar mesh with matching nodes. Numerical gaps are designed for both the toe tip-rock and toe side face-rock contacts, that are set to automatically close when the analysis begins.

In practice, the top face of the cutting toe is fixed to the bottom of the monopile. That means that the top face moves as a rigid one, not experiencing relative displacement and rotation. For representing this behaviour, two rigid 'pseudo-faces' are attached to the top of the cutting toe. Vertical loading is imposed to the top face of the cutting toe and the relative displacement of its nodes are documented for different stiffness values for the 'pseudo-faces', in an iterative procedure. By following that procedure, the stiffness of the 'pseudo-faces' that leads to rigid face behaviour of the top of the toe, was found to be $2 * 10^5\ GPa$. The displacement of 'pseudo-faces' is constrained in the X-direction, while no restriction of motion is applied to the cutting toe faces.

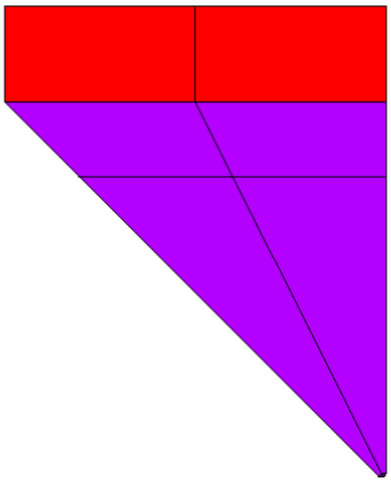

Figure 4.7: 'Pseudo-faces' depicted in red.

4.2 Modelling the Rock

Typical properties of rock types that is possible to encounter on an offshore monopile installation were used for the various investigations that are discussed in this research project. Each type of rock is characterised by a big range of mechanical properties. Representative values of this range were chosen from the available literature. Two different sandstone rock properties are included in the research investigation, representing the middle and lower bound of the values for this rock type.

Rock	Compressive strength (MPa)	Tensile Strength (MPa)	Young's Modulus (GPa)	Toe-Rock friction coefficient	Bulk Density (kg/m³)
Granite	179.1	10.77	67.8	0.27	2690
Limestone	127.3	7.45	60	0.43	2660
Sandstone	71.3	4.41	53.3	0.17	2370
Sandstone 2	48.2	2.6	53.3	0.17	2370

Table 4.1: Rock properties. ***(Bilgin, 1977)***

The rock medium that encloses the monopile is infinite in reality. Hence, the appropriate total area of modelled rock in ANSYS should be determined, and it is the one that gives accurate results without increasing, unnecessarily, the computational time. This area is estimated by running analyses for different areas of modelled rock around the cutting toe and documenting the resulting stiffness of the breaking operation. When the stiffness reaches a plateau, then the applied constraints do not affect the results and the desired modelled rock area is found. Regarding the constraints, the rock is fixed in the outmost lines, in reference to the point of indentation, in both plane directions. This was chosen for representing the confinement pressure that rock would experience, when analysing a finite rock mass at a considerable depth below the surface of the seabed. The final height of the modelled rock mass is approximately 6m, which puts the model at a theoretical depth of 10m below the seabed surface, considering a final penetration depth of the drill-drive installation of approximately 15m. The final model of the rock mass can be seen in Figure 4.3 of the previous sub-chapter. The cutting toe can also be seen with pink colour in that same figure, giving a reference of the difference in size of the two bodies.

For this investigation, a uniform pressure in the vertical direction of 50 MPa is imposed in the top face of the cutting toe. ANSYS demonstrates a rather expected behaviour, with the stiffness reducing as the modelled area increases and the constraints lie in a greater distance in respect to the indentation point. The stiffness (K) is determined as the gradient of the vertical force (F) – vertical displacement (v) graph for the cutting toe, following Hooke's law $F = K * v$. The force is expressed in N per mm of circumference and the vertical displacement in mm, giving a stiffness value with units N/mm^2 . Both the force and vertical displacement are measured for a node in the top (rigid) face of the cutting toe. Because of the non-linearity that the contact definition introduces, the force – displacement relationship is not exactly linear but can still be approximated to a linear one, with a correlation coefficient R^2 bigger than 0.99. The force – displacement graph for the analyses with various areas of modelled rock can be seen in Graph 4.1.The corresponding linear approximation is also depicted.

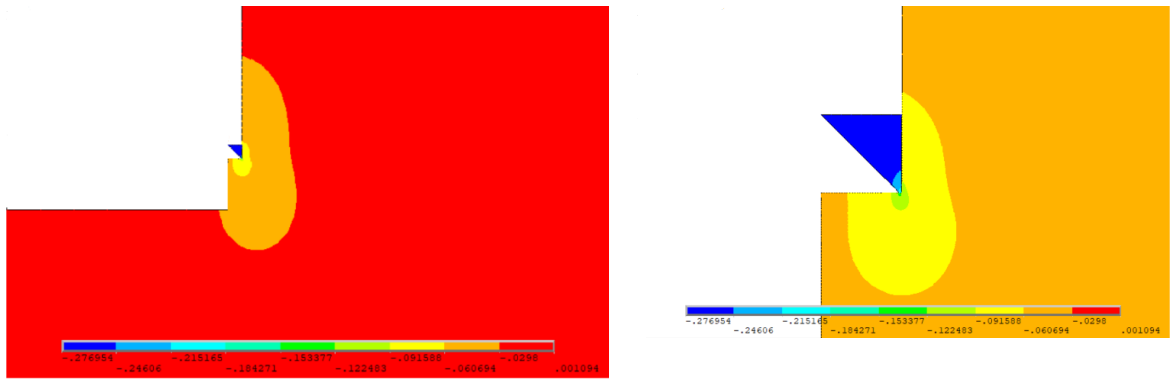

(a) (b)

Figure 4.8: Vertical displacement for Area_4 model: Part of the model (a). Close-up view in toe (b).

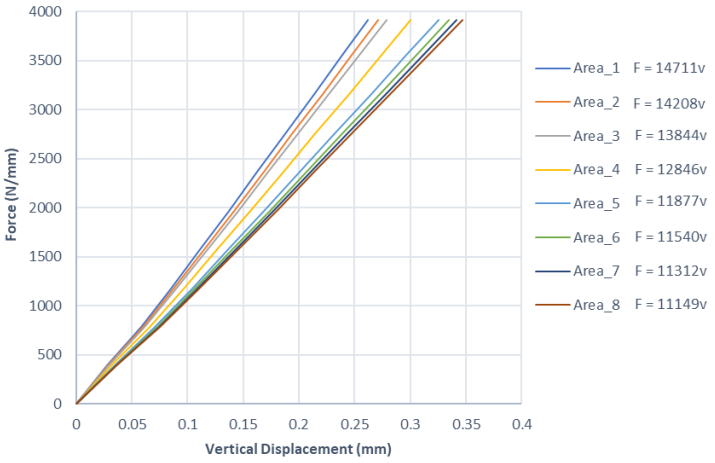

Graph 4.1: Force-displacement curve for different rock modelled areas.

Table 4.2 shows the total rock area for each model and the resulting stiffness. Linear elastic properties were used both for the rock and the cutting toe. The rock material is granite, and the cutting toe is made of tungsten carbide, with the elastic, isotropic properties given in Table 4.1 and Table 4.3 respectively. Large displacement effects are active during the analysis, accounting for changes in geometry as the bodies deflect. These changes alternate the stiffness matrix of the finite element formulation and should be taken into consideration for achieving the desired accuracy of results.

Area (m^2)	Stiffness (N/mm^2)
0.27432	14711
0.4524	14208
0.6705	13844
2.361	12846
11.436	11877
23.017	11540
38.598	11312
58.179	11149

Table 4.2: Resulting stiffness for rock modelled area investigation.

Plotting the resulting stiffness versus the area used for modelling the rock mass, it can be seen that after a modelled area of 20 m^2 the stiffness reaches a plateau with a reduction of only 1.5 % for a 15 m^2 incremental area increase. Hence, a total surface area of 23 m^2 was chosen for simulating the rock mass and it is used for the investigations that follow in the next chapters.

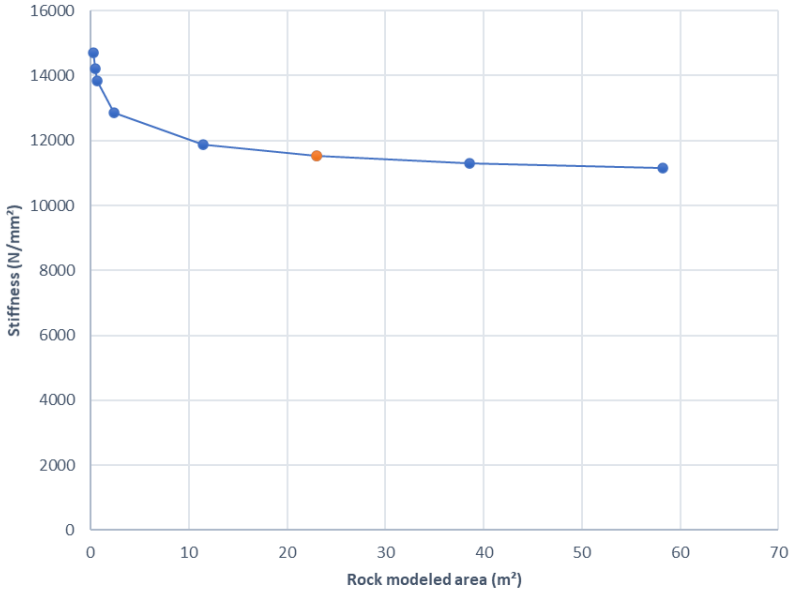

Graph 4.2: Resulting stiffness for different areas of modelled rock.

4.3 Toe Material: Tungsten Carbide vs Steel

The use of tungsten carbide and steel for the design of mining equipment was already discussed in chapter 2.3. Steel behaves in a ductile manner and can be assumed to fit the purpose of a drill-drive installation in rock, where high impact stresses are expected in the cutting toe, at a lower cost. A first indication of the effect of the cutting toe's material on the stiffness of the rock cutting operation can be given by only considering elastic, isotropic material properties. The values for both materials are given in Table 4.3. Graph 4.3 shows that using tungsten carbide results in a stiffer rock cutting operation compared to steel, namely 14.5% increase. That is credited to the higher Young's Modulus of tungsten carbide, leading to smaller vertical deflection for the same load applied on the top face of cutting toe. It is noted that because of the linear properties assumption, no differentiation between tungsten and cemented carbide is made.

More than that, the friction coefficient between tungsten carbide and rock is smaller than the one for steel and, therefore, there is bigger resistance in vertical motion provided from the defined contact on the toe's side face.

Toe Material	E (GPa)	v
Tungsten Carbide	550	0.31
Steel	210	0.3

Table 4.3: Elastic properties of tungsten carbide and steel

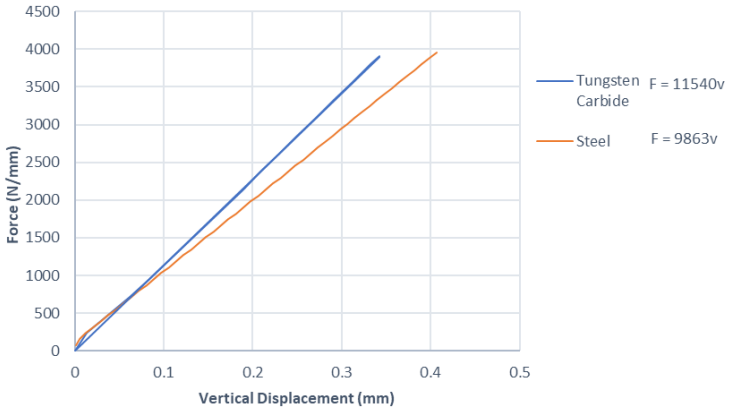

Graph 4.3: Force-displacement curve for cutting toe made of steel and tungsten carbide.

4.4 Effect of Cutting Angle

The rake angle is the most important parameter affecting the cutting performance of a rock mining tool. The general trend, according to the literature, suggests that an increase of the rake angle leads to more aggressive cutting. That means that a lower stiffness of the rock breaking process is expected as the rake angle grows. The drawback of a higher rake angle is that the tool becomes more susceptible to wear. This will be further investigated in chapter 8.

In order to investigate the effect of the rake angle in the cutting toe's performance, parametric analysis was carried out with an incremental change in angle of 5°. Specifically, cutting angles of 45°, 50°, 55°, 60°, 65°, 70° and 75° were used for a series of analysis in ANSYS. These values are judged as realistic for the design of the cutting toe in the drill-drive installation method that is investigated. The contact and rock mass is modelled as described in chapters 4.1 and 4.2 respectively, the toe's material is elastic, isotropic steel and uniform vertical pressure is imposed in the top face of the cutting toe. To be able to justify the direct comparison of the different models, the number of elements and mesh size in the contact areas were kept constant for every model. Moreover, the same maximum contact penetration is allowed, namely 1% of the maximum deflection. The latter can be controlled by adjusting the Normal Contact Stiffness in the contact definition of ANSYS. The 45°, 60° and 75° models that were used in this investigation can be seen in the figure below.

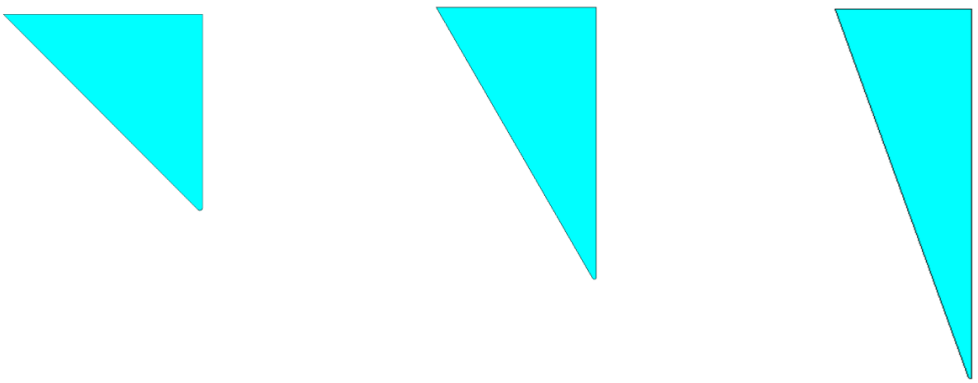

(a) (b) (c)

Figure 4.9: Modelled cutting toes (not to scale). 45° (a). 60° (b) . 75° (c)

The results from the simulations confirm the literature outcome that bigger cutting angle leads to smaller stiffness. The trend of this reduction can be seen in Graph 4.4, where the stiffness for the different cutting angle models is plotted.

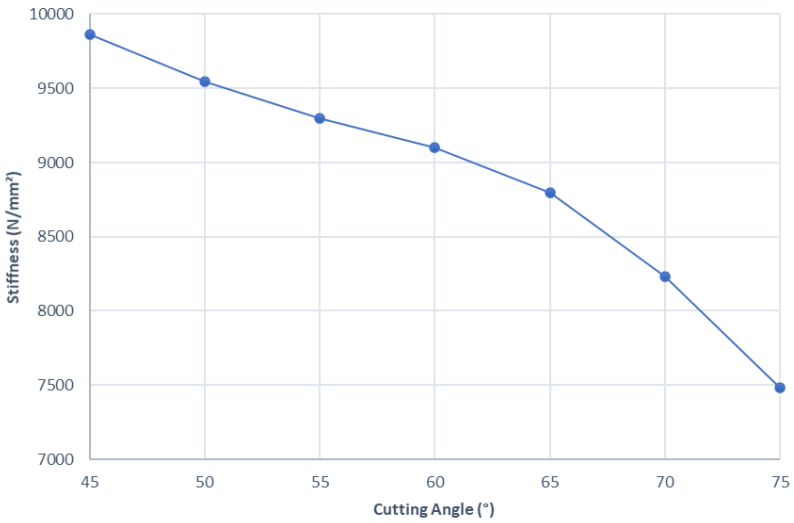

Graph 4.4: Stiffness of the rock cutting operation for various cutting angles.

It is clear that as the angle of 75° is approached, the gradient of the line becomes steeper and the reduction in stiffness is bigger. Specifically, the incremental percentile difference in the last step (70° to 75°) is close to 9%. That value is bigger than the difference of 2-3% that is found in the first four increments. The average difference per increment of 5° is approximately 5%, as seen in Graph 4.5.

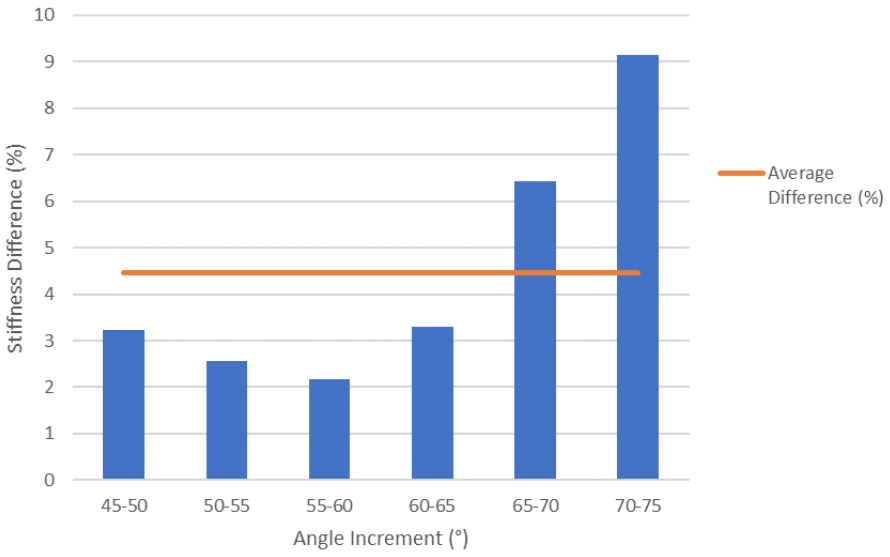

Graph 4.5: Difference in stiffness per angle increment of 5°.

4.5 Stiffness vs Rock Type

Different rock types were investigated for providing a more clear understanding of the resistance that the cutting toe would encounter during a drill-drive installation method. The rock types that were chosen are granite, limestone and sandstone, representing a broad range of soil properties that the seabed is made from. The properties for each rock type are given in Table 4.1: Rock properties. (Bilgin, 1977)Table 4.1.

The model of the rock mass, the contact definition and the cutting toe model were discussed in chapters 4.1 and 4.2. The material of the cutting toe is steel, the rake angle is 45° and the applied load on the top face of the toe is uniform stress in the vertical direction with a value of 50 MPa. No material non-linearity is considered. The force-displacement graphs were constructed and the gradient, representing the stiffness of the cutting operation, was determined through linear approximation for each type of rock. Graph 4.6 shows the distribution of stiffness versus rock type. Intuitively, it is expected that considering stronger rock will result in higher stiffness of the cutting operation. This is clearly confirmed by the numerical analysis in ANSYS .

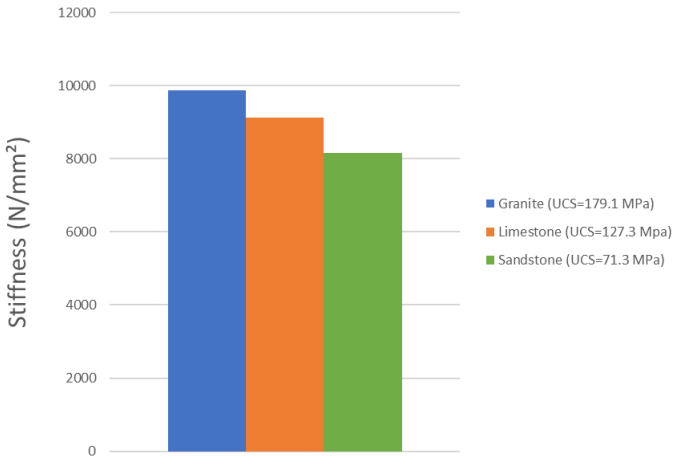

Graph 4.6: Stiffness of rock cutting for different types of rock.

4.6 Rock Plasticity

One of the biggest uncertainties in mining engineering is predicting the crack initiation and propagation and the way the rock will eventually break from the cutting operation. For this, the fractured structure and the inhomogeneous nature of rock are responsible. It is not possible to know before the operation begins, the level of disturbance that the rock has experienced, its discontinuities and if its mechanical properties have deteriorated in the course of time. Hence, on-site testing (e.g. rock coring) is mandatory for providing the geotechnical engineers with the information needed for estimating the failure mode of rock. Even in that case, a safety margin should be taken into consideration.

Another uncertainty in the response of rock during a breaking operation is related to its ductility. A common misconception is that rock is a brittle material. However, the fact that it can be highly fractured and still maintain its load bearing capabilities, proves that rock can demonstrate inelastic behaviour in failure.

The level of ductility is, once again, difficult to determine a priori and close investigation of the rock's condition should be conducted on site. In general, better quality rock exhibits more ductile behaviour and the ductility increases as the confinement pressure increases.

The ductility of rock is expressed with its dilatancy angle (ψ), a material constant that describes the volumetric change when it experiences shear deformations. Granular materials and rock tend to expand in volume when they are sheared and are under high confinement. The importance of dilatancy consideration has been already pointed out in several studies on rock mechanics. Different theories and formulas were proposed, mostly correlating the plastic strain evolution and confining stress, without though achieving widespread recognition (Salehnia et al., 2017). Hoek and Brown suggested that the dilatancy angle depends on the internal friction angle (φ) and the rock mass quality, proposing the values $\psi = \varphi/2$ for good quality rock, $\psi = \varphi/4$ for good-to-average quality rock, $\psi = \varphi/8$ for average-to-poor quality rock and $\psi = 0$ for rock with no plasticity (Alejano & Alonso, 2005). A non-associated flow rule is employed when the rock is analysed.

The challenges in determining the behaviour of rock during its interaction with a cutting tool translate also to the FE modelling of rock's failure. The extended Drucker-Prager yield criterion is found to be able to describe the damage in rock in finite element analysis, as it accounts for increase in yield strength as the hydrostatic compression increases (Liu et al., 2019). The extended version surpasses the shortcomings of the classic Drucker-Prager, which assumes elastic-perfectly plastic behaviour with no possibility of defining a flow rule. The extended Drucker-Prager criterion is available in ANSYS for axisymmetric elements and was used for determining the effect of rock failure in the stiffness of the cutting operation.

In the principal stress space, the yield surface of Drucker-Prager is a circular cone that corresponds to the external envelope of the Mohr-Coulomb yield surface (Alejano & Bobet, 2012), as shown in Figure 4.10.

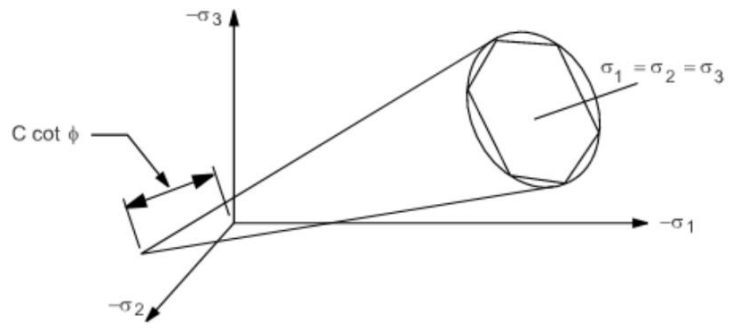

Figure 4.10: Drucker-Prager yield surface.

When expressed in the plane that is defined by the Von Mises stress (or equivalent stress) and the hydrostatic pressure, the linear Drucker-Prager yield surface satisfies the equation 4.1:

$$3\beta\sigma_m + \frac{\sigma_{eqv}}{\sqrt{3}} - \sigma_y = 0 \qquad 4.1$$

where, $\sigma_m = \frac{1}{3}(\sigma_x + \sigma_y + \sigma_z)$ is the hydrostatic stress

$\sigma_{eqv} = \sqrt{\frac{(\sigma_1-\sigma_2)^2+(\sigma_2-\sigma_3)^2+(\sigma_3-\sigma_1)^2}{2}}$ is the equivalent stress

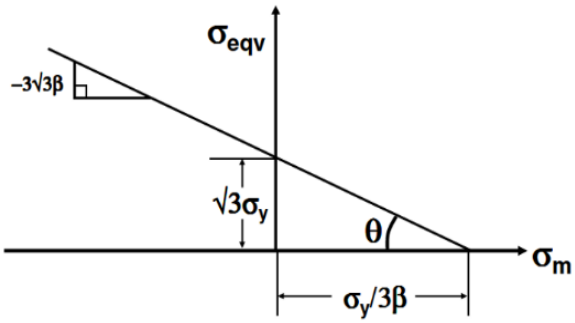

Figure 4.11: Yield strength as a function of the equivalent and hydrostatic stress, according to Drucker-Prager.

By using uniaxial compression stress and uniaxial tensile stress conditions in equation 4.1, the following formulas are derived:

$$\beta = \frac{\sigma_c + \sigma_t}{\sqrt{3}(\sigma_c - \sigma_t)} \quad 4.2$$

$$\sigma_y = \frac{2\sigma_c\sigma_t}{\sqrt{3}(\sigma_c - \sigma_t)} \quad 4.3$$

The parameters β and σ_y can be determined from the Mohr-Coulomb material parameters.

The material constant β is defined as:

$$\beta = \frac{2\sin\varphi}{\sqrt{3}(3 - \sin\varphi)} \quad 4.4$$

where, φ the angle of internal friction

The material yield parameter σ_y is derived from the equation 4.5:

$$\sigma_y = \frac{6c\cos\varphi}{\sqrt{3}(3 - \sin\varphi)} \quad 4.5$$

where, c is the cohesion

According to the ANSYS manual, the user needs to specify a pressure sensitivity (a) and a uniaxial yield stress parameter (σ_y') as input for using the linear Drucker-Prager criterion:

$$\sigma_y' = \sqrt{3}\sigma_y \quad 4.6$$

$$a = \frac{6\sin\varphi}{3 - \sin\varphi} \quad 4.7$$

The behaviour of rock after failure is described by the flow potential. For a given dilatancy angle (ψ), the linear form of the plastic flow potential is expressed by the potential pressure sensitivity (a_ψ) and it is used as input in ANSYS:

$$a_\psi = \frac{6 \sin\psi}{3 - \sin\psi} \tag{4.8}$$

An investigation was carried out for the effect of rock failure in the cutting operation. First, a parametric analysis was run for different levels of rock ductility. The ductility was defined according to the Hoek and Brown recommendations and was expressed with the ratio R:

$$R = \frac{dilatancy\ angle}{internal\ friction\ angle}$$

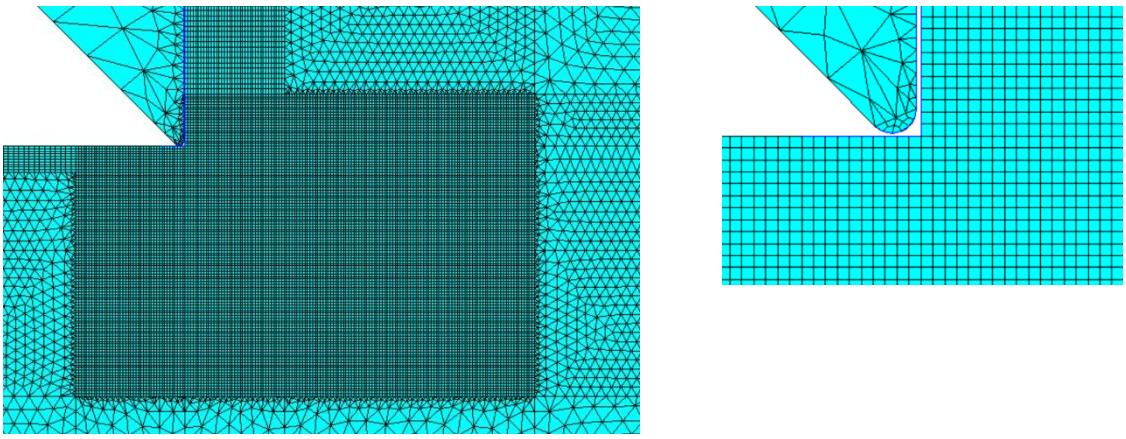

(a) (b)

Figure 4.12: Rock plasticity model mesh (a). Close-up view in toe tip (b).

The internal friction angle is constant for a given rock type and can be evaluated from equations 4.2 and 4.4. Therefore, only the dilatancy angle changes, resulting in different R values. Three values of the ratio R were investigated, namely 1, 0.5 and 0.25. The value of 1 is not realistic for rock but it was used for the sake of clarity of the results. The values 0.5 and 0.25 represent a rock of good and average quality, respectively. The rock type is granite, and the cutting toe has a rake angle of 45°, it is made of steel, and it assumed to behave elastically. The applied load on the top face of the cutting toe was determined from the Evans theory of rock cutting to be equal to 33.65 MPa. The side contact was defined as frictionless, judging that in a realistic scenario the side wall of the rock would not be able to take up much load. The wet conditions and the sudden vertical motion of the toe, resulting to an impact with the rock, were assumed to justify this judgement. The contact below the tip of the cutting toe is defined frictional according to Table 4.1. A finer mesh was used for the rock close to the indentation point, namely 0.05x0.05mm. The resulting stiffness of the cutting toe-rock interaction can be seen in Graph 4.7. It is clear that a rock with higher value R, and therefore higher ductility, will provide bigger resistance during the cutting operation, resulting in a higher stiffness.

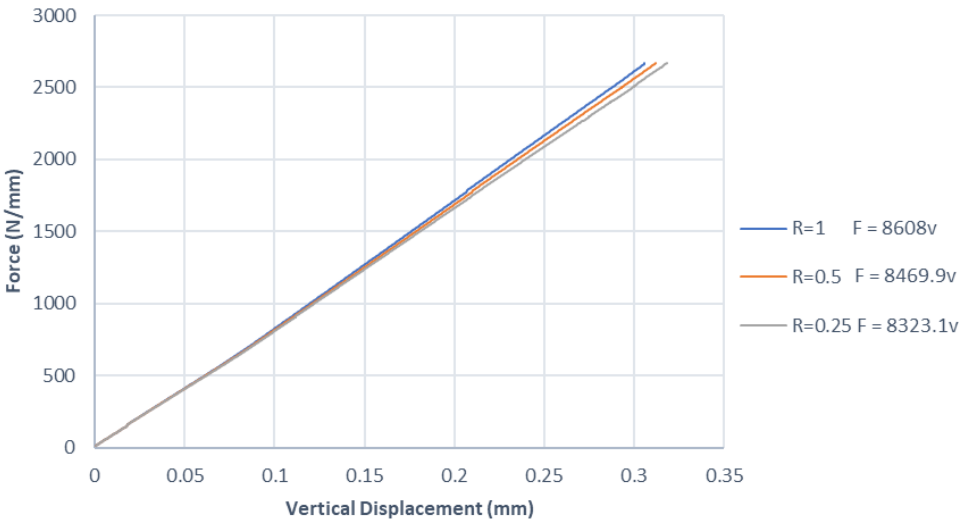

Graph 4.7: Force-displacement graph for rock with different levels of ductility.

Interesting remarks can be made from the corresponding plastic strain development for the models with different ratios R. As depicted in Figure 4.13 and Figure 4.14, the rock with the biggest dilatancy ($R = 1$) has the capacity for greater volume expansion before failure and the plastic strain does not propagate significantly. On the contrary, the rock with low dilatancy angle and, therefore, of lower quality demonstrates bigger crack propagation.

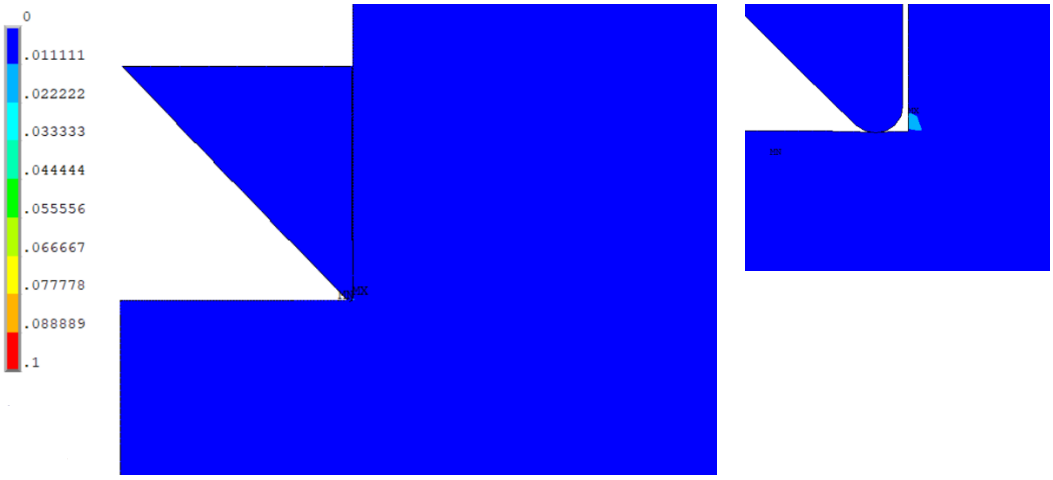

Figure 4.13: Plastic strain propagation in rock for R=1 (a). Close-up view in cutting toe (b)

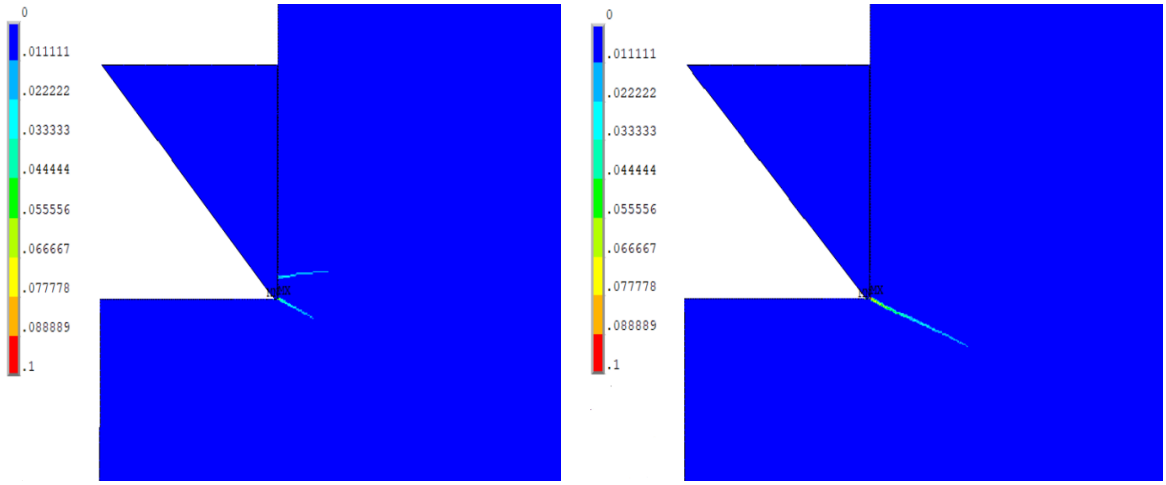

(a) (b)

Figure 4.14: Plastic strain propagation in rock. For R=0.5 (a). For R=0.25 (b)

The uncertainty in defining the friction coefficient between steel and rock in the cutting process has already been mentioned. The values used in this research were taken from literature on experimental investigation of the mechanical cutting characteristics of the specific three rock types of granite, limestone and sandstone, but they cannot assume to be accurate for every rock that will be encountered during the drill – drive installation. The quality of the rock, the asperities and discontinuities of its surface and the material conditions of the cutting toe should be analysed under a project-specific framework and only after testing on-site has been completed. Moreover, the velocity of cutting will affect significantly the level of friction at the toe-rock interface. The rock cutting operation is performed underwater which will, also, result in a reduced friction coefficient compared to dry conditions. A comparison between the friction suggested in literature and frictionless condition for the definition of side contact was made by running the non-linear analysis of rock cutting, using rock plasticity.

Elastic steel properties are used, the rock type is granite and $R = 0.5$ was assumed. The resulting force (F) – vertical displacement (v) graph is shown below. The stiffness for $\mu = 0.27$ is 9358 N/mm² and for $\mu = 0$ takes the value of 8469.9 N/mm², resulting from the linear approximation of the non-linear static analysis. The results confirm the intuitive expectation of smaller side friction leading to more aggressive cutting, and therefore smaller stiffness.

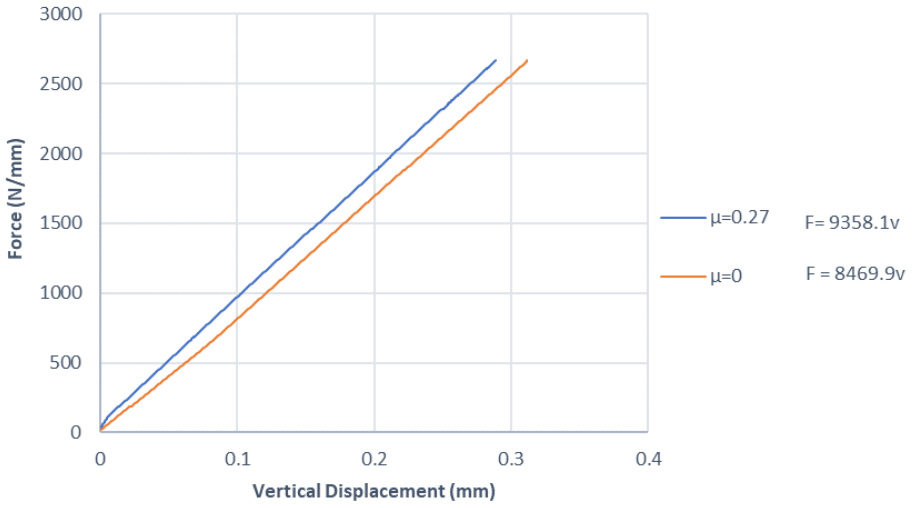

Graph 4.8: Force-displacement curve for different values of side friction between toe and rock.

Finally, an investigation of the reduction in the resistance of rock in breaking, when rock failure is considered, depending on the rock type was carried out. The extended Drucker-Prager yield criterion with ratio $R = 0.5$ was used for the 'plastic' model, while isotropic, elastic rock material properties were defined for the 'elastic' model. The force – displacement curves are provided in the appendix and the resulting stiffness can be seen in Table 4.4. The results show that a stronger rock (e.g. granite) experiences less degradation than a weaker rock when its characteristic strength is exceeded. On the other hand, the failure is more excessive for the weaker rock (e.g. sandstone), resulting in bigger reduction in stiffness when rock yielding is taken into account. Specifically, the stiffness reduction between the 'elastic' and 'plastic' conditions in granite is only 5%, with the same value climbing to 19% for the sandstone rock type.

Rock Type	Elastic	EDP	Difference (%)
Granite	9451.2	8989.4	4.9
Sandstone	8077	6596.5	18.3

Table 4.4: Difference in stiffness of the cutting operation when considering elastic and plastic rock properties.

It should be noted that the propagation of plastic strain highly depends on the way the rock is modelled. The plastic strain direction follows the path of the least compressive hydrostatic pressure, as concluded from the Drucker-Prager derivation. Hence, alternating the model of the rock mass around the cutting toe and changing the constraints would result in a different distribution of hydrostatic pressure and, consequently, different propagation of the plastic strain. This was proven by running several simulations with different rock mass models. Figures from this investigation is provided in the appendix. The desired outcome of incorporating the Drucker-Prager yield criterion in the present research is getting results on the change of stiffness when considering rock failure. Therefore, the assumption that the stiffness should be the criterion for correct rock modelling is deemed as valid.

The rock mass was simulated in a way that represents realistically the borehole around the toe, including the intact rock ring of 80mm thickness below the pile after the drilling process at an assumed depth. The modelled rock mass was gradually expanded axisymmetrically until a constant stiffness value was reached, as described in chapter 4.2. More detailed investigation of the crack propagation in rock is out of the scope of this thesis. Further investigation on this aspect is recommended with using more elaborated modelling techniques. Fracture analysis can be carried out in ANSYS by defining an initial crack and by 'killing' the elements that have undergone failure. Interesting results would, also, yield a discrete element method (DEM) analysis, for example in ANSYS Rocky software. DEM is able to follow a discrete approach of analysing the bulk behaviour of rocks and granular material as an idealised assembly of particles, in a micro-mechanical level. The interaction and contact interface behaviour of the various particles of rock can numerically be translated to velocity and displacement of the material, yielding accurate results. Additionally, discontinuities in rock and different level of disturbances can be taken into account with software used by geotechnical engineers, such as PLAXIS. The empirical failure criterion of Hoek-Brown is available in such software, providing the ability to consider more thoroughly the quality of the rock mass under investigation when failure occurs.

The analysis on the cutting toe – rock interaction yielded the result of the high dependence of the stiffness of the rock cutting operation on the angle at which the tool penetrates the rock. Additionally, a quite conservative scenario is taken into account by considering only linear properties and omitting the potential failure of rock. As discussed, implementing failure in the finite element analysis results in a reduction of almost 20% in the resulting resistance of rock in breaking. Besides the damage in the rock mass, the potential failure of the monopile and the cutting toe needs to be investigated, as it would lead to failure of the drill-drive operations. This is done in the following chapters of this thesis.

5 Pile Tip Buckling

5.1 Introduction to the Monopile Model

The next step in the analysis procedure is to investigate the structural integrity of the monopile under static loading. The possible failure modes of the monopile during a driving operation was already discussed in chapter 2.6. The damage induced by the drill and the drilling procedure is out of the scope of this thesis, assuming that the pile suffers no damage when the rock borehole is drilled.

Stability problems arise from the low slenderness ratio of the monopile, while the high stresses in the pile tip could cause excessive deformation. A series of buckling analyses was carried out in order to quantify those dangers and evaluate the capacity of the monopile structure to resist the driving load and the stresses arising from the resistance of rock during the breaking process. The cross-sectional dimensions of the monopile can be seen in Figure 5.1. The thickness of the pile shell is assumed to be constant through the entire length, meaning that no driving shoe is considered.

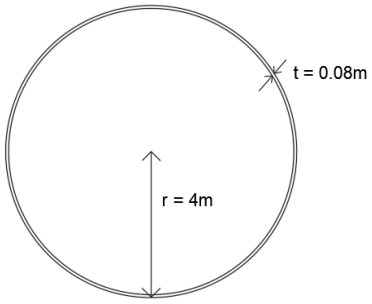

Figure 5.1: Cross-section of the monopile foundation.

A pile of 15m length was modelled following the rule of thumb that a length double the diameter is most of the times sufficient to capture accurately the local buckling behaviour. This decision is investigated and discussed thoroughly in chapter 5.4.1. Second order 3D solid elements were used for modelling the pile (Figure 5.2). The elements have 20 nodes with three degrees of freedom per node: translations in the nodal x, y and z directions. The elements support plasticity, stress stiffening and large displacements, making them suitable for both linear and non-linear buckling analysis.

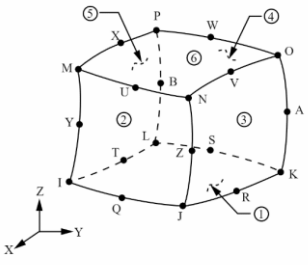

Figure 5.2: Solid hexahedral element.

According to literature on similar geometry piles, 2 elements over the thickness of the shell are deemed sufficient to capture the bending deformation and plate buckling behaviour. A hexahedral mesh size of 0.2x0.2m was used for the entire length of the pile (Appendix B9). Figures from the ANSYS environment are provided below:

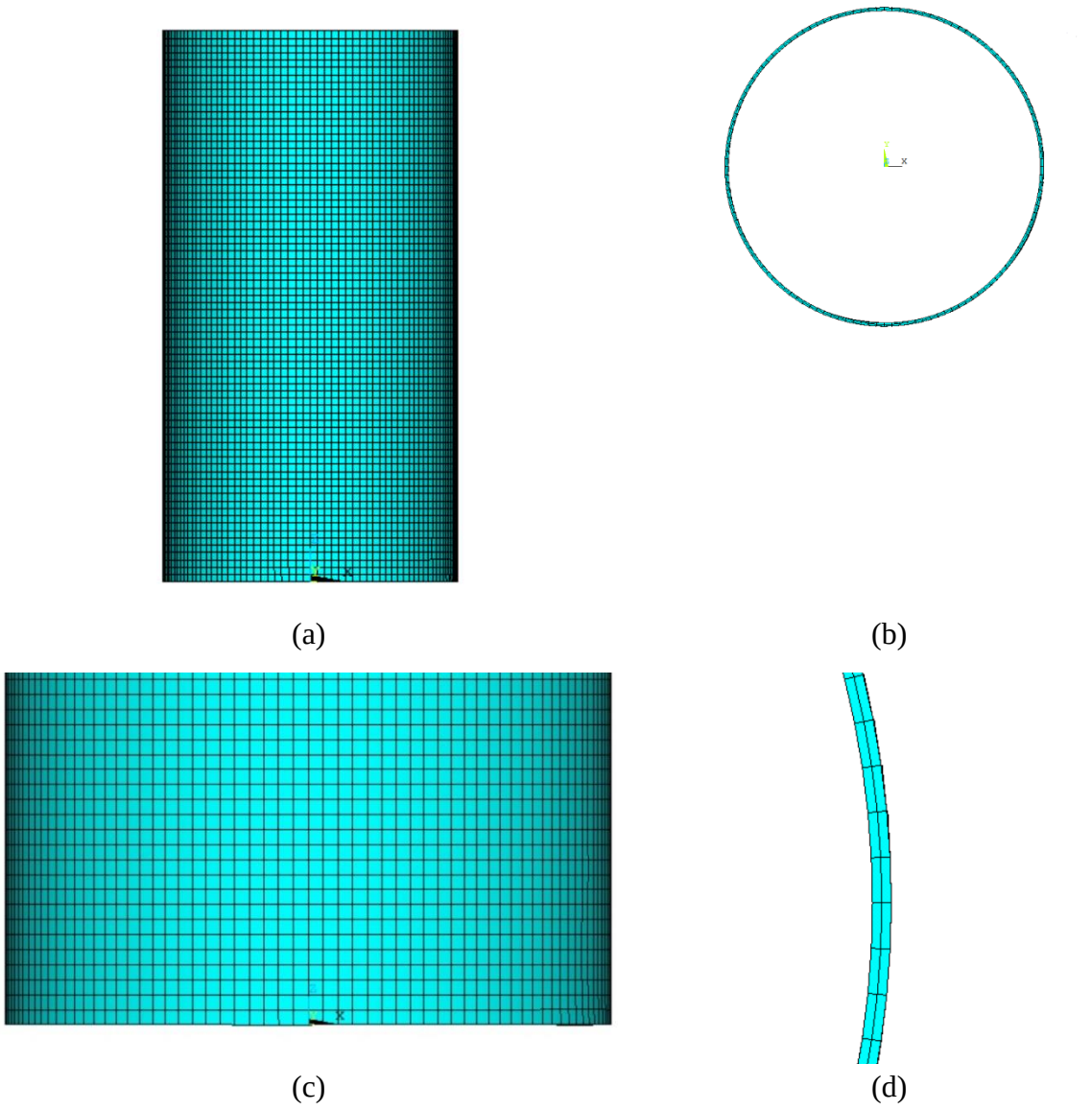

Figure 5.3: Mesh of the monopile model: Side view (a). Cross-section (b). Pile tip close-up (c). Cross-section close-up(d).

The rock medium expands infinitely around the monopile and is characterised by very high stiffness due to the high confinement pressure. This means that, in practice, the small radial deflections of the monopile during driving are not able to cause significant deformations to the walls of the borehole. By following that reasoning, the rock around the monopile is modelled as a fully fixed cylinder, enclosing the pile. The same, as the pile, 3D solid elements are used with an identical mesh size. Contact is defined between the monopile and the rock, by designating the rock as the target surface and the pile as the contact surface.

The same uncertainty as in the case of toe-rock interaction governs the friction conditions in the interface of pile and rock. It is not possible to know a priori the friction coefficient values, which can be determined only by on-site testing and by closely observing the response of the monopile and rock during the drill-drive installation. To overcome this uncertainty, an investigation of the monopile's response under static loading for different friction coefficient values was carried out in chapter 5.4.5.

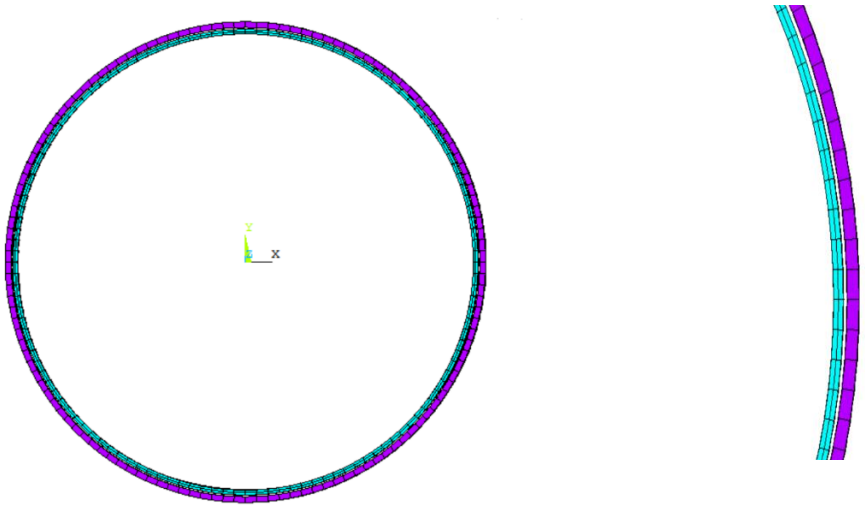

(a) (b)

Figure 5.4: Monopile (in blue) and rock borehole (in purple) cross-section mesh (a). Close-up view (b).

The resistance of the rock in the pile tip, resulting from the cutting toe-rock interaction during the breaking process, is implemented in the monopile model by a series of non-linear springs, uniformly distributed in the bottom circumference of the pile. The springs connect the mid-thickness nodes of the pile with fixed nodes located just below them, namely 2 nodes per spring element, as seen in Figure 5.6. The bottom node of the spring element is fixed, representing the immovable ground, and the choice of connecting only the mid-thickness nodes was made for representing a hinged support of the pile. Non-linear spring elements are used with longitudinal-only force-displacement capability. In practice, the rock would provide resistance only when compressed. Hence, the non-linear spring elements are defined to be active only in compression, having a unit stiffness when in tension. Unit stiffness in tension was used instead of zero, because the latter would induce instabilities in the numerical analysis. The stiffness of the springs in compression is determined from the stiffness of the rock cutting operation estimated in chapter 4.6, with the correct transformation of the distributed, per mm of circumference, value to the values for the discrete spring elements positioned in the bottom of the pile. In the ANSYS environment, the stiffness of the non-linear spring elements is considered by defining the force-deflection curve that they follow. Attention should be given to the correct designation of the compressive and tensile quadrant, which depends on the determination of the start and end node of the element.

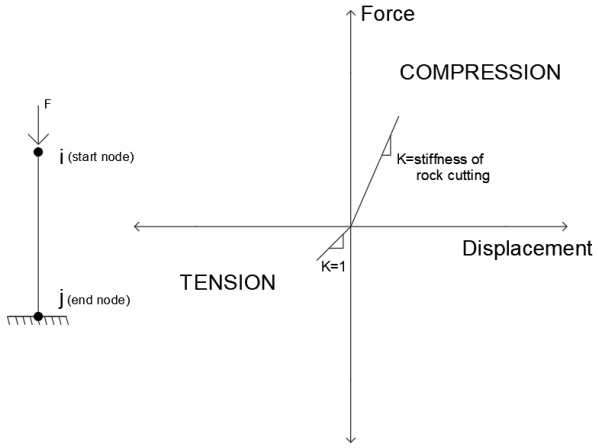

Figure 5.5: Force-displacement graph definition for non-linear springs.

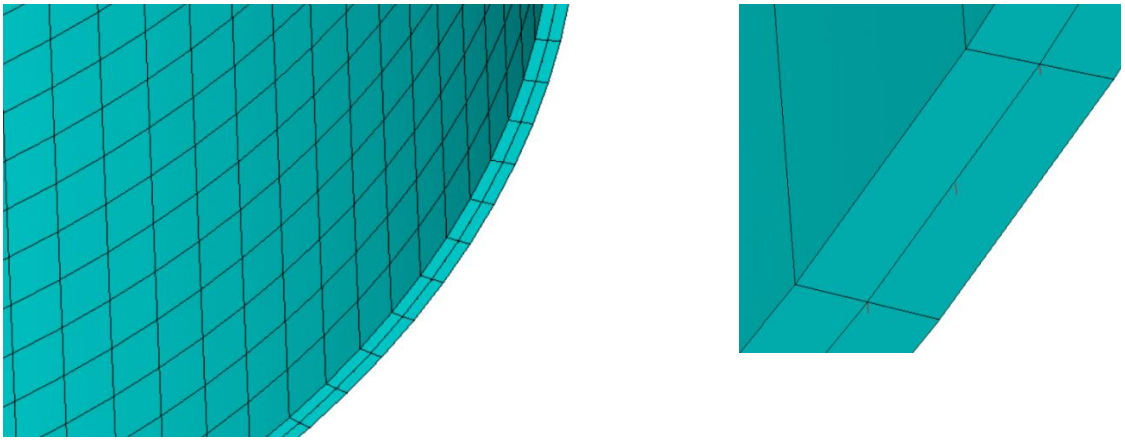

(a) (a)

Figure 5.6: Non-linear spring elements (in red) in the bottom circumference of the pile (a). Close-up view (b).

A web of rigid beam elements (Figure 5.7) was introduced in the top face of the monopile in order to simulate a hinge. They follow the Timoshenko beam theory and have six degrees of freedom per node, namely translations and rotations in the x, y and z nodal directions. The elements connect the nodes of the top pile face with a 'master' node located in the center of the pile, which is fixed against translation in x, y and rotation about z direction.

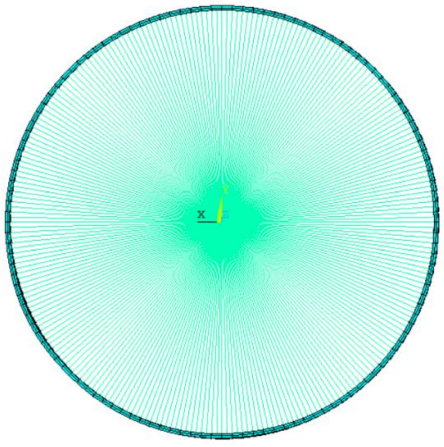

Figure 5.7: Rigid beam elements connecting the nodes of the top monopile cross section with a 'master' node in the centre.

5.2 Linear Buckling

In this chapter, fixed boundary conditions are applied to both the top and bottom face of the monopile. No rock-structure interaction is considered, due to lack of analytical formulas in the shell theory.

Firstly, the ANSYS results of linear buckling analysis are compared with the critical buckling load obtained from the shell buckling theory of axially compressed cylinders. Linear buckling or Eigen-Buckling analysis is able to predict the critical buckling load under compression that would result in the structure experiencing instability and collapse, losing its load bearing capabilities. This critical load corresponds to the bifurcation point in the applied force - displacement graph of the structure. After reaching that load, only small additional loading would produce infinite displacements. The biggest drawback of linear buckling analysis is that assumes ideal linear elastic structures without taking into consideration any non-linearities or imperfections. By doing so, Eigen-buckling analysis overestimates the critical buckling load of structures and should be avoided in most cases of engineering practice. Numerically-wise, the linear buckling analysis requires less computational time than a non-linear one and can provide useful initial insight in the response of a structure under compression.

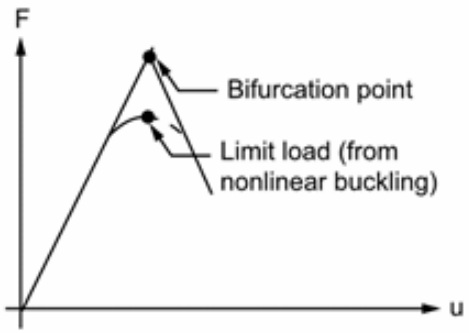

Figure 5.8: Force-displacement curve including the bifurcation point of instability.

The steps for performing Eigen-Buckling analysis in ANSYS are:

1. Perform static analysis activating prestress effects. By doing so, the stiffness matrix of the structure is updated in order to account for stress stiffening due to loading.
2. Apply unit load. Perform Eigen-Buckling and obtain the eigenvalues and the corresponding buckling mode shapes. Because unit load was applied, the eigenvalue actually represents the buckling load. The smallest buckling load is the critical load that would cause instability to the structure.

By following the abovementioned procedure, linear buckling was performed to the monopile model described in chapter 5.1. Only linear behaviour is considered in Eigen-Buckling. This means that if non-linearities are defined, such as contact, they are ignored by the software. In the case of contact elements, their stiffness is determined based on their initial status and it is not updated during the solution. For that reason the rock was not included in the model. The steel properties are linear, elastic, isotropic with Young's Modulus of 210 GPa and Poisson's ratio of 0.3.

Uniform unit compressive pressure was applied in the top face of the monopile. Fixed constraint conditions are applied in both the bottom and top face of the monopile.

The shell buckling theory predicts local buckling of a cylinder and it is independent of the boundary conditions. The Eigen-Buckling analysis of the monopile in ANSYS yielded a critical buckling stress of $2456.9\ MPa$ with the buckling shape shown in Figure 5.9.

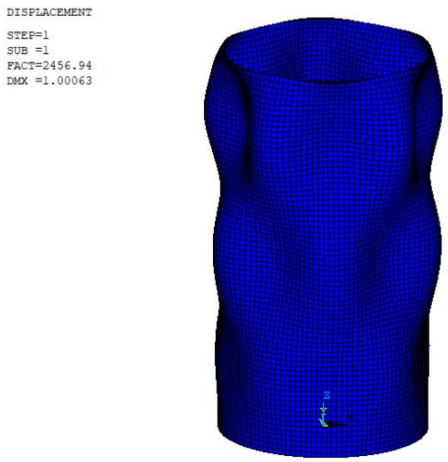

Figure 5.9: Critical elastic buckling shape for a fixed cylinder in ANSYS. (scale factor =500)

According to shell buckling theory, the Batdorf parameter (Z) is defined as:

$$Z = \frac{l^2}{rt}\sqrt{1-\nu^2} = 677.51 \qquad 5.1$$

where, l is the length of the cylinder

The critical buckling stress of a cylinder is then determined from the following expression:

$$\sigma_{cr} = \frac{\pi^2 E}{12(1-\nu^2)}\left(\frac{t}{l}\right)^2 * \frac{4\sqrt{3}}{\pi^2} Z = 2567.6\ MPa \qquad 5.2$$

The theoretical buckling load is similar to the ANSYS buckling load.

5.3 Non-Linear Buckling

In this chapter, non-linear buckling analysis was performed in the same monopile model that was used in the previous chapter. A comparison between the FEM results and the regulations of DNVGL C202 was made as a first validation of the derived numerical modelling buckling strength. Non-linear analysis provides the ability to include material and geometric non-linearities and imperfections in a static analysis with step-wise increased load, until instability occurs in the structure. Material non-linearity is taken into account by defining a plasticity material law, introducing a stress-strain curve that the structure will follow until it reaches failure.

By including geometric non-linearity, the analysis stops to assume small displacements and introduces P-δ effects instead. As P-δ effects, the additional moments that will be introduced to the structure, due to load eccentricity, as it deflects sideways are defined.

Moreover, by activating large displacements, the change in stiffness as the structure undergoes deformation is taken into account. Finally, imperfections have been proven to affect the structure's buckling response and reduce significantly its ability to resist compressive loads. Non-linear buckling analysis provides accurate results for the design of actual structures, but increases dramatically the computational time and, sometimes, introduces convergence problems.

The procedure for performing non-linear buckling analysis in ANSYS is:

- Perform Eigen-Buckling analysis and determine the critical buckling shape and its maximum deflection of interest.
- Update the geometry of the model using the critical buckling shape, scaled for accounting imperfections. The scale factor is δ/d_{max}, where δ is the theoretical imperfection and d_{max} is the maximum related displacement from the critical buckling shape.
- Define a material law.
- Impose load sufficient to trigger instability.
- Run static analysis with large displacements on. Choose sufficient number of steps for incrementally applying the load.
- When the solution starts to diverge, the structure has experienced buckling. To rule out numerical instability, the force-displacement curve is plotted. If the force (or stress) reaches a plateau when divergence initiates, then the instability is physical.

The post-buckling behaviour of the structure can be investigated by using deflection-controlled loading.

The procedure above was followed for the GMNIA of the monopile structure described in chapter 5.1. Fixed boundary conditions were applied at both the top and bottom face. Imperfections were included according to the fabrication tolerances described in DNVGL-OS-C401. The code considers the following tolerances when the buckling of circular cylindrical shells, with radius r, length l and thickness t, is analysed:

Maximum deviation from the nominal radius:

$$\delta = 0.005r = 20mm \tag{5.3}$$

Local out of roundness:

$$\delta = \frac{0.01g}{1+\frac{g}{r}} = 18.23mm \tag{5.4}$$

where, $g = \min\left(1.15\sqrt{l\sqrt{rt}}, \frac{\pi r}{2}\right) = 3349.9$

Local out of straightness:

$$\delta = \frac{0.01g}{1+\frac{g}{r}} = 14.45mm \tag{5.5}$$

where, $g = \min\left(l, 4\sqrt{rt}\right) = 2262.7$

To account for the worst-case scenario, the maximum imperfection tolerance was used as input in ANSYS, namely $20mm$.

Steel grade of S355 is assumed, a common material used for monopiles designed by Van Oord. The true stress-strain curve of steel is used as input in ANSYS according to DNVGL-RP-C208, in order to take into account strain-hardening effects and the true behaviour of the material. The stress-strain curve for S355 steel, for shell of thickness between 63mm and 100mm, is shown in the figure below. No material factor was considered on the material side.

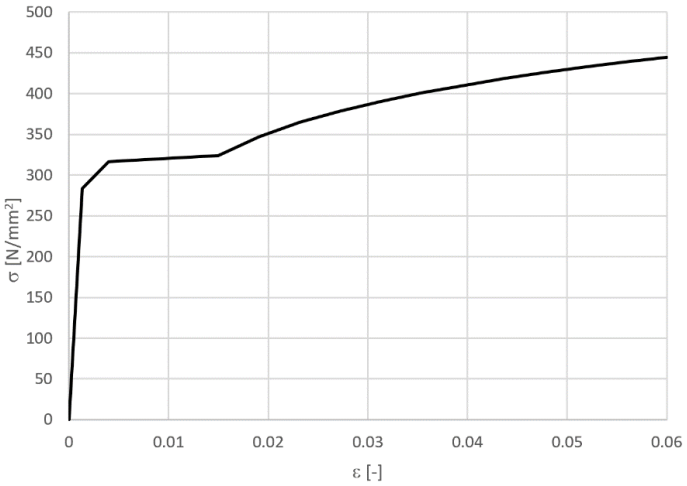

Graph 5.1: Stress-strain curve for S355 according to DNVGL-RP-C208.

The geometry of the model was updated using the eigen-buckling mode shape depicted on Figure 5.9, following a linear buckling analysis. A new uniform compression pressure of 500 MPa was applied on the top face and static analysis was run, with large displacements on. The solution showed divergence for an applied stress of 301 MPa. The design value can be obtained by applying the material factor on the load side. Hence, the design buckling load is :

$$\sigma_{cr,d} = \frac{301}{\gamma_M} = \frac{301}{1.15} = 261.7\ MPa$$

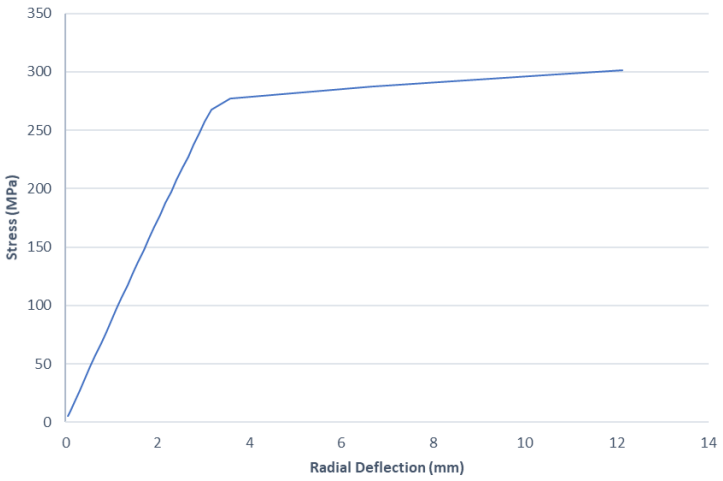

Graph 5.2: GMNIA of fixed monopile in ANSYS.

The reduced buckling strength of the cylinder, including imperfections, was determined following the regulations of DNVGL-RP-C202, and is described below:

The Batdorf parameter (or curvature parameter) was already calculated in chapter 5.2 equal to $Z = 677.51$.

The buckling coefficients for axial stress are:

$$\psi = 1 \tag{5.6}$$

$$\xi = 0.702Z = 475.61 \tag{5.7}$$

$$\rho = 0.5\left(1 + \frac{r}{150t}\right)^{-0.5} = 0.43 \tag{5.8}$$

$$C = \psi\sqrt{1 + \left(\frac{\rho\xi}{\psi}\right)^2} = 206.2 \tag{5.9}$$

The elastic buckling strength of the cylinder is:

$$f_E = C\frac{(\pi^2 E)}{12(1-\nu^2)}\left(\frac{t}{l}\right)^2 = 1113.26\ MPa \tag{5.10}$$

The reduced slenderness is calculated as:

$$\lambda_s^2 = \frac{f_y}{f_E} = 0.32 \tag{5.11}$$

The design critical buckling strength is then:

$$\sigma_{cr} = \frac{f_y}{\sqrt{1+\lambda_s^4}} * \frac{1}{\gamma_M} = 284.5\ MPa \tag{5.12}$$

where, $\gamma_M = 1.18$

The results of ANSYS and the code show acceptable convergence, with the difference resulting from the imperfections assumptions.

5.4 Monopile Buckling, Considering Interaction with Rock

5.4.1 Modelled Monopile Length

The literature findings suggest that in order to increase the bearing capacity of the monopile, both during driving but also during the service-life, it is common practice to embed the pile into the rock approximately 2-3 times the shaft diameter. Considering good quality rock and based on previous calculations and observations of Van Oord, a 15m embedment depth is assumed to be sufficient. The total monopile length is 100m.

Modelling the entire length in ANSYS would increase significantly the computational analysis time. That created the motivation for investigating the possibility to model only a segment of the pile that would still be able to capture accurately the buckling behaviour. A series of Eigen-buckling analysis was carried out on the monopile model, described in chapter 5.1, for different pile lengths. Rock was not included around the pile, therefore non-linearities are not part of this investigation. The results are presented in Graph 5.3. It can be seen that a simulated pile length of 15m is sufficient to produce accurate results of local buckling, with the value of the critical stress being constant for further increase of the length.

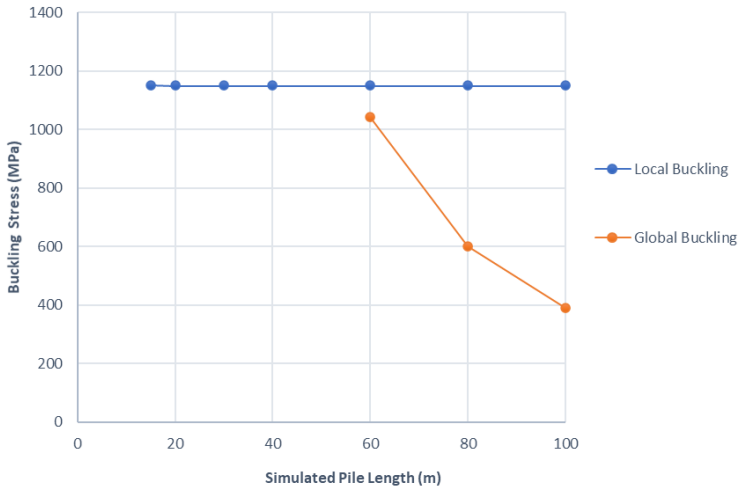

Graph 5.3: Buckling stress for models with different monopile length.

The shape of the local buckling failure mode is shown in Figure 5.10 for the 15m pile, demonstrating that the instability occurring in the pile is a result of the pile tip buckling.

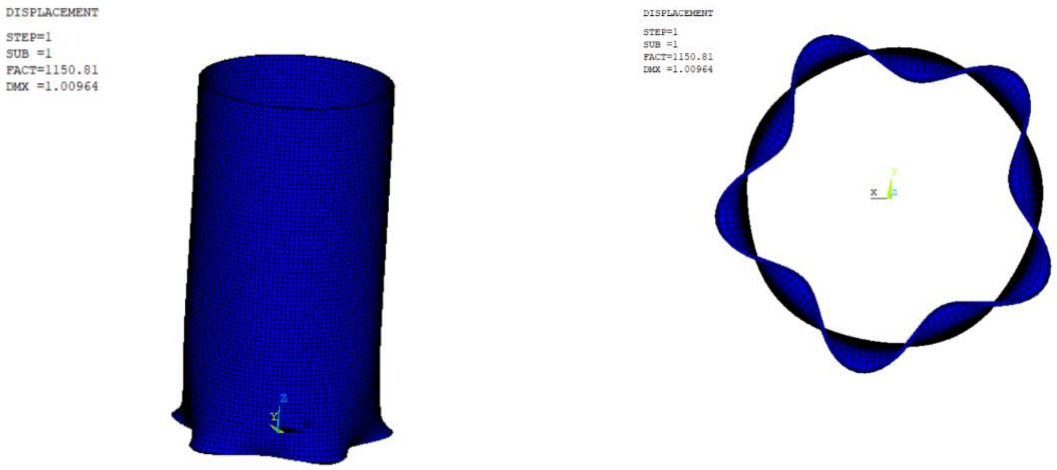

(a) (b)

Figure 5.10: Pile tip buckling for monopile of 15m length, considering rock interaction. Side view (a). Cross-section (b).

Graph 5.3 also shows that the pile starts to experience global buckling when the length becomes bigger than 60m. In practice, global buckling during driving will be prevented by the use of a gripper that provides lateral support to the monopile until it is sufficiently embedded into the rock. At this moment, the gripper is released and the rock around the pile will prevent the monopile from deflecting sideways and buckle.

Therefore, the global buckling failure mode is prevented at all times and only local buckling is investigated in the following chapters of this thesis. This conclusion coincides with the findings from literature which point out to local pile tip buckling as the governing failure mode of piles that are driven in hard soil conditions (Randolph, 2018).

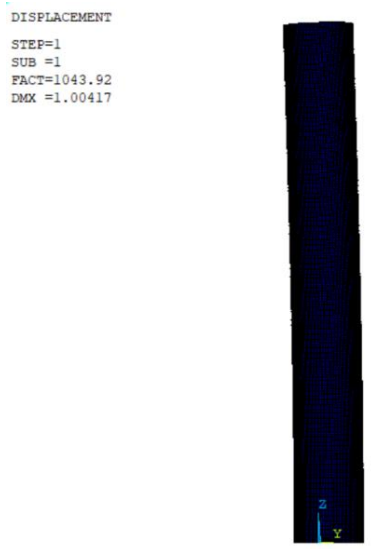

Figure 5.11: Global buckling for monopile of 60m length.

5.4.2 Monopile GMNIA

The stability of the monopile during driving was investigated by performing non-linear buckling analysis and considering the interaction with rock. The resistance of rock to the vertical motion of the pile was introduced by spring elements with the stiffness of the cutting operation for granite and sandstone, calculated in chapter 4.6.

Rock Type	Stiffnes/spring (N/mm)
Granite	882532.3
Sandstone	647609.9

Table 5.1: Stiffness value per spring element for granite and sandstone rock properties.

The non-linearity that is introduced by the contact definition between the pile and the walls of the borehole and by the response of the compression-only spring elements will be ignored from ANSYS during an Eigen-Buckling analysis. This would result to an inaccurate critical buckling shape, that will eventually be used for updating the geometry of the pile. Hence, an alternative approach was followed for obtaining the correct linear buckling shape. Linear spring elements were used that are activated both in compression and tension (with the same stiffness value). The eigen-buckling analysis was performed according to the procedure in chapter 5.2, without rock around the pile.

The results of this analysis were post-processed as follows:

- The nodes of the outer pile surface that tend to move outwards in the critical buckling mode were located. In reality, these nodes would not be able to move due to the existence of rock. Thus, they were constrained from deflecting radially.
- The spring elements that are in tension in the critical buckling shape are determined. In reality, those springs would not impose any resistance to the monopile. Thus, they were removed from the model.
- A new Eigen-Buckling analysis was run for the modified model. The critical buckling shape was used for updating the pile's geometry. The radial constraints were removed, the non-linear springs were included uniformly in the bottom circumference and the rock was modelled around the pile. Then, non-linear buckling analysis was performed according to the remaining steps mentioned in chapter 5.3.

5.4.3 Imperfections

Imperfections in the pile structure due to fabrication mistakes or mistreatment during transportation or lifting cannot really be avoided. Therefore, including them in the non-linear buckling analysis of the monopile is very important. First, they are needed for triggering the instability in the numerical analysis, but most importantly they introduce irregularities in the structure that can considerably worsen its ability to resist loads. Especially when analysing the driving of piles in hard soil, where pile tip buckling is of great concern, not accounting for possible imperfections leads to unconservative results as was pointed out in literature (Bhattacharya et al., 2005).

An investigation of the imperfection shape that yields the most unfavourable buckling performance of the monopile was carried out in ANSYS. It is noted that the imperfection that is introduced in the model results from updating the initial geometry with a scaled eigen-buckling shape. Hence, the final geometry of the monopile is a product of a scale factor and a buckling shape, derived from linear buckling analysis. The scale factor is chosen as the most conservative imperfection that the DNV code suggests, namely a deviation from the nominal radius of 20mm (see 5.3).

Five different buckling modes were introduced as imperfection: two with local buckling located only at the pile tip, two with buckling waves along the length of the pile and one with ovalisation towards the bottom part of the pile. An asymmetrical buckling shape, if it is triggered, requires smaller compression load than a symmetrical one for the same structure, making it the governing failure mode. Hence, asymmetrical buckling modes were chosen. Moreover, the modes with the smallest elastic critical buckling stress were selected for each type of deformation, either located at the tip or distributed along the length. For the buckling modes with waves along the length, the nodes were not constrained radially for obtaining the eigen-buckling mode, as done with the rest.

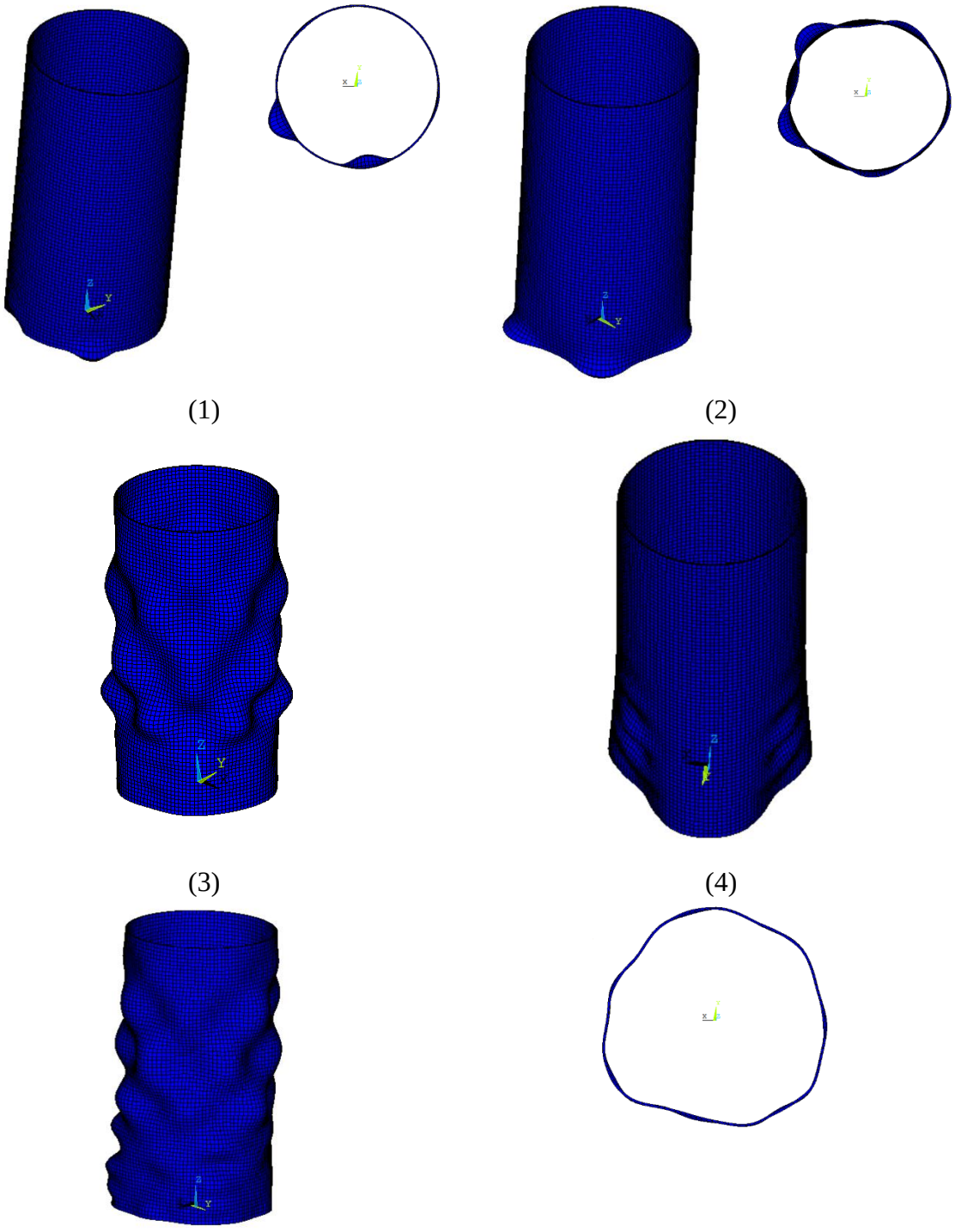

Figure 5.12: Introduced imperfection shapes.

The (absolute) value of the radial deflection for different levels of applied load is plotted in Graph 5.4, using sandstone rock properties. The 1st imperfection results in the smallest critical buckling stress, approximately 250 MPa. Hence, avoiding imperfections that are extensively concentrated in the bottom cross-section would lead to slightly better buckling performance of the monopile. It is noted that the 2nd imperfection is not included in Graph 5.4.

However, a comparison was made for granite properties between the 1st and 2nd imperfection, which showed that both yield an almost identical critical buckling stress. For the record, the critical buckling stress for driving in granite is approximately 255 MPa.

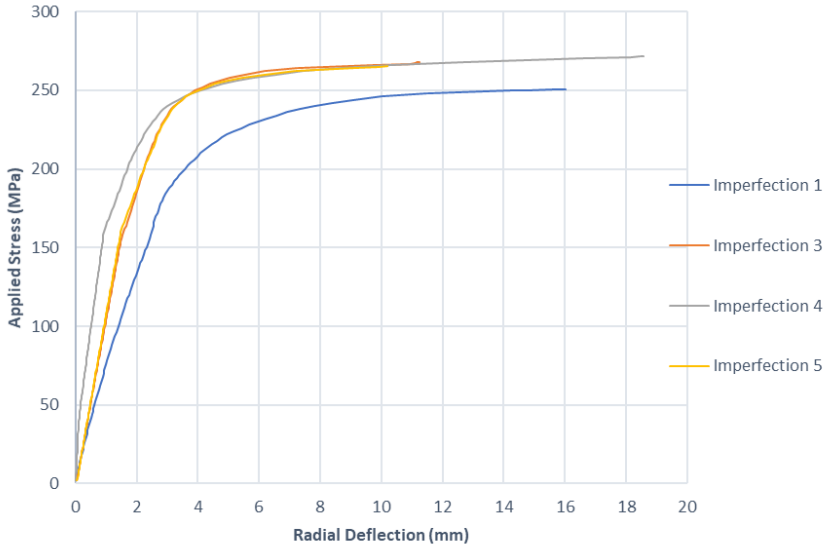

Graph 5.4: GMNIA results for different imperfections

The critical cross-section for local buckling is the monopile tip for all introduced imperfections, agreeing with the literature findings that highlight the tip buckling as the governing failure mode in pile driving in hard soil. Depending on the initial imperfection shape and considering the fact that the pile tries to buckle outwards, the final deformation shape consists of parts of the tip cross-section that have buckled inwards, after meeting resistance in lateral deflection from the borehole walls, and parts that have buckled outwards.

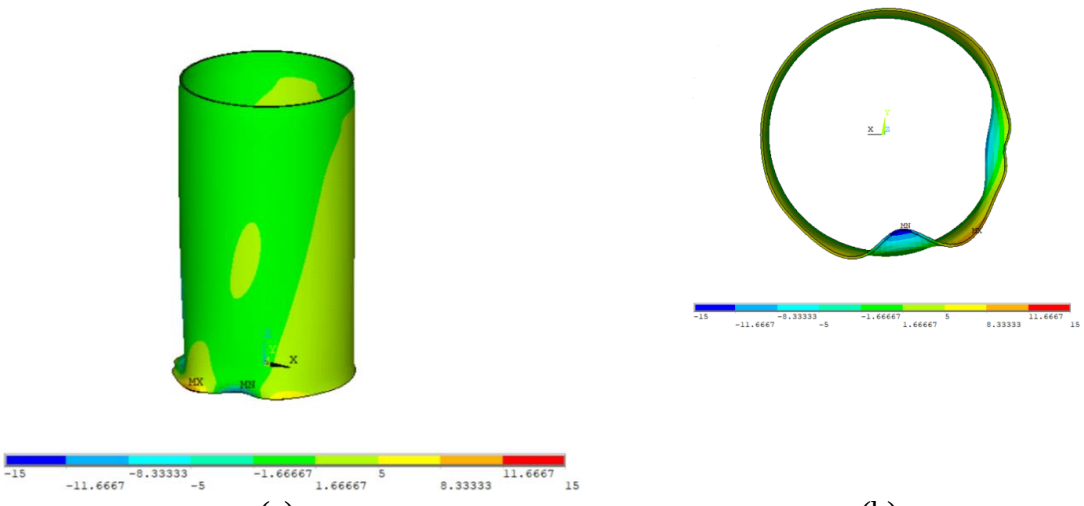

(a) (b)

Figure 5.13: Radial deflection (mm) for monopile GMNIA with imperfection 1. Side view (a). Cross-section (b). (scale factor =50)

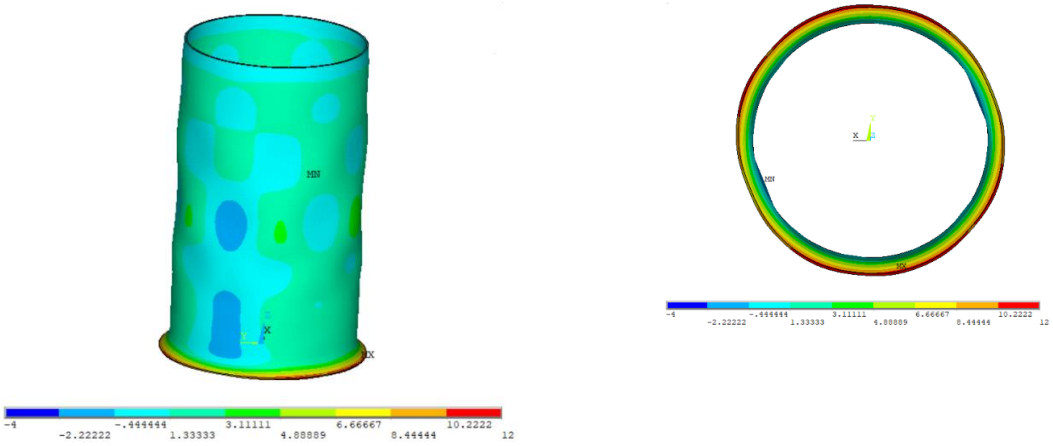

(a) (b)

Figure 5.14: Radial deflection (mm) for monopile GMNIA with imperfection 3. Side view (a). Cross-section (b). (scale factor =50)

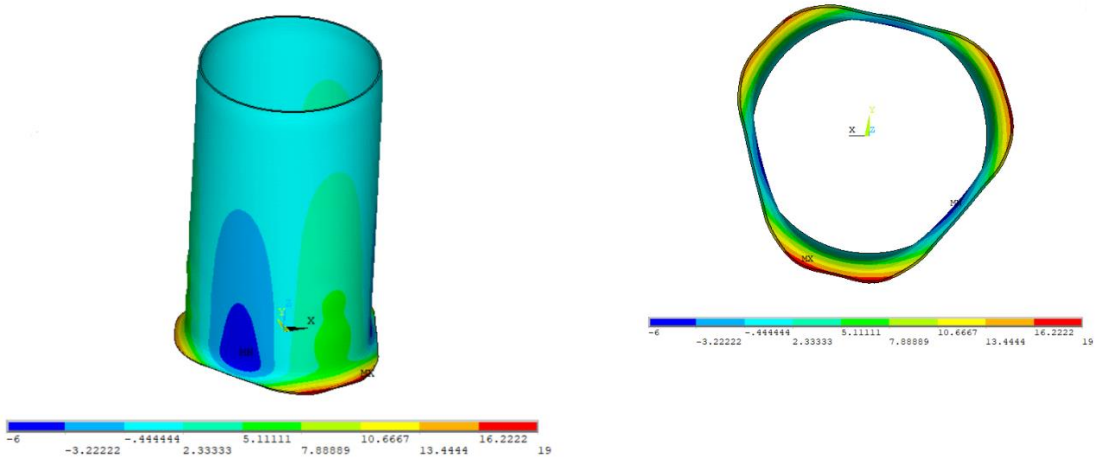

(a) (b)

Figure 5.15: Radial deflection (mm) for monopile GMNIA with imperfection 4. Side view (a). Cross-section (b). (scale factor =50)

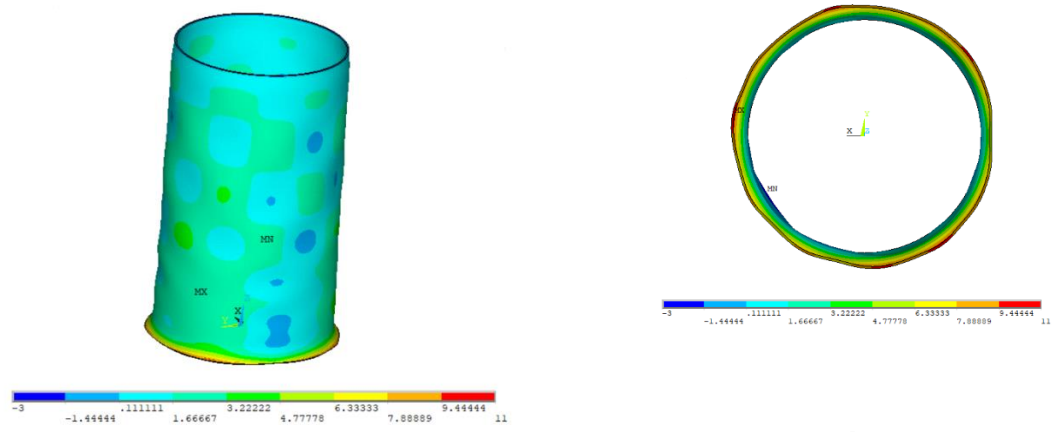

(a) (b)

Figure 5.16: Radial deflection (mm) for monopile GMNIA with imperfection 5. Side view (a). Cross-section (b). (scale factor =50)

5.4.4 Effect of Borehole on Pile Buckling

Lateral restraints may prevent the buckling of the monopile walls, increasing its ability to resist loads. In the case of this research, the rock around the monopile could have a beneficial effect in the stability during driving. For this reason, the buckling behaviour of the monopile is investigated both when no rock is modelled around it, representing the conditions of the first hammer blow that will initiate the penetration in the seabed, but also when the pile is fully embedded in rock. The results of the non-linear analysis indicate that including the rock borehole in the simulation leads to only a marginal increase in the critical buckling stress of the structure.

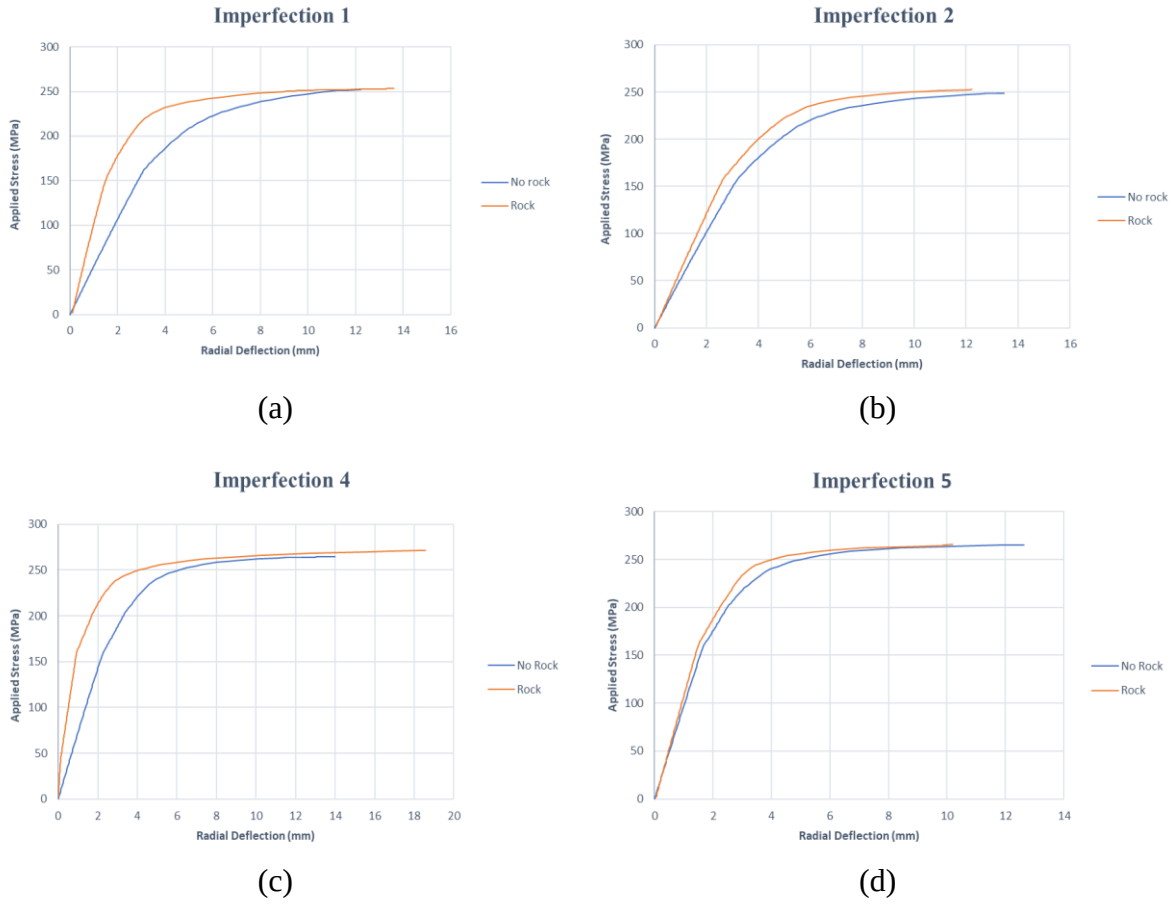

Graph 5.5: Applied Stress – Deflection GMNIA results for models with and without rock borehole.

Graph 5.5 shows that including the rock borehole in the simulation results in a stiffer buckling behaviour of the monopile, with smaller deflections for the same applied stress, when compared to the ANSYS models without rock enclosing the pile. However, the critical load that will trigger instability and eventual collapse in the structure is not affected substantially by the presence of rock around the pile. As proven in 5.4.3, the pile tip is the critical cross-section for local buckling, meaning that the behaviour of this cross-section will determine the ability of the pile to resist the driving forces. The limited effect of the rock borehole can be explained by looking at the introduced imperfections and final deformation shape of the tip cross-section (Figure 5.17).

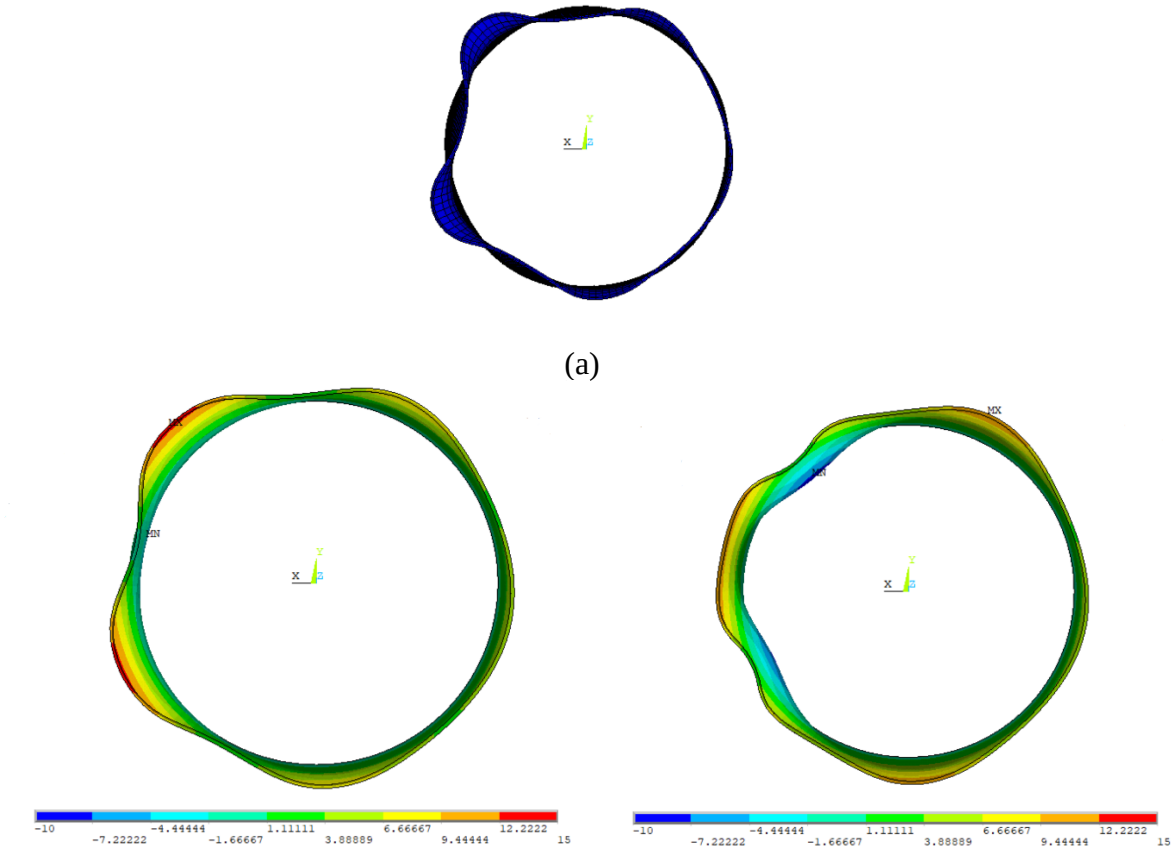

Figure 5.17: Pile tip cross-section's radial deformations (mm). Initial imperfection (a). No rock included (c). Rock enclosing the pile (c). (scale factor=50)

The initial shape of the pile includes inward and outward buckles of the tip cross-section. Only the outermost buckle of the pile tip is initially in contact with the rock around the pile. As the structure is loaded in axial compression, the pile tip has the tendency to buckle outwards. However, rock prevents the most outward buckle to further expand radially. Instead, the rest of the cross-section will move outwards and would hit the walls of the rock borehole after travelling a distance equal to the relative distance between the furthest outward buckle and each buckle in consideration. ANSYS yielded a maximum radial deflection of approximately 12 mm (Figure 5.17c) for imperfection 2 and considering that a maximum deviation from nominal radius of 20 mm was introduced as imperfection in the model, means that only the parts of the cross-section that had at least an 8 mm outwards buckle, initially, will be in contact with the rock in the final step. As seen in Figure 5.18, only a small part of the pile tip cross section is eventually restrained by the rock, which is even smaller before the driving load reaches the critical one. Concluding, rock provides negligible lateral restraint to the pile tip, therefore not improving its local buckling capacity.

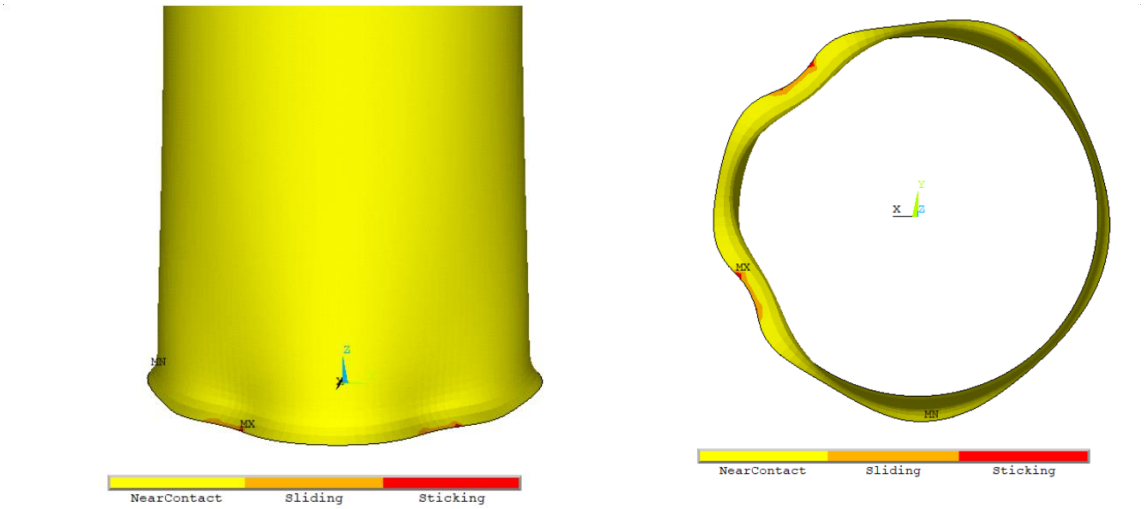

(a) (b)

Figure 5.18: Monopile-Rock contact status at the critical buckling load (imperfection 2). Side view (a). Bottom view (b).

Introducing imperfections with buckling waves located along the length of the pile results in the same buckling behaviour. Once again, the bottom cross-section will be the one triggering the instability in the structure. Trying to buckle outwards, the pile tip has to expand radially significantly before it experiences any lateral restraint from the rock. Depending on the maximum tip deflection and the initial distance from the rock wall, it is possible that the pile tip will not be restrained at all until local buckling occurs.

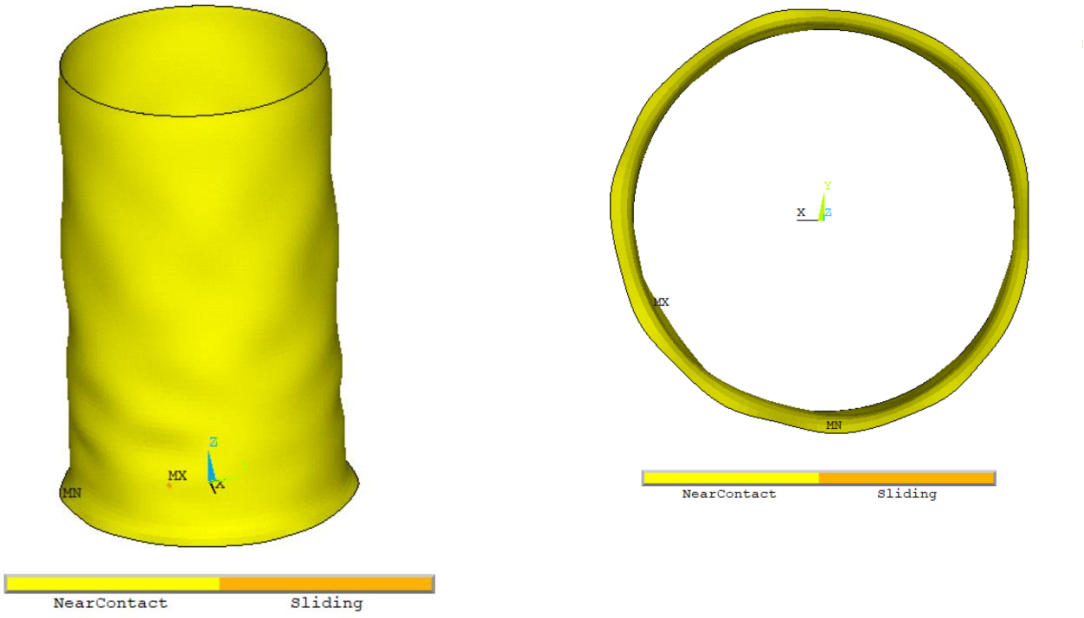

(a) (b)

Figure 5.19: Monopile-Rock contact status at the critical buckling load (imperfection 5). Pile tip is not in contact with the rock. Side view (a). Bottom view (b).

5.4.5 Friction Coefficient

According to the experimental research of E.S. Gaffney (1976), the friction coefficient between steel and rock for different types of rock ranges between 0.14 and 0.5 for dry conditions, with the value being reduced when the contact occurs underwater. The uncertainty in the response of the pile in driving and the surface conditions of the rock after drilling translates to uncertainty of determining the value of friction coefficient without tests on-site. To bypass that problem, GMNIA of the pile when driven in granite was done for different friction coefficient values, namely 0, 0.25 and 0.5. A steel of grade S355 was used and a deviation from the nominal radius was considered in order to account for imperfections. The rock material is granite. The results can be seen in Graph 5.6.

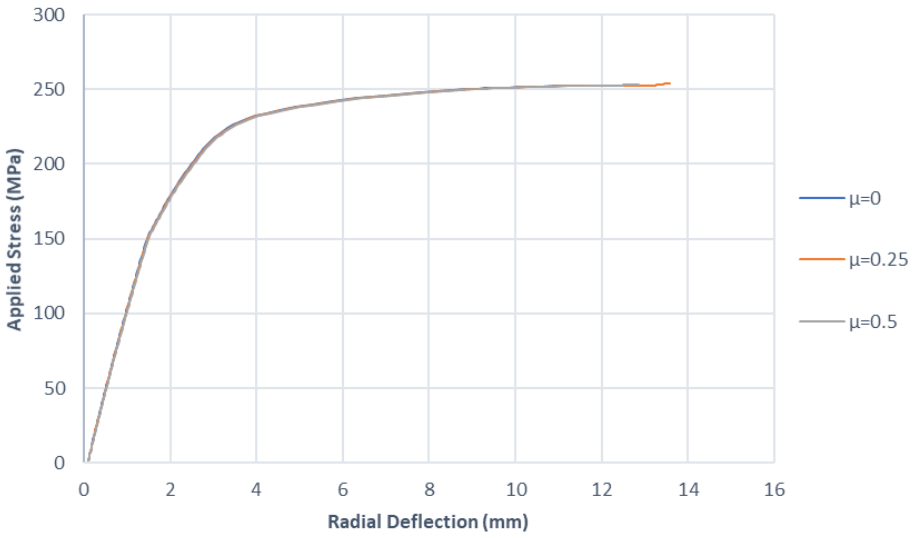

Graph 5.6: GMNIA of monopile for different friction coefficient values.

The critical buckling stress is approximately 255 MPa for all values of the friction coefficient, indicating that the interface conditions between still and borehole walls do not have an effect in the monopile's stability. Only a small part of the pile surface comes in contact with the rock borehole as discussed in the previous sub-chapter, hence the negligible effect of friction coefficient is deemed reasonable.

5.5 Buckling Results Discussion

The buckling resistance of the monopile was discussed so far without considering the rock cutting performance of the toe that is employed in its tip. The drill-drive installation in consideration can be deemed as successful when the monopile is able to reach the desired penetration depth without experiencing excessive deformation, or even preferably by staying in the elastic region throughout the entire procedure. Hence, the realization of the installation requires both the structural integrity of the monopile and the cutting efficiency of the toe to be ensured. In Table 5.2, the theoretical required force for breaking the granite and sandstone with properties according to Table 4.1 is provided. The force was calculated using the Evans rock cutting theory assuming no wear in the cutting toe.

In the third column of the table, the stress in the pile tip at the moment that instability occurs is given, considering the doubling of driving stresses as a result of the dynamic impact propagation (chapter 6.1). It can be seen that the force inducing instability is considerably bigger than the one required for breaking the rock below the rim of the pile, meaning that the pile will not experience any buckling until the rock is cut. The forces after that point are of no interest. A new hammer blow occurs and the penetration of the monopile in rock continues. Furthermore, the monopile is still in the elastic region at the moment of rock breaking, without having any permanent plastic deformation. The conclusion is reached that the monopile is safe during the drill-drive installation in granite and sandstone. No permanent deformation is expected throughout the entire installation, that would hinder the successful realization of the project.

Rock type	Theoretical Cutting Force (N)	Force at Buckling (N)
Granite	6.70E+07	1.01E+09
Sandstone	2.01E+07	9.90E+08

Table 5.2: Theoretical required rock cutting force and force at the onset of buckling.

The conclusions drawn above were made under the assumption of no wear in the cutting toe. It is clear that the consideration of damage in the toe is critical for accurately estimating the feasibility of a drill-drive installation method (chapter 7). By using the equation 2.142.15 , the allowable wear on the cutting toe can be calculated for avoiding buckling of the monopile. In that case, FC_w is assumed to be equal to the force initiating the instability.

For granite rock conditions, the allowable wear flat is :

$$WF = \frac{\frac{FC_w}{FC_s} - 0.9922}{0.5605} = \frac{15.07 - 0.9922}{0.5605} = 25\ mm \qquad 5.13$$

For sandstone:

$$WF = \frac{\frac{FC_w}{FC_s} - 0.9922}{0.5605} = \frac{49.3 - 0.9922}{0.5605} = 86\ mm \qquad 5.14$$

The investigation of the tip blunting in the cutting toe is the topic of the next chapter.

6 Cutting Toe Wear

The significance of avoiding excessive wear on rock cutting tools has already been mentioned in the previous chapters. In a drill-drive installation method, failure of the cutting toe would result in immediate stoppage of the installation process and premature driving refusal. An increase of wear in the toe translates to increase of the required force for cutting the rock. The available cutting force is nothing else than the driving stresses that reach the pile tip. The capabilities of transmitting forces to a monopile by hydraulic hammers, that are currently available on the market, are finite. Hence, the wear propagation in the cutting toe should be investigated in order to determine if the forces that are needed to break the rock during the drill-drive method are greater than the ones that the hydraulic hammer can provide.

6.1 Pile Tip Forces

In this chapter, the forces that are generated in the pile tip due to the propagating, hammer induced, wave are calculated using the 1D wave dynamics theory and the mathematical software MAPLE. The skin friction along the length of the monopile is not considered, meaning that the D'Alembert solution can be used. The resistance of the rock in breaking is implemented as a spring in the pile tip (Figure 6.1). The spring stiffness (K) is calculated as the total stiffness in the cutting toe circumference, estimated in chapter 4.6.

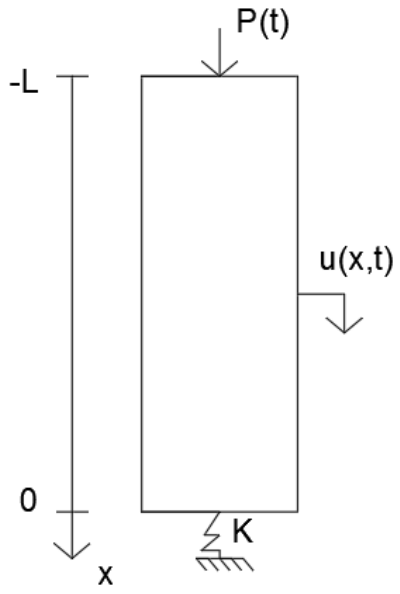

Figure 6.1: 1D representation of the monopile.

The longitudinal displacement of the monopile is given by:

$$u = f(t - x/c) + g(t + x/c) \tag{6.1}$$

The propagating wave f can be found as:

$$f(t) = \frac{c}{EA}\int_0^t P(\tau)d\tau \tag{6.2}$$

where, $P(t)$ is the hammer force and $c = 5172\ m/s$ is the wave velocity

The reflected wave is calculated from the following expression:

$$g(t) = f(t) - \frac{2K}{Z}\int_0^t f(\tau)e^{\left(-\frac{K}{Z}(t-\tau)\right)}d\tau \tag{6.3}$$

where, $Z = \frac{EA}{C}$ is the impedance of the pile

K is the spring stiffness

The pile tip force can, then, be calculated:

$$F_{tip} = EA\frac{\partial u}{\partial x}|_{x=0} \tag{6.4}$$

The full derivation can be found in the appendix.

A pulse generated by the hydraulic hammer MHU3500s by MENCK is assumed to propagate in the monopile. The hammer force was provided by Van Oord and its histogram was approximated for use in the solution mentioned above.

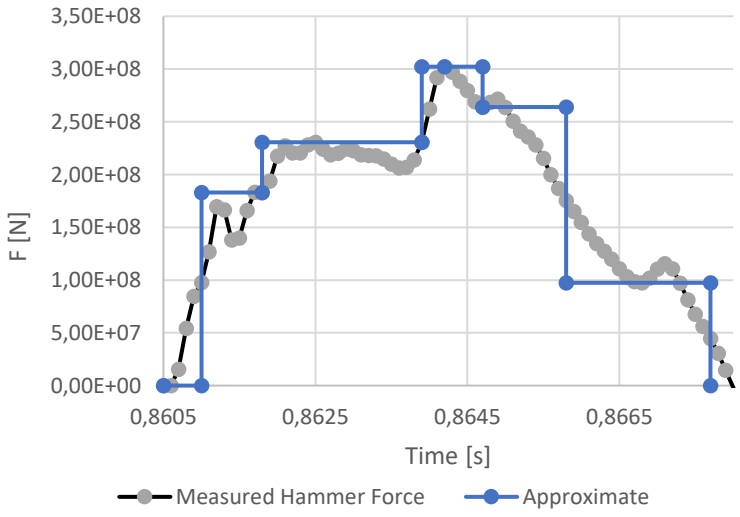

Graph 6.1: Pulse generated by MHU3500s hammer.

The solution was plugged into MAPLE and the maximum pile tip forces were determined for granite, sandstone and limestone rock properties, considering an individual hammer blow without interaction with the reflected waves from previous blows. The results are given in Table 6.1. The stronger rock will give rise to higher stresses in the pile tip, due to the higher resistance in breaking.

Stress multiplication occurs when the propagating wave reaches the pile tip, with a factor of almost 2, resembling a fixed condition. That is reasonable considering the high stiffness of the rock cutting operation.

Rock Type	Ftip (N)
Granite	5.908E+08
Limestone	5.882E+08
Sandstone	5.839E+08

Table 6.1: Maximum pile tip force for granite, limestone and sandstone.

The duration of the pulse (t_p) is $0.0072\ s$. The wavelength of the propagating wave is:

$$\lambda = c * t_p = 37.2\ m.$$

The time that is needed, after the initiation of the pulse, for the propagating wave to reach the bottom of the pile is $\frac{\Delta x}{c} = \frac{100}{5172} = 0.019\ s$, for a monopile length of 100m. A graphical representation from the MAPLE environment of the pulse propagation in granite is presented below. In the horizontal axis the length (in m) of the monopile is depicted and in the vertical axis the force (in N). Compression has a positive sign convention.

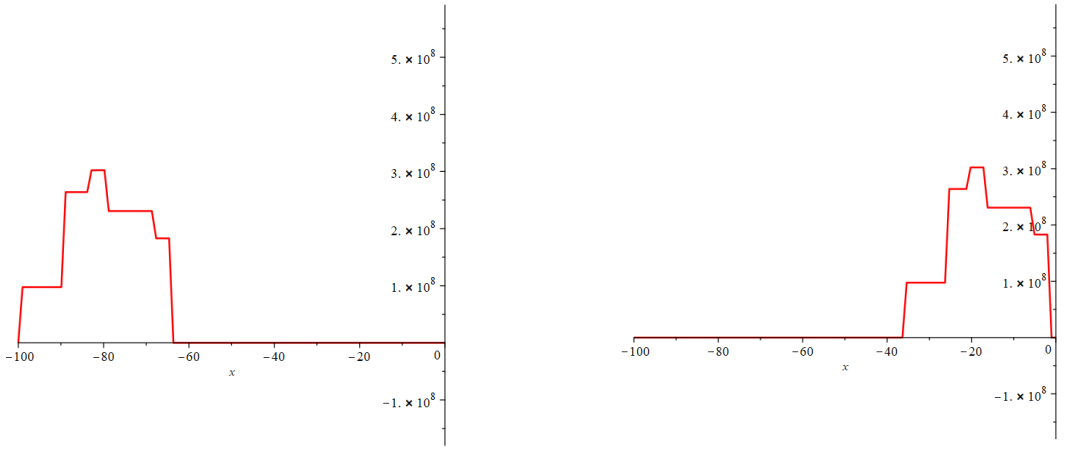

(a) (b)

Figure 6.2: Pulse propagating in the monopile. The pulse is fully developed (a). The pulse reaches the pile tip (b).

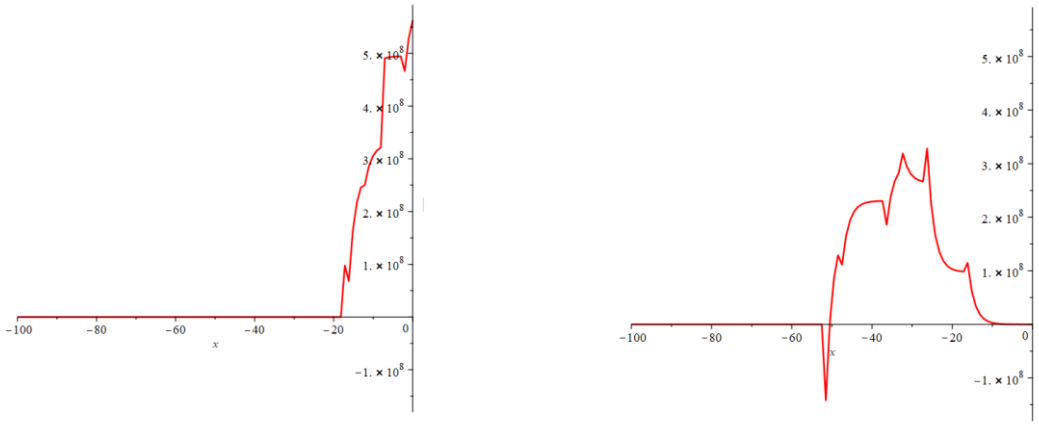

(a) (b)

Figure 6.3: The pulse undergoes distortion in the pile tip (a). The pulse is reflected with a distorted shape (b).

6.2 Toe Wear ANSYS Investigation

The investigation of wear propagation was initially attempted on ANSYS by using the toe-rock model described in chapter 4.1 and by defining a bilinear plasticity law for the toe material (Figure 6.4). The toe is made of shock resisting steel S2, having a yield strength of $f_y = 2131\ MPa$.

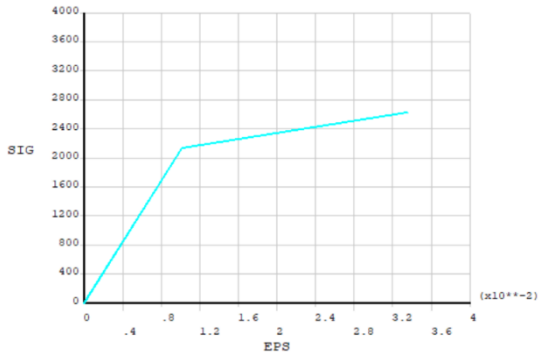

Figure 6.4: Stress-strain curve for shock resisting steel in ANSYS.

The analysis would require a significant computational time and would always stop before reaching the final load due to 'element formulation' errors. To bypass that and continue with the research an alternative approach was followed. The rock below the tip of the cutting toe is removed from the model. A contact pressure is imposed in the tip calculated with the Hertz Contact theory described in chapter 2.4, in order to take into account the toe-rock interaction.

The assumptions that were adopted in this derivation include the use of elastic, homogeneous, isotropic materials, the definition of contact from a load applied in the normal direction of the rock surface and frictionless, non-adhesive interface conditions between cutting toe and rock. Justifying those assumptions, it can be said that: inelastic material behaviour was taken into account in the FE analysis stage, the nature of the driving process defines the normal-to the rock- direction as the load application direction and the consideration of friction is out of the scope of this thesis due to the uncertainties in determination that it comes with. The Hertz contact problem is analytically solved, based on the abovementioned assumptions.

The contact pressure resulting from the maximum pile tip stresses for one hammer blow and for the three types of rock, namely granite, limestone and sandstone, is shown in Table 6.2. The modified ANSYS model can be seen in Figure 6.5. The rake angle is 45° and frictional contact is defined in the side face of the toe.

Rock Type	Contact Pressure (MPa)
Granite	16285.03
Limestone	15275.76
Sandstone	14319.84

Table 6.2: Average contact pressure in the toe tip for penetrating granite, limestone and sandstone.

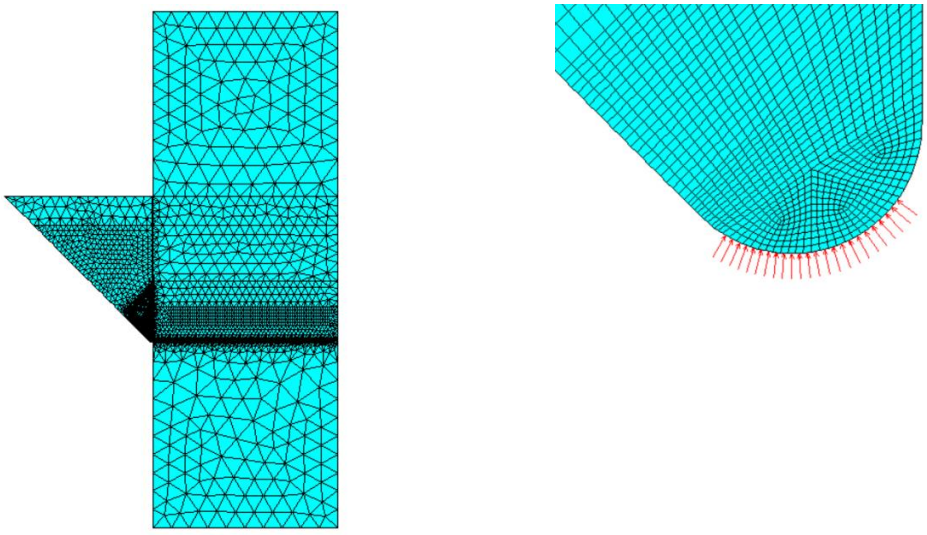

(a) (b)

Figure 6.5: Model for toe wear investigation (a). Application of contact pressure in the toe tip (b).

A static analysis, activating large displacements, is run for the new model with the S2 steel material definition. The part of the toe that has undergone yielding in the end of the analysis is depicted with red colour in Figure 6.6.

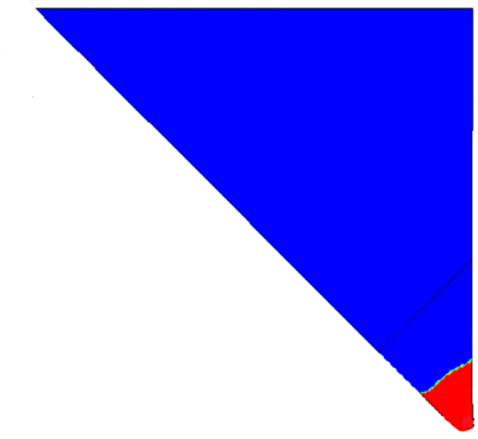

Figure 6.6: Part of the toe that has worn out (in red). (sandstone rock properties)

The Von-mises plastic strain is measured in perpendicular to the rake face sections for different levels of resulting applied contact force in the vertical direction. The latter is equal to the driving force reaching the pile tip. When all the nodes of a section exhibit plastic deformation, the entire cross section of the toe is considered to be worn out, defining a wear flat equal to the width of the section. Then the wear propagation versus the pile tip forces graph is drawn for all types of rock.

It is noted that the stresses are uniform in the sections under investigation, hence according to Saint-Venant's principle the application of the uniform (average) contact pressure does not produce different results than applying a non-uniform contact pressure.

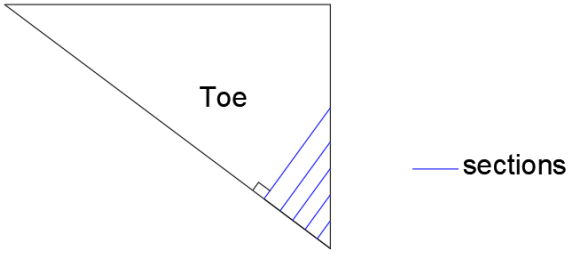

Figure 6.7: Defined sections in the toe for measuring the plastic strain development.

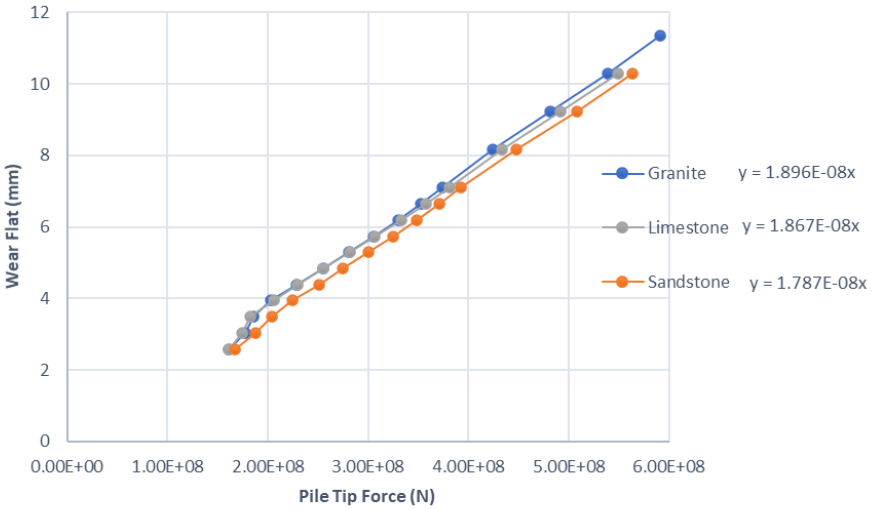

Graph 6.2: Wear propagation in cutting toe made of S2 shock resisting steel for different rock types.

The curves showcase the trend of the interaction with a weaker rock leading to slightly smaller wear propagation in the cutting toe.

The rock cutting theory suggests that increasing the rake angle of a mining tool makes it more susceptible to wear. An investigation was carried out for different cutting angles of ANSYS toe models. The angles that were considered were 45°, 60° and 75°. The same procedure as in the investigation for different rock types was followed, namely imposing a Hertz contact pressure and measuring the plastic strain development in several cross sections.

The results verify the literature findings, showing that an increase in rake angle leads to faster blunting of the cutting toe. Sandstone rock material properties were considered for all models.

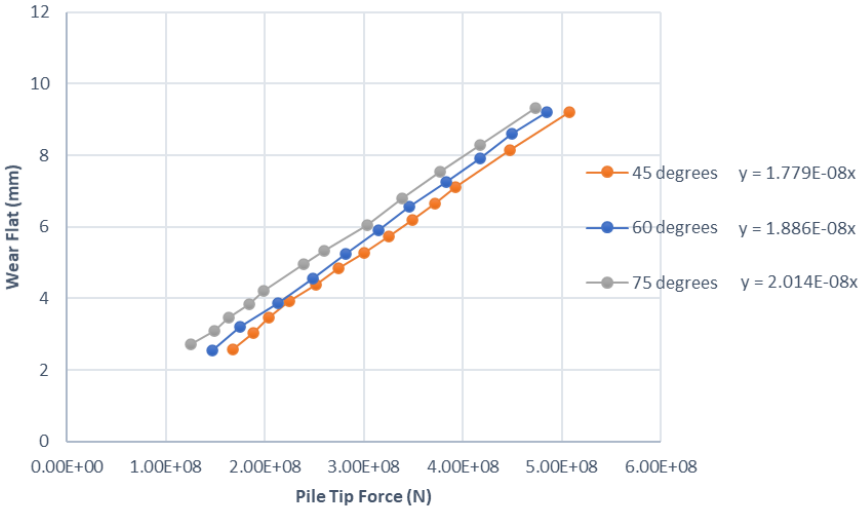

Graph 6.3: Wear propagation in toe made of S2 steel for different cutting angles.

It is noted that dynamic effects are not considered in order to be on the conservative side. If they were to be considered, an increase of approximately 20% in the yield strength of the cutting toe would be possible.

6.3 Cemented Carbide Toe

The unique combination of high strength and good impact resistance of cemented carbide (CC) could potentially make it the material of choice for the drill-drive monopile installation in consideration. Due to its intricate microstructure, the analysis of its failure and wear process is proven to be a complicated matter. Detailed fracture analysis or elaborated explicit non-linear transient dynamic analysis, including strain-hardening, can be conducted for capturing the inelastic behaviour of cemented carbide until failure (Hazell et al., 2010). When finite element analysis is used, the literature review showed that different approaches have been followed. Some researchers utilize the Drucker-Prager failure criterion, taking into account the difference in properties in tension and compression (Agode et al., 2021). By doing that, the carbide phase is assumed to be critical for the ultimate failure of the material. Others represent the inelastic behaviour of CC with an elastic-perfectly plastic material law, choosing the Von Mises criterion to be the one determining if the tool has failed (Nordgren et al., 2014). To be on the conservative side, both approaches are followed in this investigation.

Two compositions were investigated: 91% tungsten carbide and 9% cobalt content (91WC-9Co) with a compressive strength of 4702 MPa and tensile strength of 1862 MPa, and 97% tungsten carbide and 3% cobalt (97WC-3Co) with compressive strength 5778 MPa and tensile strength 1175 MPa (Cardarelli, n.d.). For both compositions, a Young's Modulus of 550 GPa and Poisson's ratio of 0.25 was used.

To begin with, the Hertz contact theory was used to determine the maximum contact pressure in the toe tip for maximum pile tip force, yielding a value of 15631 MPa.

Then, the ANSYS model described in chapter 6.2 was used for a rake angle of 75°. First, the Extended Drucker-Prager (EDP) material law was used as input and the wear flat for different levels of pile tip force was derived.

The second approach included an elastic-perfectly plastic material law definition with the yield strength being equal to the compressive strength. Since the material is neither brittle nor ductile, the most conservative of the Von Mises and Maximum Principal Stress (MPS) criteria was chosen for determining failure. The MPS criterion was proven to be the most critical and the minimum principal stress was checked for the predefined cross-section cuts in the ANSYS model. If the stress is bigger (in value) than the compressive strength in the entire section, then a wear flat of equal width is reported. It is noted that the same failure criterion was also checked for the tensile strength and the maximum principal stress, proving not to be critical as the cutting toe is mainly in compression.

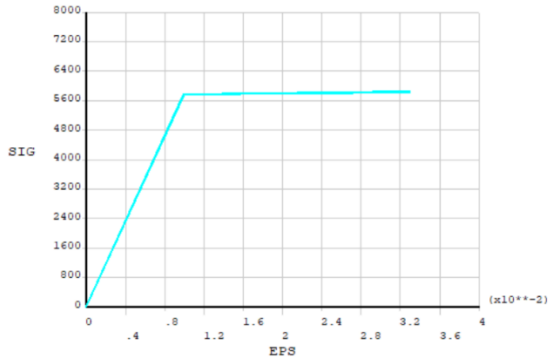

Figure 6.8: Material law for 97WC-3Co cutting toe in ANSYS.

The results of the investigation of wear propagation in cemented carbide can be seen in the following graph, alongside the results for shock resisting steel S2, for a cutting toe of 75° angle.

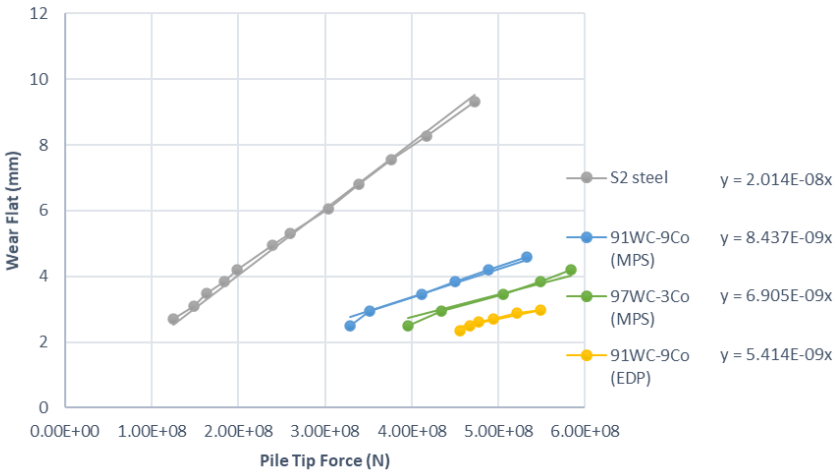

Graph 6.4: Wear Propagation in cutting toe for steel and cemented carbide material properties.

It can be seen that implementing cemented carbide in the cutting toe leads to a stunning 65% reduction in wear propagation.

7 Driveability Analysis

As discussed already, a great challenge of a drill-drive installation of monopiles, using the monopile as casing, is to reach the desired penetration depth. An attempt of a first driveability analysis for this installation method was made as part of this thesis, and the results are given in this chapter.

The Evans rock cutting theory is used for the entire research investigation so far. Considering the theory of minimum work hypothesis, the rock will break in the path of the lower stresses exceeding rock's tensile strength (Miedema, 2019). Mathematically expressed, that means that the angle β can be determined by solving $\frac{\partial F_c}{\partial \beta} = 0$. The full derivation is provided in the appendix. The shear angle β can be derived from the equation:

$$\beta = \frac{1}{2}\left(\frac{\pi}{4} + \frac{\alpha}{2} - \varphi\right) \tag{7.1}$$

where, α is the cutting angle

φ is the friction angle between rock and toe

According to the experiments performed by Evans, the rock will break along a crack of circular arc shape that reaches the free surface. Besides the fact that the exact prediction of the crack path is out of the scope of the thesis, performing such analysis requires detailed numerical simulation of rock considering all aspects relating to its failure or preferably on-site testing. For the driveability analysis in this chapter, the part of the rock material depicted with green in Figure 7.1 is assumed to also get removed by the cutting toe. The quality of this part of rock can be assumed to deteriorate rapidly by being in the vicinity of high failure stresses and therefore would, possibly, not oppose significant resistance in the following rock breaking process. The derivation of the vertical dimension (v_{crack}) of the ejected, by the toe, rock chip can be found in the appendix.

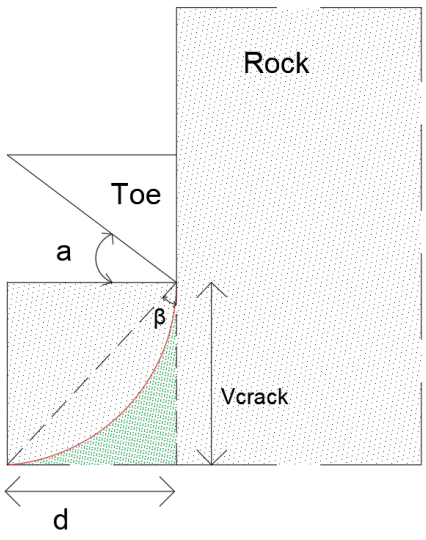

Figure 7.1: Crack propagation according to Evans. Theoretical crack in red. Vertical crack assumed in the thesis.

A constant vertical chip dimension is considered throughout the entire installation.

$$v_{crack} = F_c * \frac{1 - \sin\left(\frac{\pi}{4} - \frac{\alpha}{2} + \varphi\right)}{2\sigma_t w \sin\left(\frac{\pi}{4} - \frac{\alpha}{2} + \varphi\right)} * \frac{1}{\tan\beta} \quad 7.2$$

where, v_{crack} is the vertical dimension of the rock chip

w is the width of the cut

α is the cutting angle

β is the shear breaking angle

The estimation of the pile shaft resistance when driving in rock is proven to be a challenging task due to the uncertainty of the level of degradation that the rock, surrounding the monopile, will experience in the driving process. The value of the characteristic shaft resistance could be determined considering the way that the grains of the rock mass will degrade during the pile driving. Granular and coarse-grained rocks, like granite and sandstone, will disintegrate to a material with a consistency similar to medium-dense sand, hence the effective stress theory for sandy soils could be utilized for estimating the shaft resistance arising from rock (Barrett & Prendergast, 2020).

Adopting the effective stress theory, the formula for determining the pile shaft resistance from rock is:

$$Q_s = K * \sigma_v' * \tan\delta * A_s \quad 7.3$$

where, K is the lateral earth pressure coefficient

σ_v' is the effective overburden pressure

δ is the friction coefficient between the rock and pile wall

A_s is the surface area of the pile shaft

The lateral earth pressure coefficient expresses the pressure that rock imposes on the pile walls in the horizontal direction. It is defined as the ratio of the horizontal effective stress σ_h' and the overburden effective stress σ_v' that the overlying rock layers impose. Depending on the relative behaviour of rock and pile, the coefficient can be characterized as 'active', 'passive' or 'at rest'. The 'active' value is the minimum lateral pressure value and the 'passive' is the maximum one. Active earth pressure is considered when the pile moves away from the rock, allowing the rock mass to 'relax' and deform laterally. On the other hand, passive state occurs when the pile walls push to the rock, forcing the rock mass to deform inwards. The Rankine theory is widely accepted for the estimation of active and passive lateral pressure conditions. A zero lateral strain state describes the at-rest conditions, with the rock mass not moving outwards nor inwards. The value of the 'at rest' coefficient is best to be obtained by field tests, for example dilatometer tests or borehole pressuremeter tests. Due to the uncertainty of the pile's response during the drill-drive operation, a value of 1 is adopted for the lateral earth pressure coefficient, assuming hydrostatic conditions. Additionally, in order to be on the conservative side, a friction coefficient equal to 0.5 is assumed, the maximum value reported between steel and rock.

A driveability analysis was carried out for investigating the penetration depth that is able to be reached for different types of rock, different cutting angles and a toe made of steel or cemented carbide. As already mentioned, a final desired penetration depth of 15m is assumed. The drive-drill installation is considered to experience refusal when the force that is required to further break the rock is bigger than the force that the driving stresses can generate in the pile tip. Additionally, the loss of stability of the monopile results in unsuccessful operation and the driveability analysis is stopped. The analytical dynamic analysis showed that there is stress multiplication in the pile tip with a factor of almost 2, meaning that the critical buckling force can be doubled for getting compared to the force that needs to be generated in the pile tip in order to break the rock. An average critical buckling stress of 250 MPa was used for all cases, as the FEM buckling stress investigation yielded a range of values around that number for all cases considered. A toe wear flat bigger than 80mm, equal to the monopile shell thickness, is used as the third criterion for early termination of the driving process. The reasoning behind the latter is that a cutting toe of bigger width than the shell thickness would give rise to force eccentricities and bending moments, stress concentrations and overall difficulties in joining the monopile and the cutting toe.

An iterative procedure is followed in which for each hammer blow, the required rock cutting force, the pile shaft resistance, the total required force for moving the pile further into the rock and the wear on the cutting toe are determined. If one of the three refusal criteria is met, the driveability stops:

1. The required rock cutting force is bigger than the force that the hydraulic hammer can generate in the pile tip.
2. The required rock cutting force is bigger than the critical monopile buckling force, considering doubling in the tip to account for dynamic stress multiplication.
3. The wear flat in the toe is bigger than 80mm.

The iterative procedure steps are:

1. Consider first hammer blow. Calculate the required cutting force, according to Evans, assuming sharp toe tip. No pile shaft resistance is considered, because the pile is not embedded yet in rock. The required cutting force is evaluated according to the refusal criteria . If none is met, the rock can be cut. The vertical penetration in rock is calculated using the expression 7.2. The developed wear on the cutting is calculated according to the wear flat-pile tip force relationships that were found on chapters 6.2 and 6.3.
2. The second hammer blow is considered. The required rock cutting force (F_c) is calculated considering the toe damage from the previous step, by using the equation 2.142.15. The pile shaft resistance (Q_s) is determined for the embedment depth already achieved (L_i). The total required force for moving the pile downwards (F_{req}) is the sum of the rock cutting force and the shaft resistance. The total force is compared to the pile tip force (F_{tip}), to the pile failure force (refusal criterion 2) and the ability to continue the driving is evaluated. Moreover, the wear flat needs to be smaller than 80mm. If driving can continue, the new embedment length (L_{i+1}) is calculated with the equation $L_i + v_{crack}$. The accumulated wear on the cutting toe is calculated by summing the prior toe damage and the wear flat that was developed in the current hammer blow.
3. The next hammer blow is analysed by following the same procedure as in step 2.
4. The driveability analysis stops when one of the refusal criteria is met.

Rock Properties	Cutting Angle (°)	Toe Material	Rock Cutting Force (N)	Pile Failure Force (N)	Allowable wear (mm)	Maximum Embedment (m)
Granite	45	Steel	6.698E+07	9.953E+08	24.74	0.81
Limestone	45	Steel	7.616E+07	9.953E+08	21.54	0.79
Sandstone	45	Steel	2.010E+07	9.953E+08	80.00	2.75
Sandstone	60	Steel	1.264E+07	9.953E+08	80.00	3.86
Sandstone	75	Steel	7.382E+06	9.953E+08	80.00	5.2
Sandstone 2	75	Steel	4.352E+06	9.953E+08	80.00	8.66
Sandstone 2	75	91WC-9Co	7.801E+06	9.953E+08	80.00	13.4
Sandstone 2	75	97WC-3Co	7.801E+06	9.953E+08	80.00	15

*the rock cutting force is derived for lack of toe wear

* the pile failure force includes dynamic force multiplication

* the allowable wear is calculated from the Bilgin wear formula

Table 7.1: Maximum penetration depth with drill-drive installation in rock using the monopile as casing.

The table of the driveability analysis results for sandstone rock properties and a cutting angle of 45° are provided below. The tables for the rest of the investigated cases can be found in the appendix.

Blow no	Li (mm)	Fc (N)	Qs (N)	Freq (N)	Ftip (N)	Refusal	v (mm)	Li+1 (mm)	Li+1 (m)	w (mm)
0	0.00	0	0.00E+00	0	0.00E+00	0	0.00	0.00	0	0.00
1	0.00	2.01E+07	0.00E+00	2.01E+07	5.84E+08	NO	144.60	144.60	0.14	0.36
2	144.60	2.40E+07	1.77E+03	2.40E+07	5.84E+08	NO	144.60	289.20	0.29	0.79
3	289.20	2.89E+07	7.06E+03	2.89E+07	5.84E+08	NO	144.60	433.80	0.43	1.31
4	433.80	3.47E+07	1.59E+04	3.47E+07	5.84E+08	NO	144.60	578.39	0.58	1.94
5	578.39	4.18E+07	2.82E+04	4.18E+07	5.84E+08	NO	144.60	722.99	0.72	2.69
6	722.99	5.02E+07	4.41E+04	5.02E+07	5.84E+08	NO	144.60	867.59	0.87	3.59
7	867.59	6.04E+07	6.36E+04	6.04E+07	5.84E+08	NO	144.60	1012.19	1.01	4.67
8	1012.19	7.26E+07	8.65E+04	7.27E+07	5.84E+08	NO	144.60	1156.79	1.16	5.98
9	1156.79	8.73E+07	1.13E+05	8.74E+07	5.84E+08	NO	144.60	1301.39	1.30	7.55
10	1301.39	1.05E+08	1.43E+05	1.05E+08	5.84E+08	NO	144.60	1445.99	1.45	9.43
11	1445.99	1.26E+08	1.77E+05	1.26E+08	5.84E+08	NO	144.60	1590.58	1.59	11.70
12	1590.58	1.52E+08	1.77E+05	1.52E+08	5.84E+08	NO	144.60	1735.18	1.74	14.43
13	1735.18	1.82E+08	2.54E+05	1.83E+08	5.84E+08	NO	144.60	1879.78	1.88	17.71
14	1879.78	2.19E+08	2.98E+05	2.20E+08	5.84E+08	NO	144.60	2024.38	2.02	21.65
15	2024.38	2.64E+08	3.46E+05	2.64E+08	5.84E+08	NO	144.60	2168.98	2.17	26.39
16	2168.98	3.17E+08	3.46E+05	3.18E+08	5.84E+08	NO	144.60	2313.58	2.31	32.09
17	2313.58	3.82E+08	4.52E+05	3.82E+08	5.84E+08	NO	144.60	2458.17	2.46	38.95
18	2458.17	4.59E+08	5.10E+05	4.59E+08	5.84E+08	NO	144.60	2602.77	2.60	47.19
19	2602.77	5.52E+08	5.72E+05	5.52E+08	5.84E+08	NO	144.60	2747.37	2.75	57.11
20	2747.37	6.63E+08	6.37E+05	6.64E+08	5.84E+08	YES				

Table 7.2: Driveability analysis results for drill-drive installation in sandstone, cutting angle of 45° and S2 steel toe.

The results of the driveability analysis are given in Graph 7.1. It can be seen that increasing the rake angle results in achieving a greater embedment depth. When using steel as the cutting toe material, a maximum penetration of almost 9m is calculated for the weaker sandstone. Finally, the toe made of 97WC-3Co can withstand the driving forces and successfully complete the installation operation with a desired embedment depth of 15m, when sandstone rock properties are considered. Moreover, the monopile does not experience buckling or excessive deformation until the final hammer blow. The drill-drive installation method is deemed successful under those specific boundaries, namely a 75° cutting angle, a 97WC-3Co cemented carbide toe and penetration in sandstone of 2.6 MPa tensile strength.

Because the most conservative scenario was followed in the wear propagation analysis, it can be postulated that the proposed installation method could be feasible also with a toe of smaller compressive strength.

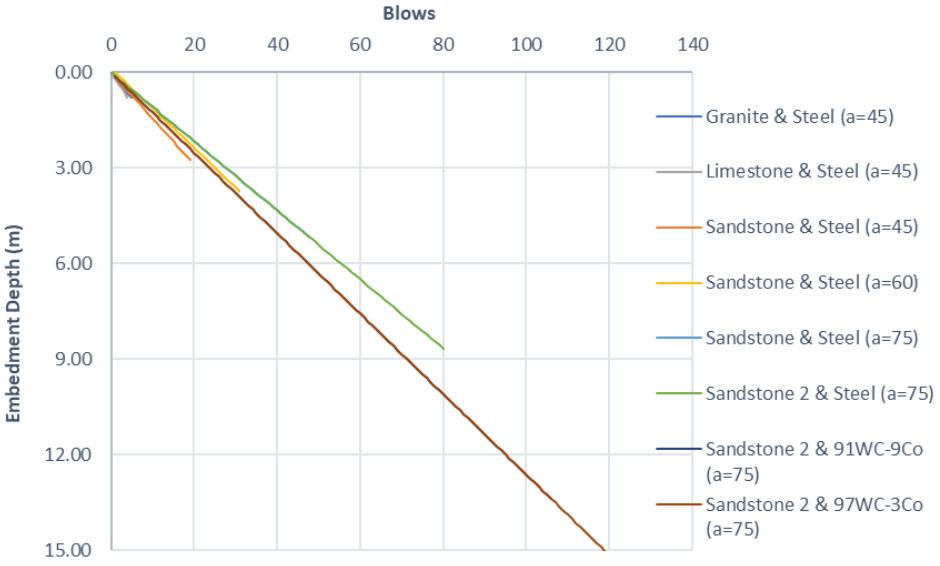

***Graph 7.1*:** Driveability analysis results for drill-drive installation in rock using the monopile as casing.

8 Conclusions

A first attempt was made to investigate the possibility of a successful offshore monopile installation in rock by using the drill-drive method, described in chapter 1.2. The presented research should be regarded as 'testing the waters' of a novel engineering solution that will help the offshore industry and Van Oord to expand its operations in seabed with far from ideal soil conditions. Specifically, the monopile is driven into rock, with a cutting toe, that is attached in its rim, being responsible for breaking the rock and getting the pile to the desired penetration depth. A series of assumptions were adopted during the research that were mandatory to reach some first useful conclusions for evaluating the feasibility of the proposed installation method. These assumptions were mentioned throughout the report of this thesis.

Starting with the results, the ANSYS investigation showed that the cutting angle of the toe plays the most important role in effectively cutting the rock. An average decrease of 5% in the resistance of rock in breaking is estimated for an incremental increase in rake angle of only 5°. Following the findings from literature, a bigger angle would translate to acceleration of the wear propagation that the toe experiences from the interaction with rock. The numerical simulation showed that this increase of the wear damage is not significant. Specifically, an increase of only 10% in the wear rate between rake angles of 45° and 75° is expected. The latter angle value can be considered the maximum that would be used in the design of a toe for the drill-drive installation method and can be concluded to be the optimal selection in terms of cutting efficiency-durability performance. Regarding the tool's material, a cemented carbide toe experiences considerably less wear than a cutting toe made of shock resisting steel.

The modelling approach is deemed as decisive for the investigation of the response of the rock material. Some research constraints had to be applied for reaching a result in agreement with the scope of the thesis. Inside that framework, implementing the Drucker-Prager yielding criterion provides a satisfactory estimation of the response of rock in failure. Different values of dilatancy angle were considered, representing rock material of better quality and greater potential for plastic behaviour after fracture. The simulation results depicted a trend of higher resistance in breaking when the rock is of better quality. Finally, taking into account material failure is more critical for weaker rocks as the results exhibit considerable divergence with the corresponding model with linear elastic properties.

The stability of the monopile during the drill-drive installation method was investigated using non-linear buckling analysis. The resistance of rock in breaking was implemented with a series of non-linear Winkler springs, distributed in the bottom circumference of the pile. The stiffness of those springs was determined from the toe-rock interaction ANSYS models. Uniform pile thickness was assumed along its length, with a diameter over shell thickness ratio of 100. The buckling analysis showed that for a range of typical granite to sandstone rock properties, a critical buckling stress of approximately 250 MPa is to be expected for a steel grade of S355. An imperfection sensitivity analysis was conducted, which highlighted the pile tip as the critical cross-section that will first experience local buckling, irrespective of the initial imperfection shape. Moreover, the effect that the rock borehole has on the stability of the monopile was determined by a series of GMNIA.

The investigation showed that including the rock surrounding in the simulation has only a limited effect in the buckling performance of the pile, due to the initial imperfections shape that result in inefficient lateral restraint of the critical cross-section, as it tries to buckle.

Finally, a driveability analysis was caried out by comparing the pile tip force that the hydraulic hammer can generate and the pile buckling resistance, with the required force for breaking the rock below the monopile foundation. The total bearing resistance, taking into account the skin friction, was calculated and the ability to break the rock for the corresponding toe damage was determined. A penetration depth of 15m is expected to be sufficient for providing the required support during the installation and service life of the wind turbine. The driveability results showed that granite and limestone soil conditions are unfavourable for the successful realisation of the drill-drive installation method, using the monopile as a casing. Moreover, a maximum penetration depth of 9m can be reached when driving in sandstone with an S2 shock resisting steel tool of 75° cutting angle. Under the same angle and by using cemented carbide in the cutting toe's structure, a successful drill-drive operation in sandstone can be achieved. Specifically, for a 97WC-3Co toe, a total wear flat of 57mm was calculated at the end of the installation process. The required driving force for 15m embedment depth did not exceed half of the hammer's capacity and only 30% of the monopile's buckling resistance is utilised, with the pile being in the elastic region throughout the entire driving operation. It is concluded that the drill-drive installation method, by using the monopile as casing, can be successfully used for the offshore installation of monopiles in weak sandstone, when the cutting toe is made of materials with similar mechanical properties as cemented carbide.

9 Future Research Recommendations

The research constraints that were used for reaching the conclusions mentioned above leave ‘room’ for additional future investigations on the drill-drive monopile installation in rock, using the monopile as casing. Recommendations for interesting extensions in the research content are given in this chapter.

The importance of limiting the wear on the cutting toe has already been highlighted throughout the report. To overcome excessive toe damage, cemented carbide was used as the material of choice, yielding successful driveability results. The complex nature of cemented carbide rises questions on the most appropriate method of analysing its failure. In this research, an elastic-perfectly plastic behaviour of the material was defined and the value of maximum principal stresses determined its failure, evaluating this approach as the most conservative. However, a more elaborated failure investigation of cemented carbide is encouraged. Additionally, the extent to which the total volume of the cutting toe consists of this material should be investigated, making allowance for the use of steel in the least affected parts. Most importantly, the cost that cemented carbide would add per monopile foundation, should be estimated. The cutting toe is left in the seabed after the installation is completed, meaning that it will be used only once, and the added cost has to be justified considering the project-specific objectives.

Another aspect that could influence the results is utilising a different rock cutting load introduction. Specifically, vertical rock cutting was considered as a result of the pile driving with a hydraulic hammer. Mining tools that cut the rock by dragging them along its surface have been proven to develop less wear. Hence, introducing rotational motion in the cutting toe could lead to achieving a greater penetration depth even when using steel. This rotation could be generated by an electrical device that would be attached to the cutting toe during the installation, but get removed after its completion. The same electrical device could be used in the installation of several monopiles, keeping the total budget under a reasonable limit. The required speed of cutting should be investigated. Additionally, the effect, on the feasibility of such approach, of introducing vibration or torque in the monopile, during the installation, should be determined. Obviously, this method would require a different research approach and cannot be directly linked to the results presented in this thesis.

The complexity of modelling the crack propagation in rock was pointed out. Following a more elaborated simulation technique, such as fracture analysis, could add valuable new perspectives to the results presented in this thesis. Developing a tool for realistically predicting the, rather unpredictable, behaviour of rock during pile driving will open new possibilities for offshore wind farm development in a hard seabed.

The monopile response was investigated using static analysis. Although prior comparison between static and dynamic analysis results on pile tip buckling evaluated the static approach as sufficient to estimate local failure modes, dynamic simulation should be preferred for the actual design of monopile foundations. If close attention is paid in estimating the damping and rock-structure interaction parameters, and dynamic strain effects are considered, then dynamic analysis is expected to provide more realistic results and is recommended for future studies.

The buckling behaviour of the monopile when encountering rock with non-uniform properties, discontinuities or cracks could yield interesting results and highlight more the effect of the rock borehole on the stability of the pile during driving. Therefore, it is recommended as a future research topic.

Premature termination of the installation method can occur due to fatigue damage. Therefore, the fatigue analysis of the proposed drill-drive solution is strongly encouraged and could be a future research project. The monopile structure is possibly not the critical detail, in fatigue terms. Instead, the monopile-toe connection, the welds along the cutting toe's circumference and the cemented carbide toe could prove to be unable to resist the cycling loading. Connecting the steel and carbide parts with preloaded bolts could be a solution that will effectively keep them clamped, besides the fluctuating stresses in the pile tip, and should be investigated. The fatigue performance of cemented carbide has been described in the available literature, and the degree of suitability of proposed S-N curves for this installation configuration should be evaluated.

Finally, the high uncertainty in the rock's response during a drill-drive monopile installation makes testing in the field mandatory. Accurate determination of the rock mechanical properties, the pile-rock friction, the earth lateral pressure coefficient and the stability of the borehole can only be done by on-site testing and a development of such database is strongly recommended.

Concluding, offshore wind turbine installation in rocky soil is a very promising research field and further studies are an 'one-way street' to exploring new methodologies that will expand the innovative entity of the offshore industry

Bibliography

1. Agode, K. E., Wolff, C., Nouari, M., & Moufki, A. (2021). Microstructure scale modelling of the WC and Co phases plastic behaviour in the WC-Co composite with different cobalt contents and for different temperatures. Comparison of the Drucker-Prager and Mises models. *International Journal of Refractory Metals and Hard Materials*, *99*. https://doi.org/10.1016/j.ijrmhm.2021.105588

2. Alejano, L. R., & Alonso, E. (2005). Considerations of the dilatancy angle in rocks and rock masses. *International Journal of Rock Mechanics and Mining Sciences*, *42*(4), 481–507. https://doi.org/10.1016/j.ijrmms.2005.01.003

3. Alejano, L. R., & Bobet, A. (2012). Drucker-Prager criterion. *Rock Mechanics and Rock Engineering*, *45*(6), 995–999. https://doi.org/10.1007/s00603-012-0278-2

4. Alm, T., & Jacket, A. K. (2004). *Design and Installation of the Valhall Piggyback Structures*. http://onepetro.org/OTCONF/proceedings-pdf/04OTC/All-04OTC/OTC-16294-MS/1854876/otc-16294-ms.pdf/1

5. Barrett, J. W., & Prendergast, L. J. (2020). Empirical Shaft Resistance of Driven Piles Penetrating Weak Rock. *Rock Mechanics and Rock Engineering*, *53*(12), 5531–5543. https://doi.org/10.1007/s00603-020-02228-7

6. Beste, U. (2004). *On the Nature of Cemented Carbide Wear in Rock Drilling*.

7. Bhattacharya, S., Carrington, T. M., & Aldridge, T. R. (2005). Buckling considerations in pile design. *Frontiers in Offshore Geotechnics, ISFOG 2005 - Proceedings of the 1st International Symposium on Frontiers in Offshore Geotechnics*, 815–821. https://doi.org/10.1201/noe0415390637.ch93

8. Bieniawski, Z. T. (1967). MECHANISM OF BRITTLE FRACTURE OF ROCK PART I-THEORY OF THE FRACTURE PROCESS. In *Int. J. Rock Mech. Min. Sci* (Vol. 4). Pergamon Prea Ltd.

9. Bilgin, N. (1977). *Investigations into the mechanical cutting characteristics of some medium and high strength rocks*.

10. Bilgin, N., Copur, H., & Balci, C. (2012). Effect of replacing disc cutters with chisel tools on performance of a TBM in difficult ground conditions. *Tunnelling and Underground Space Technology*, *27*(1), 41–51. https://doi.org/10.1016/j.tust.2011.06.006

11. Bilgin, Nuh, Copur, Hanifi, Balci, & Cemal. (n.d.). *Mechanical Excavation in Mining and Civil Industries*.

12. Bresse, M. (1866). *Cours de Mecanique Appliquee*.

13. Brush, D. O., & Almroth, B. O. (1975). *Buckling of Bars, Plates and Shells*.

14. Cardarelli, F. (n.d.). *Materials Handbook: A Concise Desktop Reference* (2nd Edition).

15. Doğruöz, C. (2010). *EFFECT OF PICK BLUNTING ON CUTTING PERFORMANCE FOR WEAK-MODERATE ROCKS*.

16. Dogruoz, C., & Bolukbasi, N. (2014). Effect of cutting tool blunting on the performances of various mechanical excavators used in low- and medium-strength rocks. *Bulletin of Engineering Geology and the Environment*, *73*(3), 781–789. https://doi.org/10.1007/s10064-013-0551-y

17. Dogruoz, C., Bolukbasi, N., Rostami, J., & Acar, C. (2016). An Experimental Study of Cutting Performances of Worn Picks. *Rock Mechanics and Rock Engineering*, *49*(1), 213–224. https://doi.org/10.1007/s00603-015-0734-x

18. Gaffney, E. S. (1976). *Measurements of Dynamic Friction Between Rock and Steel*. https://www.researchgate.net/publication/235100587

19. Great Britain. Health and Safety Executive., & MSL Engineering. (2001). *A study of pile fatigue during driving and in-service and of pile tip integrity*. HSE Books.

20. Hamdi, S. (n.d.). *Pipe pile driving into rock*. http://hdl.handle.net/2078.1/172501

21. Harvey, P. D. (1982). *Engineering Properties of Steel*.

22. Hazell, P. J., Appleby-Thomas, G. J., Herlaar, K., & Painter, J. (2010). *Materials Science and Engineering A: 527 (29-30)*.

23. Hekinian, R. (n.d.). *Sea Floor Exploration Scientific Adventures Diving into the Abyss*. http://www.springer.com/series/10175

24. Hertz, H. (1882). *Über die Berührung fester elastischer Körper*.

25. Hoek, E., & Brown, E. T. (1997). Practical Estimates of Rock Mass Strength. In *Int. J. Rock Mech. Min. Sci* (Vol. 34, Issue 8).

26. Hurt, K. G., & Macandrew, K. M. (1985). Cutting Efficiency and life of rock-cutting picks. In *Mining Science and Technology* (Vol. 2).

27. Irvine, J., Terente, V., Lee, L. T., & Comrie, R. (2015). Driven pile design in weak rock. *Frontiers in Offshore Geotechnics III - Proceedings of the 3rd International Symposium on Frontiers in Offshore Geotechnics, ISFOG 2015*, 569–574. https://doi.org/10.1201/b18442-73

28. Jafari, M., Gharsallaoui, H., Victor, K. H., & Holeyman, A. (2019). End bearing response of open-ended pipe piles embedded in rock. *International Journal of Rock Mechanics and Mining Sciences*, *119*, 46–57. https://doi.org/10.1016/j.ijrmms.2019.04.008

29. Jorna, M. M. (2018). *Pile tip deformation caused by obstacles*.

30. Liu, W., Qian, X., Li, T., Zhou, Y., & Zhu, X. (2019). Investigation of the tool-rock interaction using Drucker-Prager failure criterion. *Journal of Petroleum Science and Engineering*, *173*, 269–278. https://doi.org/10.1016/j.petrol.2018.09.064

31. Metrikine, A., & Vrouwenvelder, A. C. W. M. (n.d.). Wave Dynamics. In *Dynamics of Structures*.

32. Miedema, S. A. (2019). *The Delft Sand, Clay and Rock Cutting model*.

33. Nahak, S., Dewangan, S., Chattopadhyaya, S., Krolczyk, G., & Hloch, S. (2018). Discussion on importance of tungsten carbide - Cobalt (Wc-Co) cemented carbide and its critical characterization for wear mechanisms based on mining applications. *Archives of Mining Sciences*, *63*(1), 229–246. https://doi.org/10.24425/118897

34. Nishimatsu, Y. (1972). THE MECHANICS OF ROCK CUTTING. In *Int. J. Rock Mech. Min. Sci* (Vol. 9). Pergamon Press.

35. Nordgren, A., Samani, B. Z., & MSaoubic, R. (2014). Experimental study and modelling of plastic deformation of cemented carbide tools in turning. *Procedia CIRP*, *14*, 599–604. https://doi.org/10.1016/j.procir.2014.03.021

36. Ouyang, Y., Yang, Q., Chen, X., & Xu, Y. (2020). An analytical model for rock cutting with a chisel pick of the cutter suction dredger. *Journal of Marine Science and Engineering*, *8*(10), 1–23. https://doi.org/10.3390/jmse8100806

37. Pang, S. S., Goldsmith, W., & Hood, M. (n.d.). *A Force-Indentation Model for Brittle Rocks*.

38. Parola, F. (1970). *Mechanics of impact pile driving*.

39. Peng, S., & Zhang, J. (n.d.). *Engineering Geology for Underground Rocks*.

40. Popov, V., Hess, M., & Willert, E. (2019). *Handbook of Contact Mechanics: Exact solutions of axisymmetric contact problems*.

41. Ramezanzadeh, A. (2010). *A state-of-the-art review of mechanical rock excavation technologies* https://www.researchgate.net/publication/284044715.

42. Randolph, M. F. (2018). *Potential Damage to Steel Pipe Piles During Installation* (Vol. 3).

43. Salehnia, F., Collin, F., & Charlier, R. (2017). On the Variable Dilatancy Angle in Rocks Around Underground Galleries. *Rock Mechanics and Rock Engineering*, *50*(3), 587–601. https://doi.org/10.1007/s00603-016-1126-6

44. SANDVIK. (n.d.). *Cemented Carbide, Sandvik new developments and applications*.

45. Shah, S. (1992). *A modified Hoek-Brown failure criterion for jointed rock masses*.

46. Spagnoli, G., & Weixler, L. (2013). Drilling technologies for offshore foundation engineering. *Proceedings of the International Conference on Offshore Mechanics and Arctic Engineering - OMAE*, *6*. https://doi.org/10.1115/OMAE2013-10305

47. Stevens, R. F., & Westgate, Z. (2019). *Assessing the Pile Driving Risk Due to the Presence of Boulders*. http://onepetro.org/OTCONF/proceedings-pdf/19OTC/3-19OTC/D031S040R003/1137152/otc-29668-ms.pdf/1

48. Stevens, R. S. (1982). *Evaluating Pile Drivability for Hard Clay, Very Dense Sand, and Rock.*

49. Timoshenko, S., & Gere, J. M. (1961). *Theory of Elastic Stability*.

50. Verhoef, P. N. W. (1997). *Wear of rock cutting tools*.

51. Vlasblom, W. J. (n.d.). *LECTURE WB3413 DREDGING PROCESSES: CUTTING OF ROCK*.

52. York, D. L. (n.d.). *Structural Behavior of Driven Piling*.

Appendix

A1: Experimental results on tool wear

Rock	*UCS* (MPa)	*BTS* (MPa)	*Q* (%)	*L* (m)	*WF* (mm)	*FC* (kN)	*F'C* (kN)	*FN* (kN)	*F'N* (kN)	*FN/FC*	*F'N/F'C*
Bunter sandstone	48.2	2.6	82	0.3	0	0.47	1.36	0.31	0.83	0.66	0.61
				10	1.2	0.72	1.78	0.65	1.32	0.90	0.74
				20	1.5	0.9	2.10	0.80	1.63	0.89	0.78
				30	1.7	0.81	2.29	0.96	1.72	1.19	0.75
				50	2.0	0.96	2.46	1.15	2.02	1.20	0.82
				100	2.1	1.25	2.79	1.61	2.52	1.29	0.90
Dunhouse sandstone	54.8	3.1	76	0.3	0.0	0.33	0.76	0.20	0.44	0.61	0.56
				10	1.2	0.55	1.00	0.57	0.97	1.04	0.97
				20	1.3	0.72	1.30	0.77	1.27	1.07	0.98
				30	1.6	0.76	1.32	0.79	1.38	1.04	1.05
				50	1.9	0.95	1.47	1.14	1.62	1.20	1.10
				100	2.0	1.13	1.67	1.38	1.94	1.22	1.16
Mansfield sandstone	69.9	4.3	14	0.3	0.00	0.38	0.88	0.19	0.39	0.50	0.44
				10	0.16	0.51	1.06	0.30	0.59	0.56	0.56
				20	0.18	0.54	1.14	0.34	0.66	0.63	0.58
				30	0.19	0.51	1.15	0.31	0.63	0.61	0.55
				50	0.22	0.53	1.17	0.4	0.67	0.76	0.57
				100	0.23	0.59	1.20	0.43	0.77	0.78	0.64
Weardale limestone	124.8	7.3	0	0.3	0.00	1.30	2.91	0.73	1.37	0.56	0.47
				10	0.07	1.35	3.12	1.06	1.72	0.79	0.55
				20	0.08	1.33	2.88	1.15	1.82	0.86	0.53
				30	0.10	1.24	2.77	1.09	1.75	0.88	0.63
				50	0.10	1.24	2.50	1.12	1.73	0.90	0.69
				100	0.10	1.3	2.70	1.17	1.69	0.90	0.63
Anhidrite	110.7	5.4	0	0.3	0.00	1.07	2.75	0.55	1.18	0.51	0.43
				10	0.04	1.15	2.49	0.75	1.33	0.65	0.53
				30	0.08	1.22	2.99	1.08	1.61	0.89	0.54
				50	0.11	1.15	2.91	1.29	1.83	1.12	0.63
				100	0.16	1.23	2.73	1.60	2.15	1.30	0.78
Granite	180.3	16.1	38	0.3	0.00	2.35	4.96	1.81	2.89	0.77	0.58
				1.5	0.60	2.56	5.78	3.25	4.51	1.27	0.78
				10	1.09	5.16	10.22	6.94	10.11	1.34	0.99
				20	1.55	6.00	10.98	9.55	12.57	1.59	1.14
				30	1.89	6.39	11.92	10.71	14.31	1.68	1.20
				50	2.47	7.72	13.78	13.52	17.45	1.75	1.27
				100	3.5	7.91	14.87	16.2	23.12	2.05	1.55

***Figure*:** Wear flat experiments results on rock cutting tools. (Bilgin et al., 2012)

A2: S2 shock resisting tool properties

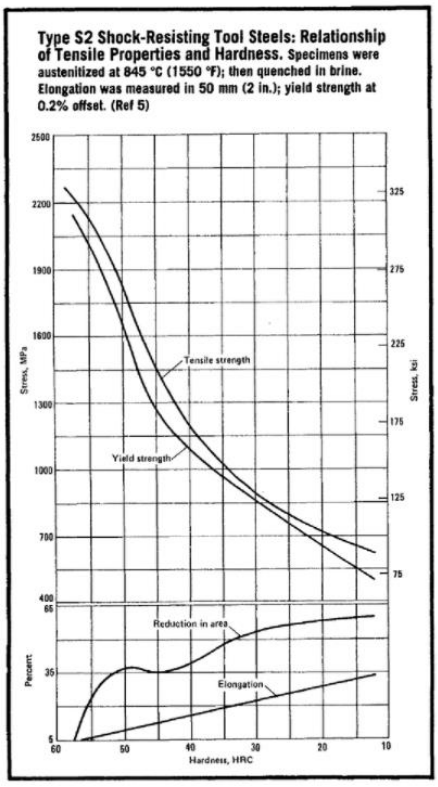

Figure: S2 shock resisting steel yield strength graph. (Harvey, 1982)

A3: Cemented carbide properties

Hardmetal (wt.%)	Density (ρ/kg.m^{-3})	Young's modulus (E/GPa)	Transverse rupture strength (MPa)	Compressive strength (MPa)	Vickers hardness (HV/kgf.mm^{-2})	Thermal conductivity (k/Wm^{-1}K^{-1})	Coefficient of linear thermal expansion (10^{-6} K^{-1})	Electrical resistivity ($\mu\Omega$.cm)
100WC	15,700	707	296–490	2937	1800–2000		5.7–7.2	53
97WC–3Co	15,150	655	979–1175	5778	1600–1700	87.9		
95.5WC–4.5Co	15,050	627	1172–1372	5681	1550–1650	83.7	3.4	
94.5WC–5.5Co	14,800	607	1565–1765	4895	1500–1600	79.5	3.6	20
91WC–9Co	14,600	579	1469–1862	4702	1400–1500	75.3		
89WC–11Co	14,150	565	1565–1958	4502	1300–1400	66.9	3.8	18
87WC–13Co	14,080	545	1662–2,55	4406	1250–1350	58.6		
85WC–15Co	13,800	538	1765–2151	3820	1150–1250		6.0	
80WC–20Co	13,300	490	1958–2544	3330	1050–1150		4.7	
75WC–25Co	13,000	459	1765–2648	3130	900–1000		5.0	
70WC–30Co	12,500				850–950			

Table: Cemented carbide properties. (Cardarelli, n.d.)

A4: DNVGL-RP-C208 True Stress-Strain

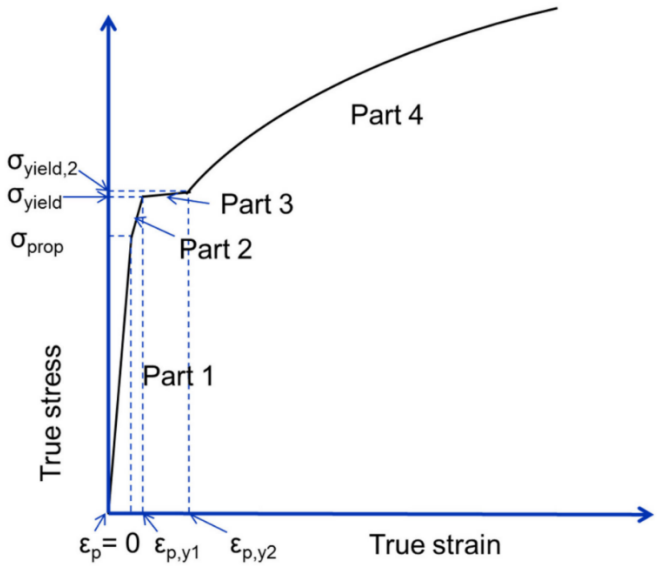

Graph: True stress-strain curve.

	S355			
Thickness [mm]	*t≤ 16*	*16< t ≤ 40*	*40< t ≤ 63*	*63< t ≤ 100*
E [MPa]	210000	210000	210000	210000
σ_{prop} **[MPa]**	320.0	311.0	301.9	284
σ_{yield} **[MPa]**	357.0	346.9	336.9	316.7
σ_{yield2} **[MPa]**	366.1	355.9	345.7	323.8
ε_{p_y1}	0.004	0.004	0.004	0.004
ε_{p_y2}	0.015	0.015	0.015	0.015
K[MPa]	740	740	725	725
n	0.166	0.166	0.166	0.166

Table: Proposed properties for S355 steel

A5: DNVGL-OS-C401 Imperfection tolerances

Detail	*Tolerance*	*Fig.*	*Comments*
Circular cylindrical shells. Local out of roundness. Local out of straightness.	Max. imperfection $\delta = \frac{0.01g}{1 + g/r}$	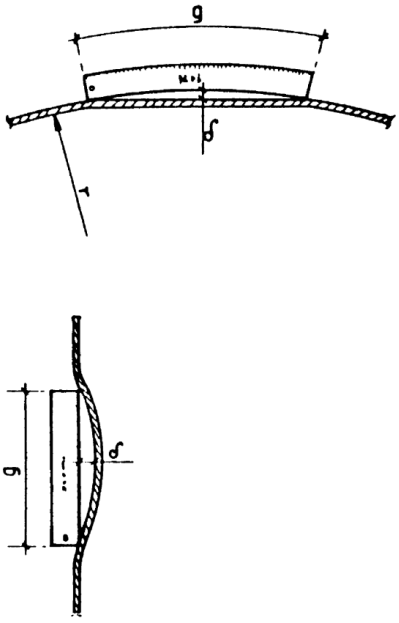	A circular template or straight rod held anywhere on the shell. g = length of template or rod. The length of the circular template shall be the smallest of: $s, 1.15\sqrt{l\sqrt{rt}}$ and $\pi\frac{r}{2}$ s = stiffener spacing (of longitudinal stiffeners) *l* = distance between rings or bulkhead. The length of the straight rod shall be taken equal to the smallest of: *l* and $4\sqrt{rt}$. .
Circular cylindrical shells.	Max. deviation from the nominal radius measured at ring stiffener or bulkhead $\delta = (r_a - r) = 0.005\ r$		r_a = actual distance from the cylinder axis to the shell wall. r = nominal radius of the shell.

Figure: Imperfection tolerances according to DNV code.

B1: Cutting Angle Investigation

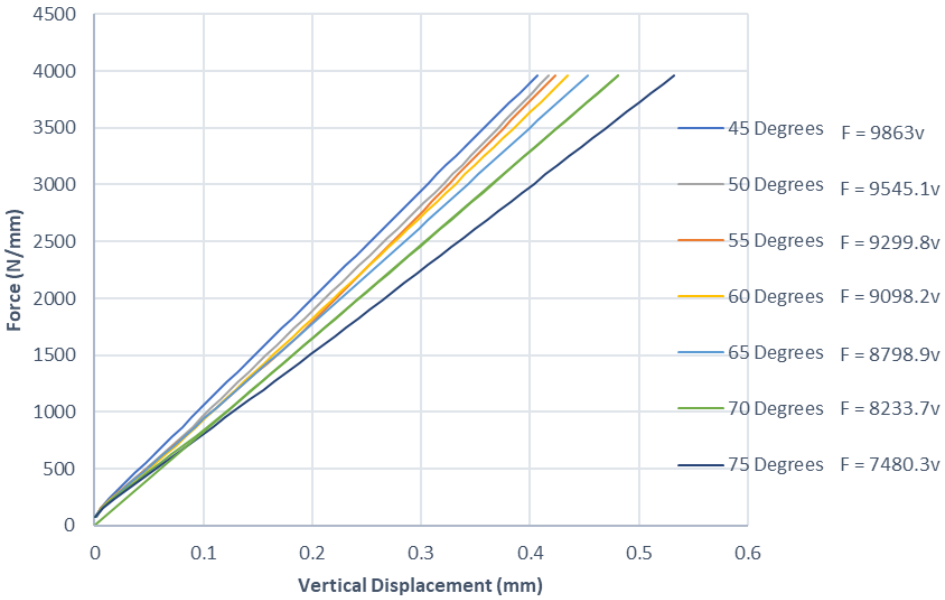

Graph: Force-displacement curves for different cutting angles

B2: Rock Plasticity Investigation

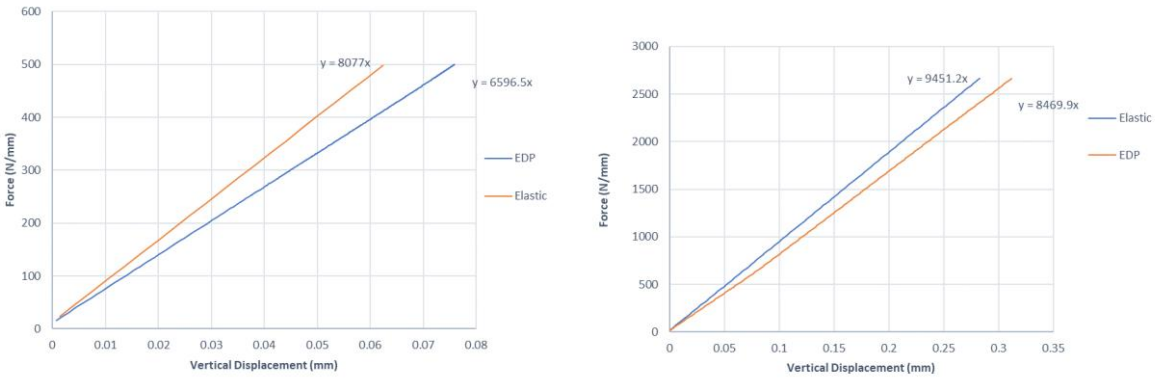

(a) (b)

Graph: Force-displacement curves of cutting operation for elastic and plastic rock properties. Sandstone (a). Granite (b).

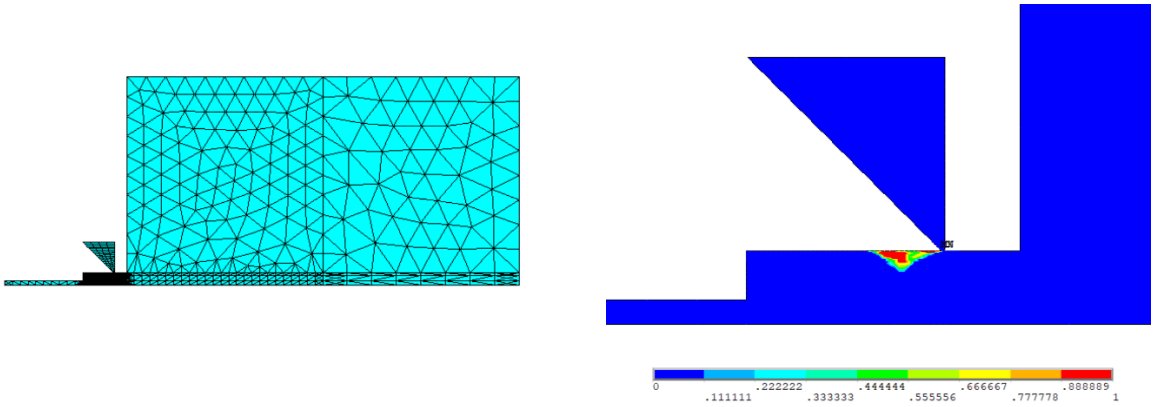

(a) (b)

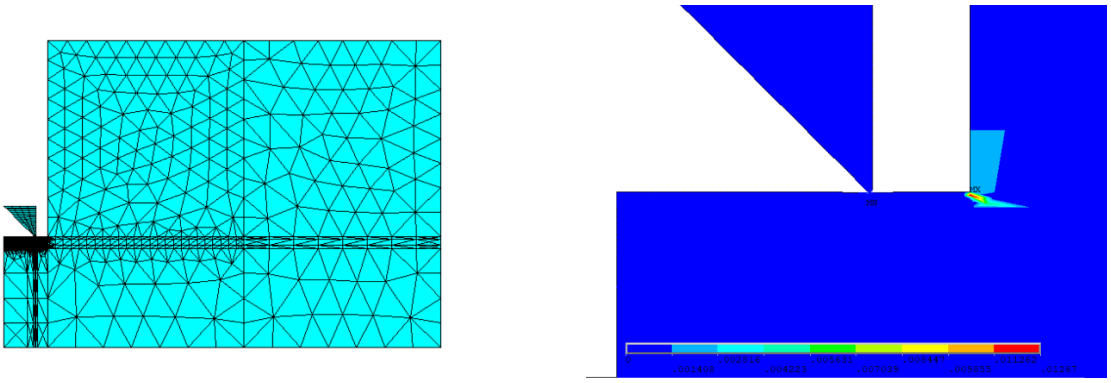

(a) (b)

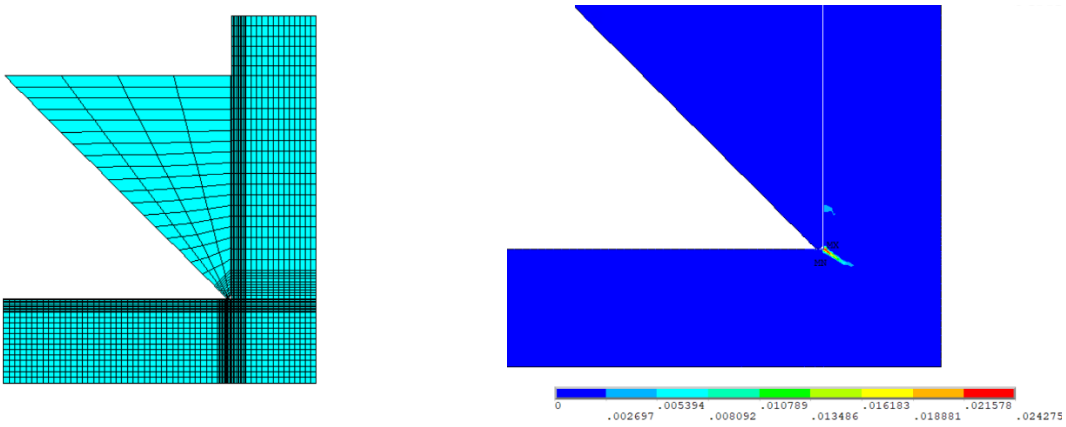

(a) (b)

Figure: The plastic strain propagation depends heavily on the modelled rock mass around the toe, due to changes in the distribution of hydrostatic pressure. ANSYS Model (a). Plastic strain (b).

B3: Driveability Analysis Results

Blow no	Li (mm)	Fc (N)	Qs (N)	Freq (N)	Ftip (N)	Refusal	v (mm)	Li+1 (mm)	Li+1 (m)	w (mm)
0	0.00	0.00E+00	0.00E+00	0.00E+00	0.00E+00	0	0.00	0.00	0.00	0
1	0.00	6.70E+07	0.00E+00	6.70E+07	5.91E+08	NO	161.85	161.85	0.16	1.27
2	161.85	1.14E+08	2.73E+03	1.14E+08	5.91E+08	NO	161.85	323.71	0.32	3.43
3	323.71	1.95E+08	1.09E+04	1.95E+08	5.91E+08	NO	161.85	485.56	0.49	7.14
4	485.56	3.34E+08	2.46E+04	3.34E+08	5.91E+08	NO	161.85	647.41	0.65	13.48
5	647.41	5.73E+08	4.37E+04	5.73E+08	5.91E+08	NO	161.85	809.26	0.81	24.33
6	809.26	9.80E+08	6.82E+04	9.80E+08	5.91E+08	YES				

Table: Driveability analysis results for granite rock properties, 45° cutting angle and S2 steel toe.

Blow no	Li (mm)	Fc (N)	Qs (N)	Freq (N)	Ftip (N)	Refusal	v (mm)	Li+1 (mm)	Li+1 (m)	w (mm)
0	0.00	0.00E+00	0.00E+00	0.00E+00	0.00E+00	0	0.00	0.00	0.00	0.00
1	0.00	1.26E+07	0.00E+00	1.26E+07	5.81E+08	NO	124.59	124.59	0.12	0.24
2	124.59	1.42E+07	1.31E+03	1.42E+07	5.81E+08	NO	124.59	249.19	0.25	0.50
3	249.19	1.61E+07	5.24E+03	1.61E+07	5.81E+08	NO	124.59	373.78	0.37	0.80
4	373.78	1.82E+07	1.18E+04	1.82E+07	5.81E+08	NO	124.59	498.38	0.50	1.14
5	498.38	2.06E+07	2.10E+04	2.07E+07	5.81E+08	NO	124.59	622.97	0.62	1.53
6	622.97	2.34E+07	3.28E+04	2.34E+07	5.81E+08	NO	124.59	747.57	0.75	1.96
7	747.57	2.65E+07	4.72E+04	2.65E+07	5.81E+08	NO	124.59	872.16	0.87	2.46
8	872.16	3.00E+07	6.42E+04	3.00E+07	5.81E+08	NO	124.59	996.76	1.00	3.02
9	996.76	3.39E+07	8.39E+04	3.40E+07	5.81E+08	NO	124.59	1121.35	1.12	3.65
10	1121.35	3.84E+07	1.06E+05	3.85E+07	5.81E+08	NO	124.59	1245.95	1.25	4.37
11	1245.95	4.35E+07	1.31E+05	4.36E+07	5.81E+08	NO	124.59	1370.54	1.37	5.18
12	1370.54	4.93E+07	1.59E+05	4.94E+07	5.81E+08	NO	124.59	1495.13	1.50	6.10
13	1495.13	5.58E+07	1.89E+05	5.60E+07	5.81E+08	NO	124.59	1619.73	1.62	7.15
14	1619.73	6.32E+07	2.22E+05	6.34E+07	5.81E+08	NO	124.59	1744.32	1.74	8.33
15	1744.32	7.15E+07	2.57E+05	7.18E+07	5.81E+08	NO	124.59	1868.92	1.87	9.66
16	1868.92	8.10E+07	2.95E+05	8.13E+07	5.81E+08	NO	124.59	1993.51	1.99	11.17
17	1993.51	9.17E+07	3.36E+05	9.21E+07	5.81E+08	NO	124.59	2118.11	2.12	12.89
18	2118.11	1.04E+08	3.79E+05	1.04E+08	5.81E+08	NO	124.59	2242.70	2.24	14.83
19	2242.70	1.18E+08	4.25E+05	1.18E+08	5.81E+08	NO	124.59	2367.30	2.37	17.02
20	2367.30	1.33E+08	4.73E+05	1.34E+08	5.81E+08	NO	124.59	2491.89	2.49	19.51
21	2491.89	1.51E+08	5.24E+05	1.51E+08	5.81E+08	NO	124.59	2616.48	2.62	22.33
22	2616.48	1.71E+08	5.78E+05	1.71E+08	5.81E+08	NO	124.59	2741.08	2.74	25.52
23	2741.08	1.93E+08	6.34E+05	1.94E+08	5.81E+08	NO	124.59	2865.67	2.87	29.13
24	2865.67	2.19E+08	6.93E+05	2.20E+08	5.81E+08	NO	124.59	2990.27	2.99	33.22
25	2990.27	2.48E+08	7.55E+05	2.49E+08	5.81E+08	NO	124.59	3114.86	3.11	37.85
26	3114.86	2.81E+08	8.19E+05	2.82E+08	5.81E+08	NO	124.59	3239.46	3.24	43.09
27	3239.46	3.18E+08	8.86E+05	3.19E+08	5.81E+08	NO	124.59	3364.05	3.36	49.03
28	3364.05	3.60E+08	8.86E+05	3.61E+08	5.81E+08	NO	124.59	3488.65	3.49	55.75
29	3488.65	4.08E+08	1.03E+06	4.09E+08	5.81E+08	NO	124.59	3613.24	3.61	63.37
30	3613.24	4.62E+08	1.10E+06	4.63E+08	5.81E+08	NO	124.59	3737.84	3.74	71.99
31	3737.84	5.23E+08	1.18E+06	5.24E+08	5.81E+08	NO	124.59	3862.43	3.86	81.75
32	3862.43	5.92E+08	1.26E+06	5.93E+08	5.81E+08	YES				

Table: Driveability analysis results for sandstone rock properties, 60° cutting angle and S2 steel toe.

Blow no	Li (mm)	Fc (N)	Qs (N)	Freq (N)	Ftip (N)	Refusal	v (mm)	Li+1 (mm)	Li+1 (m)	w (mm)
0	0.00	0.00E+00	0.00E+00	0.00E+00	0.00E+00	0	0.00	0.00	0.00	0.00
1	0.00	7.62E+07	0.00E+00	7.62E+07	5.88E+08	NO	197.33	197.33	0.20	1.42
2	197.33	1.36E+08	3.98E+03	1.36E+08	5.88E+08	NO	197.33	394.67	0.39	3.97
3	394.67	2.45E+08	1.59E+04	2.45E+08	5.88E+08	NO	197.33	592.00	0.59	8.54
4	592.00	4.40E+08	3.59E+04	4.40E+08	5.88E+08	NO	197.33	789.34	0.79	16.75
5	789.34	7.91E+08	6.38E+04	7.91E+08	5.88E+08	YES				

Table: Driveability analysis results for limestone rock properties, 45° cutting angle and S2 steel toe.

Blow no	Li (mm)	Fc (N)	Qs (N)	Freq (N)	Ftip (N)	Refusal	v (mm)	Li+1 (mm)	Li+1 (m)	w (mm)
0.00	0.00	0.00E+00	0.00E+00	0.00E+00	0.00E+00	0	0.00	0.00	0.00	0.00
1.00	0.00	7.38E+06	0.00E+00	7.38E+06	5.73E+08	NO	108.30	108.30	0.11	0.15
2.00	108.30	7.94E+06	9.90E+02	7.94E+06	5.73E+08	NO	108.30	216.59	0.22	0.31
3.00	216.59	8.60E+06	3.96E+03	8.60E+06	5.73E+08	NO	108.30	324.89	0.32	0.48
4.00	324.89	9.32E+06	8.91E+03	9.33E+06	5.73E+08	NO	108.30	433.18	0.43	0.67
5.00	433.18	1.01E+07	1.58E+04	1.01E+07	5.73E+08	NO	108.30	541.48	0.54	0.87
6.00	541.48	1.09E+07	2.48E+04	1.10E+07	5.73E+08	NO	108.30	649.78	0.65	1.09
7.00	649.78	1.18E+07	3.57E+04	1.19E+07	5.73E+08	NO	108.30	758.07	0.76	1.33
8.00	758.07	1.28E+07	4.85E+04	1.29E+07	5.73E+08	NO	108.30	866.37	0.87	1.59
9.00	866.37	1.39E+07	6.34E+04	1.40E+07	5.73E+08	NO	108.30	974.67	0.97	1.87
10.00	974.67	1.51E+07	8.02E+04	1.51E+07	5.73E+08	NO	108.30	1082.96	1.08	2.17
11.00	1082.96	1.63E+07	9.90E+04	1.64E+07	5.73E+08	NO	108.30	1191.26	1.19	2.50
12.00	1191.26	1.77E+07	1.20E+05	1.78E+07	5.73E+08	NO	108.30	1299.55	1.30	2.86
13.00	1299.55	1.91E+07	1.43E+05	1.93E+07	5.73E+08	NO	108.30	1407.85	1.41	3.24
14.00	1407.85	2.07E+07	1.67E+05	2.09E+07	5.73E+08	NO	108.30	1516.15	1.52	3.66
15.00	1516.15	2.25E+07	1.94E+05	2.27E+07	5.73E+08	NO	108.30	1624.44	1.62	4.11
16.00	1624.44	2.43E+07	2.23E+05	2.46E+07	5.73E+08	NO	108.30	1732.74	1.73	4.60
17.00	1732.74	2.64E+07	2.54E+05	2.66E+07	5.73E+08	NO	108.30	1841.04	1.84	5.14
18.00	1841.04	2.86E+07	2.86E+05	2.89E+07	5.73E+08	NO	108.30	1949.33	1.95	5.71
19.00	1949.33	3.10E+07	3.21E+05	3.13E+07	5.73E+08	NO	108.30	2057.63	2.06	6.33
20.00	2057.63	3.35E+07	3.58E+05	3.39E+07	5.73E+08	NO	108.30	2165.92	2.17	7.01
21.00	2165.92	3.63E+07	3.96E+05	3.67E+07	5.73E+08	NO	108.30	2274.22	2.27	7.74
22.00	2274.22	3.94E+07	4.37E+05	3.98E+07	5.73E+08	NO	108.30	2382.52	2.38	8.53
23.00	2382.52	4.26E+07	4.79E+05	4.31E+07	5.73E+08	NO	108.30	2490.81	2.49	9.39
24.00	2490.81	4.62E+07	5.24E+05	4.67E+07	5.73E+08	NO	108.30	2599.11	2.60	10.32
25.00	2599.11	5.00E+07	5.70E+05	5.06E+07	5.73E+08	NO	108.30	2707.41	2.71	11.33
26.00	2707.41	5.42E+07	6.19E+05	5.48E+07	5.73E+08	NO	108.30	2815.70	2.82	12.42
27.00	2815.70	5.87E+07	6.69E+05	5.94E+07	5.73E+08	NO	108.30	2924.00	2.92	13.60
28.00	2924.00	6.36E+07	7.22E+05	6.43E+07	5.73E+08	NO	108.30	3032.29	3.03	14.89
29.00	3032.29	6.89E+07	7.76E+05	6.97E+07	5.73E+08	NO	108.30	3140.59	3.14	16.27
30.00	3140.59	7.47E+07	8.33E+05	7.55E+07	5.73E+08	NO	108.30	3248.89	3.25	17.78
31.00	3248.89	8.09E+07	8.91E+05	8.18E+07	5.73E+08	NO	108.30	3357.18	3.36	19.41
32.00	3357.18	8.76E+07	9.52E+05	8.86E+07	5.73E+08	NO	108.30	3465.48	3.47	21.17
33.00	3465.48	9.49E+07	1.01E+06	9.59E+07	5.73E+08	NO	108.30	3573.78	3.57	23.08
34.00	3573.78	1.03E+08	1.08E+06	1.04E+08	5.73E+08	NO	108.30	3682.07	3.68	25.15
35.00	3682.07	1.11E+08	1.14E+06	1.13E+08	5.73E+08	NO	108.30	3790.37	3.79	27.40
36.00	3790.37	1.21E+08	1.21E+06	1.22E+08	5.73E+08	NO	108.30	3898.66	3.90	29.83
37.00	3898.66	1.31E+08	1.28E+06	1.32E+08	5.73E+08	NO	108.30	4006.96	4.01	32.46
38.00	4006.96	1.42E+08	1.36E+06	1.43E+08	5.73E+08	NO	108.30	4115.26	4.12	35.31
39.00	4115.26	1.53E+08	1.43E+06	1.55E+08	5.73E+08	NO	108.30	4223.55	4.22	38.40
40.00	4223.55	1.66E+08	1.51E+06	1.68E+08	5.73E+08	NO	108.30	4331.85	4.33	41.75
41.00	4331.85	1.80E+08	1.58E+06	1.82E+08	5.73E+08	NO	108.30	4440.14	4.44	45.38
42.00	4440.14	1.95E+08	1.66E+06	1.97E+08	5.73E+08	NO	108.30	4548.44	4.55	49.31
43.00	4548.44	2.11E+08	1.75E+06	2.13E+08	5.73E+08	NO	108.30	4656.74	4.66	53.56
44.00	4656.74	2.29E+08	1.83E+06	2.31E+08	5.73E+08	NO	108.30	4765.03	4.77	58.17
45.00	4765.03	2.48E+08	1.92E+06	2.50E+08	5.73E+08	NO	108.30	4873.33	4.87	63.17
46.00	4873.33	2.69E+08	1.92E+06	2.71E+08	5.73E+08	NO	108.30	4981.63	4.98	68.58
47.00	4981.63	2.91E+08	2.10E+06	2.93E+08	5.73E+08	NO	108.30	5089.92	5.09	74.44
48.00	5089.92	3.15E+08	2.19E+06	3.18E+08	5.73E+08	YES	108.30	5198.22	5.20	80.79

Table: Driveability analysis results for sandstone rock properties, 75° cutting angle and S2 steel toe.

Blow no	Li (mm)	Fc (N)	Qs (N)	Freq (N)	Ftip (N)	Refusal	v (mm)	Li+1 (mm)	Li+1 (m)	w (mm)
0	0.00	0.00E+00	0.00E+00	0.00E+00	0.00E+00	0	0.00	0.00	0.00	0.00
1	0.00	4.35E+06	0.00E+00	4.35E+06	5.73E+08	NO	108.30	108.30	0.11	0.09
2	108.30	4.53E+06	9.90E+02	4.53E+06	5.73E+08	NO	108.30	216.59	0.22	0.18
3	216.59	4.75E+06	3.96E+03	4.76E+06	5.73E+08	NO	108.30	324.89	0.32	0.27
4	324.89	4.99E+06	8.91E+03	5.00E+06	5.73E+08	NO	108.30	433.18	0.43	0.38
5	433.18	5.23E+06	1.58E+04	5.25E+06	5.73E+08	NO	108.30	541.48	0.54	0.48
6	541.48	5.49E+06	2.48E+04	5.52E+06	5.73E+08	NO	108.30	649.78	0.65	0.59
7	649.78	5.76E+06	3.57E+04	5.80E+06	5.73E+08	NO	108.30	758.07	0.76	0.71
8	758.07	6.04E+06	4.85E+04	6.09E+06	5.73E+08	NO	108.30	866.37	0.87	0.83
9	866.37	6.34E+06	6.34E+04	6.40E+06	5.73E+08	NO	108.30	974.67	0.97	0.96
10	974.67	6.65E+06	8.02E+04	6.73E+06	5.73E+08	NO	108.30	1082.96	1.08	1.09
11	1082.96	6.98E+06	9.90E+04	7.08E+06	5.73E+08	NO	108.30	1191.26	1.19	1.23
12	1191.26	7.32E+06	1.20E+05	7.44E+06	5.73E+08	NO	108.30	1299.55	1.30	1.38
13	1299.55	7.68E+06	1.43E+05	7.82E+06	5.73E+08	NO	108.30	1407.85	1.41	1.53
14	1407.85	8.06E+06	1.67E+05	8.23E+06	5.73E+08	NO	108.30	1516.15	1.52	1.70
15	1516.15	8.45E+06	1.94E+05	8.65E+06	5.73E+08	NO	108.30	1624.44	1.62	1.87
16	1624.44	8.87E+06	2.23E+05	9.09E+06	5.73E+08	NO	108.30	1732.74	1.73	2.04
17	1732.74	9.30E+06	2.54E+05	9.56E+06	5.73E+08	NO	108.30	1841.04	1.84	2.23
18	1841.04	9.76E+06	2.86E+05	1.00E+07	5.73E+08	NO	108.30	1949.33	1.95	2.43
19	1949.33	1.02E+07	3.21E+05	1.06E+07	5.73E+08	NO	108.30	2057.63	2.06	2.63
20	2057.63	1.07E+07	3.58E+05	1.11E+07	5.73E+08	NO	108.30	2165.92	2.17	2.85
21	2165.92	1.13E+07	3.96E+05	1.17E+07	5.73E+08	NO	108.30	2274.22	2.27	3.08
22	2274.22	1.18E+07	4.37E+05	1.23E+07	5.73E+08	NO	108.30	2382.52	2.38	3.32
23	2382.52	1.24E+07	4.79E+05	1.29E+07	5.73E+08	NO	108.30	2490.81	2.49	3.57
24	2490.81	1.30E+07	5.24E+05	1.35E+07	5.73E+08	NO	108.30	2599.11	2.60	3.83
25	2599.11	1.37E+07	5.70E+05	1.42E+07	5.73E+08	NO	108.30	2707.41	2.71	4.10
26	2707.41	1.43E+07	6.19E+05	1.49E+07	5.73E+08	NO	108.30	2815.70	2.82	4.39
27	2815.70	1.50E+07	6.69E+05	1.57E+07	5.73E+08	NO	108.30	2924.00	2.92	4.69
28	2924.00	1.58E+07	7.22E+05	1.65E+07	5.73E+08	NO	108.30	3032.29	3.03	5.01
29	3032.29	1.65E+07	7.76E+05	1.73E+07	5.73E+08	NO	108.30	3140.59	3.14	5.35
30	3140.59	1.74E+07	8.33E+05	1.82E+07	5.73E+08	NO	108.30	3248.89	3.25	5.69
31	3248.89	1.82E+07	8.91E+05	1.91E+07	5.73E+08	NO	108.30	3357.18	3.36	6.06
32	3357.18	1.91E+07	9.52E+05	2.01E+07	5.73E+08	NO	108.30	3465.48	3.47	6.45
33	3465.48	2.00E+07	1.01E+06	2.11E+07	5.73E+08	NO	108.30	3573.78	3.57	6.85
34	3573.78	2.10E+07	1.08E+06	2.21E+07	5.73E+08	NO	108.30	3682.07	3.68	7.27
35	3682.07	2.21E+07	1.14E+06	2.32E+07	5.73E+08	NO	108.30	3790.37	3.79	7.72
36	3790.37	2.31E+07	1.21E+06	2.44E+07	5.73E+08	NO	108.30	3898.66	3.90	8.18
37	3898.66	2.43E+07	1.28E+06	2.56E+07	5.73E+08	NO	108.30	4006.96	4.01	8.67
38	4006.96	2.55E+07	1.36E+06	2.68E+07	5.73E+08	NO	108.30	4115.26	4.12	9.19
39	4115.26	2.67E+07	1.43E+06	2.82E+07	5.73E+08	NO	108.30	4223.55	4.22	9.72
40	4223.55	2.80E+07	1.51E+06	2.95E+07	5.73E+08	NO	108.30	4331.85	4.33	10.29
41	4331.85	2.94E+07	1.58E+06	3.10E+07	5.73E+08	NO	108.30	4440.14	4.44	10.88
42	4440.14	3.09E+07	1.66E+06	3.25E+07	5.73E+08	NO	108.30	4548.44	4.55	11.50
43	4548.44	3.24E+07	1.75E+06	3.41E+07	5.73E+08	NO	108.30	4656.74	4.66	12.16
44	4656.74	3.40E+07	1.83E+06	3.58E+07	5.73E+08	NO	108.30	4765.03	4.77	12.84
45	4765.03	3.56E+07	1.92E+06	3.76E+07	5.73E+08	NO	108.30	4873.33	4.87	13.56
46	4873.33	3.74E+07	1.92E+06	3.93E+07	5.73E+08	NO	108.30	4981.63	4.98	14.31
47	4981.63	3.92E+07	2.10E+06	4.13E+07	5.73E+08	NO	108.30	5089.92	5.09	15.10
48	5089.92	4.12E+07	2.19E+06	4.33E+07	5.73E+08	NO	108.30	5198.22	5.20	15.93
49	5198.22	4.32E+07	2.28E+06	4.55E+07	5.73E+08	NO	108.30	5306.51	5.31	16.80
50	5306.51	4.53E+07	2.38E+06	4.77E+07	5.73E+08	NO	108.30	5414.81	5.41	17.71
51	5414.81	4.75E+07	2.48E+06	5.00E+07	5.73E+08	NO	108.30	5523.11	5.52	18.67
52	5523.11	4.99E+07	2.58E+06	5.24E+07	5.73E+08	NO	108.30	5631.40	5.63	19.67
53	5631.40	5.23E+07	2.68E+06	5.50E+07	5.73E+08	NO	108.30	5739.70	5.74	20.73
54	5739.70	5.49E+07	2.78E+06	5.77E+07	5.73E+08	NO	108.30	5848.00	5.85	21.83
55	5848.00	5.76E+07	2.89E+06	6.05E+07	5.73E+08	NO	108.30	5956.29	5.96	22.99
56	5956.29	6.04E+07	3.00E+06	6.34E+07	5.73E+08	NO	108.30	6064.59	6.06	24.21
57	6064.59	6.34E+07	3.11E+06	6.65E+07	5.73E+08	NO	108.30	6172.88	6.17	25.48
58	6172.88	6.65E+07	3.22E+06	6.97E+07	5.73E+08	NO	108.30	6281.18	6.28	26.82
59	6281.18	6.97E+07	3.33E+06	7.31E+07	5.73E+08	NO	108.30	6389.48	6.39	28.23
60	6389.48	7.32E+07	3.45E+06	7.66E+07	5.73E+08	NO	108.30	6497.77	6.50	29.70
61	6497.77	7.68E+07	3.57E+06	8.03E+07	5.73E+08	NO	108.30	6606.07	6.61	31.25
62	6606.07	8.05E+07	3.69E+06	8.42E+07	5.73E+08	NO	108.30	6714.37	6.71	32.87
63	6714.37	8.45E+07	3.81E+06	8.83E+07	5.73E+08	NO	108.30	6822.66	6.82	34.57
64	6822.66	8.86E+07	3.93E+06	9.26E+07	5.73E+08	NO	108.30	6930.96	6.93	36.35
65	6930.96	9.30E+07	4.06E+06	9.71E+07	5.73E+08	NO	108.30	7039.25	7.04	38.23
66	7039.25	9.76E+07	4.18E+06	1.02E+08	5.73E+08	NO	108.30	7147.55	7.15	40.19
67	7147.55	1.02E+08	4.31E+06	1.07E+08	5.73E+08	NO	108.30	7255.85	7.26	42.25
68	7255.85	1.07E+08	4.45E+06	1.12E+08	5.73E+08	NO	108.30	7364.14	7.36	44.42
69	7364.14	1.13E+08	4.58E+06	1.17E+08	5.73E+08	NO	108.30	7472.44	7.47	46.69
70	7472.44	1.18E+08	4.72E+06	1.23E+08	5.73E+08	NO	108.30	7580.74	7.58	49.07
71	7580.74	1.24E+08	4.85E+06	1.29E+08	5.73E+08	NO	108.30	7689.03	7.69	51.56
72	7689.03	1.30E+08	4.99E+06	1.35E+08	5.73E+08	NO	108.30	7797.33	7.80	54.18
73	7797.33	1.36E+08	5.13E+06	1.42E+08	5.73E+08	NO	108.30	7905.62	7.91	56.93
74	7905.62	1.43E+08	5.28E+06	1.48E+08	5.73E+08	NO	108.30	8013.92	8.01	59.82
75	8013.92	1.50E+08	5.42E+06	1.56E+08	5.73E+08	NO	108.30	8122.22	8.12	62.84
76	8122.22	1.58E+08	5.57E+06	1.63E+08	5.73E+08	NO	108.30	8230.51	8.23	66.02
77	8230.51	1.65E+08	5.72E+06	1.71E+08	5.73E+08	NO	108.30	8338.81	8.34	69.35
78	8338.81	1.73E+08	5.87E+06	1.79E+08	5.73E+08	NO	108.30	8447.10	8.45	72.84
79	8447.10	1.82E+08	6.03E+06	1.88E+08	5.73E+08	NO	108.30	8555.40	8.56	76.51
80	8555.40	1.91E+08	6.18E+06	1.97E+08	5.73E+08	YES	108.30	8663.70	8.66	80.35

Table: Driveability analysis results for sandstone 2 rock properties, 75° cutting angle and S2 steel toe.

Blow no	Li (mm)	Fc (N)	Qs (N)	Freq (N)	Ftip (N)	Refusal	v (mm)	Li+1 (mm)	Li+1 (m)	w (mm)
0	0	0	0	0	0	0	0	0		0.00
1	0	7800945.1	0	7800945.1	5.81E+08	NO	126.29511	126.29511	0.12629511	0.07
2	126.29511	8027876.1	1346.9221	8029223	5.81E+08	NO	126.29511	252.59021	0.25259021	0.13
3	252.59021	8324026	5387.6885	8329413.7	5.81E+08	NO	126.29511	378.88532	0.37888532	0.20
4	378.88532	8631100.9	12122.299	8643223.2	5.81E+08	NO	126.29511	505.18042	0.50518042	0.28
5	505.18042	8949503.8	21550.754	8971054.6	5.81E+08	NO	126.29511	631.47553	0.63147553	0.35
6	631.47553	9279652.7	33673.053	9313325.8	5.81E+08	NO	126.29511	757.77063	0.75777063	0.43
7	757.77063	9621980.9	48489.196	9670470.1	5.81E+08	NO	126.29511	884.06574	0.88406574	0.51
8	884.06574	9976937.6	65999.184	10042937	5.81E+08	NO	126.29511	1010.3608	1.01036084	0.60
9	1010.3608	10344989	86203.015	10431192	5.81E+08	NO	126.29511	1136.6559	1.13665595	0.68
10	1136.6559	10726617	109100.69	10835718	5.81E+08	NO	126.29511	1262.9511	1.26295106	0.77
11	1262.9511	11122324	134692.21	11257016	5.81E+08	NO	126.29511	1389.2462	1.38924616	0.87
12	1389.2462	11532629	162977.58	11695606	5.81E+08	NO	126.29511	1515.5413	1.51554127	0.96
13	1515.5413	11958070	193956.78	12152027	5.81E+08	NO	126.29511	1641.8364	1.64183637	1.07
14	1641.8364	12399205	227629.84	12626835	5.81E+08	NO	126.29511	1768.1315	1.76813148	1.17
15	1768.1315	12856614	263996.73	13120611	5.81E+08	NO	126.29511	1894.4266	1.89442658	1.28
16	1894.4266	13330897	303057.48	13633955	5.81E+08	NO	126.29511	2020.7217	2.02072169	1.39
17	2020.7217	13822677	344812.06	14167489	5.81E+08	NO	126.29511	2147.0168	2.14701679	1.51
18	2147.0168	14332598	389260.49	14721858	5.81E+08	NO	126.29511	2273.3119	2.2733119	1.63
19	2273.3119	14861330	436402.76	15297733	5.81E+08	NO	126.29511	2399.607	2.399607	1.75
20	2399.607	15409567	486238.88	15895806	5.81E+08	NO	126.29511	2525.9021	2.52590211	1.88
21	2525.9021	15978029	538768.85	16516798	5.81E+08	NO	126.29511	2652.1972	2.65219722	2.02
22	2652.1972	16567462	593992.65	17161454	5.81E+08	NO	126.29511	2778.4923	2.77849232	2.16
23	2778.4923	17178638	651910.3	17830549	5.81E+08	NO	126.29511	2904.7874	2.90478743	2.30
24	2904.7874	17812362	712521.8	18524883	5.81E+08	NO	126.29511	3031.0825	3.03108253	2.45
25	3031.0825	18469463	775827.14	19245290	5.81E+08	NO	126.29511	3157.3776	3.15737764	2.61
26	3157.3776	19150805	841826.32	19992631	5.81E+08	NO	126.29511	3283.6727	3.28367274	2.77
27	3283.6727	19857282	910519.35	20767801	5.81E+08	NO	126.29511	3409.9678	3.40996785	2.94
28	3409.9678	20589821	981906.22	21571727	5.81E+08	NO	126.29511	3536.263	3.53626295	3.11
29	3536.263	21349383	1055986.9	22405370	5.81E+08	NO	126.29511	3662.5581	3.66255806	3.29
30	3662.5581	22136966	1132761.5	23269727	5.81E+08	NO	126.29511	3788.8532	3.78885317	3.48
31	3788.8532	22953603	1212229.9	24165833	5.81E+08	NO	126.29511	3915.1483	3.91514827	3.67
32	3915.1483	23800366	1294392.2	25094758	5.81E+08	NO	126.29511	4041.4434	4.04144338	3.87
33	4041.4434	24678366	1.38E+06	26057614	5.81E+08	NO	126.29511	4167.7385	4.16773848	4.08
34	4167.7385	25588755	1466798.2	27055553	5.81E+08	NO	126.29511	4294.0336	4.29403359	4.30
35	4294.0336	26532729	1557042	28089771	5.81E+08	NO	126.29511	4420.3287	4.42032869	4.52
36	4420.3287	27511527	1649979.6	29161506	5.81E+08	NO	126.29511	4546.6238	4.5466238	4.75
37	4546.6238	28526432	1745611.1	30272043	5.81E+08	NO	126.29511	4672.9189	4.6729189	4.99
38	4672.9189	29578778	1843936.4	31422714	5.81E+08	NO	126.29511	4799.214	4.79921401	5.24
39	4799.214	30669944	1944955.5	32614900	5.81E+08	NO	126.29511	4925.5091	4.92550912	5.50
40	4925.5091	31801364	2048668.5	33850033	5.81E+08	NO	126.29511	5051.8042	5.05180422	5.77
41	5051.8042	32974523	2155075.4	35129598	5.81E+08	NO	126.29511	5178.0993	5.17809933	6.05
42	5178.0993	34190959	2264176.1	36455135	5.81E+08	NO	126.29511	5304.3944	5.30439443	6.34
43	5304.3944	35452270	2375970.6	37828241	5.81E+08	NO	126.29511	5430.6895	5.43068954	6.64
44	5430.6895	36760111	2490459	39250570	5.81E+08	NO	126.29511	5556.9846	5.55698464	6.95
45	5556.9846	38116198	2607641.2	40723840	5.81E+08	NO	126.29511	5683.2797	5.68327975	7.27
46	5683.2797	39522312	2727517.3	42249830	5.81E+08	NO	126.29511	5809.5749	5.80957485	7.60
47	5809.5749	40980298	2850087.2	43830385	5.81E+08	NO	126.29511	5935.87	5.93586996	7.95
48	5935.87	42492069	2975350.9	45467420	5.81E+08	NO	126.29511	6062.1651	6.06216506	8.31
49	6062.1651	44059609	3103308.5	47162918	5.81E+08	NO	126.29511	6188.4602	6.18846017	8.68
50	6188.4602	45684977	3233960	48918937	5.81E+08	NO	126.29511	6314.7553	6.31475528	9.06
51	6314.7553	4.74E+07	3367305.3	50737609	5.81E+08	NO	126.29511	6441.0504	6.44105038	9.46
52	6441.0504	49117804	3503344.4	52621148	5.81E+08	NO	126.29511	6567.3455	6.56734549	9.88
53	6567.3455	50929769	3642077.4	54571846	5.81E+08	NO	126.29511	6693.6406	6.69364059	10.31
54	6693.6406	52808578	3783504.2	56592082	5.81E+08	NO	126.29511	6819.9357	6.8199357	10.75
55	6819.9357	54756696	3927624.9	58684321	5.81E+08	NO	126.29511	6946.2308	6.9462308	11.21
56	6946.2308	56776681	4074439.4	60851120	5.81E+08	NO	126.29511	7072.5259	7.07252591	11.69
57	7072.5259	58871183	4223947.7	63095131	5.81E+08	NO	126.29511	7198.821	7.19882101	12.19
58	7198.821	61042953	4376149.9	65419103	5.81E+08	NO	126.29511	7325.1161	7.32511612	12.71
59	7325.1161	63294839	4531046	67825885	5.81E+08	NO	126.29511	7451.4112	7.45141123	13.24
60	7451.4112	65629797	4688635.9	70318433	5.81E+08	NO	126.29511	7577.7063	7.57770633	13.79
61	7577.7063	68050893	4848919.6	72899813	5.81E+08	NO	126.29511	7704.0014	7.70400144	14.37
62	7704.0014	70561303	5011897.2	75573200	5.81E+08	NO	126.29511	7830.2965	7.83029654	14.96
63	7830.2965	73164323	5177568.6	78341892	5.81E+08	NO	126.29511	7956.5916	7.95659165	15.58
64	7956.5916	75863369	5345933.9	81209303	5.81E+08	NO	126.29511	8082.8868	8.08288675	16.22
65	8082.8868	78661983	5516993	84178976	5.81E+08	NO	126.29511	8209.1819	8.20918186	16.88
66	8209.1819	81563839	5690745.9	87254584	5.81E+08	NO	126.29511	8335.477	8.33547696	17.57
67	8335.477	84572744	5867192.7	90439937	5.81E+08	NO	126.29511	8461.7721	8.46177207	18.29
68	8461.7721	87692649	6046333.4	93738982	5.81E+08	NO	126.29511	8588.0672	8.58806718	19.03
69	8588.0672	87692649	6228167.9	93920816	5.81E+08	NO	126.29511	8714.3623	8.71436228	19.77
70	8714.3623	94162645	6412696.2	100575342	5.81E+08	NO	126.29511	8840.6574	8.84065739	20.56
71	8840.6574	97636323	6599918.4	104236242	5.81E+08	NO	126.29511	8966.9525	8.96695249	21.38
72	8966.9525	101238146	6789834.4	108027980	5.81E+08	NO	126.29511	9093.2476	9.0932476	22.24
73	9093.2476	104972840	6982444.2	111955284	5.81E+08	NO	126.29511	9219.5427	9.2195427	23.12
74	9219.5427	108845308	7177747.9	116023056	5.81E+08	NO	126.29511	9345.8378	9.34583781	24.04
75	9345.8378	112860632	7375745.5	120236378	5.81E+08	NO	126.29511	9472.1329	9.47213291	24.99
76	9472.1329	117024082	7576436.9	124600519	5.81E+08	NO	126.29511	9598.428	9.59842802	25.98
77	9598.428	121341123	7779822.1	129120945	5.81E+08	NO	126.29511	9724.7231	9.72472312	27.00
78	9724.7231	125817420	7985901.2	133803321	5.81E+08	NO	126.29511	9851.0182	9.85101823	28.07
79	9851.0182	130458849	8194674.1	138653523	5.81E+08	NO	126.29511	9977.3133	9.97731334	29.17
80	9977.3133	135271500	8406140.9	143677641	5.81E+08	NO	126.29511	10103.608	10.1036084	30.31
81	10103.608	140261692	8620301.5	148881993	5.81E+08	NO	126.29511	10229.904	10.2299035	31.49
82	10229.904	145435972	8837156	154273128	5.81E+08	NO	126.29511	10356.199	10.3561987	32.72
83	10356.199	150801133	9056704.3	159857837	5.81E+08	NO	126.29511	10482.494	10.4824938	33.99
84	10482.494	156364215	9278946.4	165643161	5.81E+08	NO	126.29511	10608.789	10.6087889	35.31
85	10608.789	162132521	9503882.4	171636403	5.81E+08	NO	126.29511	10735.084	10.735084	36.68
86	10735.084	168113620	9731512.3	177845132	5.81E+08	NO	126.29511	10861.379	10.8613791	38.10
87	10861.379	174315363	9961836	184277199	5.81E+08	NO	126.29511	10987.674	10.9876742	39.57
88	10987.674	180745890	10194853	190940744	5.81E+08	NO	126.29511	11113.969	11.1139693	41.09
89	11113.969	187413640	10430565	197844205	5.81E+08	NO	126.29511	11240.264	11.2402644	42.67
90	11240.264	194327365	10668970	204996335	5.81E+08	NO	126.29511	11366.559	11.3665595	44.31
91	11366.559	201496139	10910069	212406208	5.81E+08	NO	126.29511	11492.855	11.4928546	46.01
92	11492.855	208929369	11153862	220083231	5.81E+08	NO	126.29511	11619.15	11.6191497	47.78
93	11619.15	216636813	11400349	228037162	5.81E+08	NO	126.29511	11745.445	11.7454448	49.60
94	11745.445	224628587	11649529	236278116	5.81E+08	NO	126.29511	11871.74	11.8717399	51.50
95	11871.74	232915178	11901404	244816581	5.81E+08	NO	126.29511	11998.035	11.998035	53.46
96	11998.035	241507463	12155972	253663435	5.81E+08	NO	126.29511	12124.33	12.1243301	55.50
97	12124.33	250416719	12413234	262829953	5.81E+08	NO	126.29511	12250.625	12.2506252	57.61
98	12250.625	259654639	12673190	272327829	5.81E+08	NO	126.29511	12376.92	12.3769203	59.81
99	12376.92	269233348	12935840	282169188	5.81E+08	NO	126.29511	12503.215	12.5032154	62.08
100	12503.215	279165417	13201184	292366601	5.81E+08	NO	126.29511	12629.511	12.6295106	64.43
101	12629.511	289463883	13201184	302665066	5.81E+08	NO	126.29511	12755.806	12.7558057	66.87
102	12755.806	300142260	13739952	313882213	5.81E+08	NO	126.29511	12882.101	12.8821008	69.41
103	12882.101	311214565	14013378	325227943	5.81E+08	NO	126.29511	13008.396	13.0083959	72.03
104	13008.396	322695330	14289497	336984826	5.81E+08	NO	126.29511	13134.691	13.134691	74.75
105	13134.691	334599621	14568310	349167931	5.81E+08	NO	126.29511	13260.986	13.2609861	77.58
106	13260.986	346943065	14849816	361792881	5.81E+08	YES	126.29511	13387.281	13.3872812	80.50

Table: Driveability analysis results for sandstone 2 rock properties, 75° cutting angle and 91WC-9Co toe.

Blow no	Li (mm)	Fc (N)	Qs (N)	Freq (N)	Ftip (N)	Refusal	v (mm)	Li+1 (mm)	Li+1 (m)	w (mm)
0	0	0	0	0	0	0	0	0		0
1	0	7800945.1	0	7800945.1	580671431	NO	126.29511	126.295106	0.12629511	0.05386553
2	126.29511	7975621	1346.9221	7976967.9	580671431	NO	126.29511	252.590211	0.25259021	0.10893719
3	252.59021	8216418	5387.6885	8221805.7	580671431	NO	126.29511	378.885317	0.37888532	0.16567156
4	378.88532	8464485	12122.299	8476607.3	580671431	NO	126.29511	505.180422	0.50518042	0.22411882
5	505.18042	8720041.6	21550.754	8741592.3	580671431	NO	126.29511	631.475528	0.63147553	0.28433071
6	631.47553	8983313.8	33673.053	9016986.9	580671431	NO	126.29511	757.770633	0.75777063	0.34636049
7	757.77063	9254534.7	48489.196	9303023.9	580671431	NO	126.29511	884.065739	0.88406574	0.41026305
8	884.06574	9533944.1	65999.184	9599943.3	580671431	NO	126.29511	1010.36084	1.01036084	0.47609494
9	1010.3608	9821789.4	86203.015	9907992.4	580671431	NO	126.29511	1136.65595	1.13665595	0.5439144
10	1136.6559	10118325	109100.69	10227426	580671431	NO	126.29511	1262.95106	1.26295106	0.61378143
11	1262.9511	10423814	134692.21	10558506	580671431	NO	126.29511	1389.24616	1.38924616	0.68575787
12	1389.2462	10423814	162977.58	10586792	580671431	NO	126.29511	1515.54127	1.51554127	0.7577343
13	1515.5413	11053238	193956.78	11247195	580671431	NO	126.29511	1641.83637	1.64183637	0.83405691
14	1641.8364	11386953	227629.84	11614583	580671431	NO	126.29511	1768.13148	1.76813148	0.91268382
15	1768.1315	11730744	263996.73	11994740	580671431	NO	126.29511	1894.42658	1.89442658	0.9936846
16	1894.4266	12084914	303057.48	12387971	580671431	NO	126.29511	2020.72169	2.02072169	1.07713093
17	2020.7217	12449777	344812.06	12794589	580671431	NO	126.29511	2147.01679	2.14701679	1.16309664
18	2147.0168	12825656	389260.49	13214917	580671431	NO	126.29511	2273.3119	2.2733119	1.2516578
19	2273.3119	13212884	436402.76	13649286	580671431	NO	126.29511	2399.607	2.399607	1.34289276
20	2399.607	13611802	486238.88	14098041	580671431	NO	126.29511	2525.90211	2.52590211	1.43688225
21	2525.9021	14022764	538768.85	14561533	580671431	NO	126.29511	2652.19722	2.65219722	1.53370944
22	2652.1972	14446135	593992.65	15040127	580671431	NO	126.29511	2778.49232	2.77849232	1.63346
23	2778.4923	14882287	651910.3	15534197	580671431	NO	126.29511	2904.78743	2.90478743	1.73622219
24	2904.7874	15331607	712521.8	16044129	580671431	NO	126.29511	3031.08253	3.03108253	1.84208694
25	3031.0825	15794493	775827.14	16570321	580671431	NO	126.29511	3157.37764	3.15737764	1.95114792
26	3157.3776	16271355	841826.32	17113181	580671431	NO	126.29511	3283.67274	3.28367274	2.06350162
27	3283.6727	16762614	910519.35	17673133	580671431	NO	126.29511	3409.96785	3.40996785	2.17924747
28	3409.9678	17268704	981906.22	18250610	580671431	NO	126.29511	3536.26295	3.53626295	2.29848787
29	3536.263	17790075	1055986.9	18846061	580671431	NO	126.29511	3662.55806	3.66255806	2.42132834
30	3662.5581	18327186	1132761.5	19459947	580671431	NO	126.29511	3788.85317	3.78885317	2.54787756
31	3788.8532	18880513	1212229.9	20092743	580671431	NO	126.29511	3915.14827	3.91514827	2.6782475
32	3915.1483	19450547	1294392.2	20744939	580671431	NO	126.29511	4041.44338	4.04144338	2.81255353
33	4041.4434	20037790	1379248.2	21417039	580671431	NO	126.29511	4167.73848	4.16773848	2.95091447
34	4167.7385	20642764	1466798.2	22109562	580671431	NO	126.29511	4294.03359	4.29403359	3.09345276
35	4294.0336	21266003	1557042	22823045	580671431	NO	126.29511	4420.32869	4.42032869	3.2402945
36	4420.3287	21908058	1649979.6	23558037	580671431	NO	126.29511	4546.6238	4.5466238	3.39156964
37	4546.6238	22569498	1745611.1	24315109	580671431	NO	126.29511	4672.9189	4.6729189	3.54741202
38	4672.9189	23250908	1843936.4	25094844	580671431	NO	126.29511	4799.21401	4.79921401	3.70795954
39	4799.214	23952890	1944955.5	25897846	580671431	NO	126.29511	4925.50912	4.92550912	3.87335425
40	4925.5091	24676067	2048668.5	26724736	580671431	NO	126.29511	5051.80422	5.05180422	4.04374249
41	5051.8042	25421078	2155075.4	27576153	580671431	NO	126.29511	5178.09933	5.17809933	4.21927503
42	5178.0993	26188581	2264176.1	28452757	580671431	NO	126.29511	5304.39443	5.30439443	4.40010719
43	5304.3944	26979257	2375970.6	29355228	580671431	NO	126.29511	5430.68954	5.43068954	4.58639896
44	5430.6895	27793805	2490459	30284264	580671431	NO	126.29511	5556.98464	5.55698464	4.77831518
45	5556.9846	28632945	2607641.2	31240586	580671431	NO	126.29511	5683.27975	5.68327975	4.97602567
46	5683.2797	29497420	2727517.3	32224938	580671431	NO	126.29511	5809.57485	5.80957485	5.17970536
47	5809.5749	30387996	2850087.2	33238083	580671431	NO	126.29511	5935.86996	5.93586996	5.38953447
48	5935.87	31305459	2975350.9	34280810	580671431	NO	126.29511	6062.16506	6.06216506	5.60569866
49	6062.1651	32250621	3103308.5	35353930	580671431	NO	126.29511	6188.46017	6.18846017	5.8283892
50	6188.4602	33224320	3233960	36458280	580671431	NO	126.29511	6314.75528	6.31475528	6.05780313
51	6314.7553	34227416	3367305.3	37594722	580671431	NO	126.29511	6441.05038	6.44105038	6.29414344
52	6441.0504	35260798	3503344.4	38764142	580671431	NO	126.29511	6567.34549	6.56734549	6.53761925
53	6567.3455	36325379	3642077.4	39967456	580671431	NO	126.29511	6693.64059	6.69364059	6.78844599
54	6693.6406	37422101	3783504.2	41205605	580671431	NO	126.29511	6819.9357	6.8199357	7.04684559
55	6819.9357	38551935	3927624.9	42479560	580671431	NO	126.29511	6946.2308	6.9462308	7.31304671
56	6946.2308	39715881	4074439.4	43790320	580671431	NO	126.29511	7072.52591	7.07252591	7.58728486
57	7072.5259	40914968	4223947.7	45138916	580671431	NO	126.29511	7198.82101	7.19882101	7.86980271
58	7198.821	42150257	4376149.9	46526407	580671431	NO	126.29511	7325.11612	7.32511612	8.16085024
59	7325.1161	43422842	4531046	47953888	580671431	NO	126.29511	7451.41123	7.45141123	8.46068497
60	7451.4112	44733848	4688635.9	49422484	580671431	NO	126.29511	7577.70633	7.57770633	8.76957219
61	7577.7063	46084436	4848919.6	50933356	580671431	NO	126.29511	7704.00144	7.70400144	9.08778522
62	7704.0014	47475800	5011897.2	52487697	580671431	NO	126.29511	7830.29654	7.83029654	9.41560562
63	7830.2965	48909172	5177568.6	54086740	580671431	NO	126.29511	7956.59165	7.95659165	9.75332345
64	7956.5916	50385819	5345933.9	55731753	580671431	NO	126.29511	8082.88675	8.08288675	10.1012375
65	8082.8868	51907049	5516993	57424042	580671431	NO	126.29511	8209.18186	8.20918186	10.4596557
66	8209.1819	53474207	5690745.9	59164953	580671431	NO	126.29511	8335.47696	8.33547696	10.8288951
67	8335.477	55088681	5867192.7	60955874	580671431	NO	126.29511	8461.77207	8.46177207	11.2092825
68	8461.7721	56751898	6046333.4	62798231	580671431	NO	126.29511	8588.06718	8.58806718	11.6011543
69	8588.0672	56751898	6228167.9	62980066	580671431	NO	126.29511	8714.36228	8.71436228	11.9930262
70	8714.3623	60178762	6412696.2	66591458	580671431	NO	126.29511	8840.65739	8.84065739	12.4085605
71	8840.6574	61995657	6599918.4	68595575	580671431	NO	126.29511	8966.95249	8.96695249	12.8366405
72	8966.9525	63867407	6789834.4	70657241	580671431	NO	126.29511	9093.2476	9.0932476	13.277645
73	9093.2476	65795668	6982444.2	72778112	580671431	NO	126.29511	9219.5427	9.2195427	13.731964
74	9219.5427	67782146	7177747.9	74959894	580671431	NO	126.29511	9345.83781	9.34583781	14.1999998
75	9345.8378	69828599	7375745.5	77204345	580671431	NO	126.29511	9472.13291	9.47213291	14.6821662
76	9472.1329	71936838	7576436.9	79513275	580671431	NO	126.29511	9598.42802	9.59842802	15.1788901
77	9598.428	74108728	7779822.1	81888551	580671431	NO	126.29511	9724.72312	9.72472312	15.6906109
78	9724.7231	76346191	7985901.2	84332093	580671431	NO	126.29511	9851.01823	9.85101823	16.2177813
79	9851.0182	78651207	8194674.1	86845881	580671431	NO	126.29511	9977.31334	9.97731334	16.7608679
80	9977.3133	81025815	8406140.9	89431956	580671431	NO	126.29511	10103.6084	10.1036084	17.3203512
81	10103.608	83472116	8620301.5	92092418	580671431	NO	126.29511	10229.9035	10.2299035	17.8967261
82	10229.904	85992275	8837156	94829431	580671431	NO	126.29511	10356.1987	10.3561987	18.4905028
83	10356.199	88588522	9056704.3	97645226	580671431	NO	126.29511	10482.4938	10.4824938	19.1022065
84	10482.494	91263154	9278946.4	100542100	580671431	NO	126.29511	10608.7889	10.6087889	19.7323786
85	10608.789	94018537	9503882.4	103522419	580671431	NO	126.29511	10735.084	10.735084	20.3815766
86	10735.084	96857110	9731512.3	106588622	580671431	NO	126.29511	10861.3791	10.8613791	21.050375
87	10861.379	99781383	9961836	109743219	580671431	NO	126.29511	10987.6742	10.9876742	21.7393654
88	10987.674	102793946	10194853	112988799	580671431	NO	126.29511	11113.9693	11.1139693	22.4491576
89	11113.969	105897462	10430565	116328027	580671431	NO	126.29511	11240.2644	11.2402644	23.1803796
90	11240.264	109094679	10668970	119763649	580671431	NO	126.29511	11366.5595	11.3665595	23.9336783
91	11366.559	112388425	10910069	123298494	580671431	NO	126.29511	11492.8546	11.4928546	24.7097204
92	11492.855	115781614	11153862	126935476	580671431	NO	126.29511	11619.1497	11.6191497	25.5091925
93	11619.15	119277250	11400349	130677598	580671431	NO	126.29511	11745.4448	11.7454448	26.3328019
94	11745.445	122878424	11649529	134527953	580671431	NO	126.29511	11871.7399	11.8717399	27.1812774
95	11871.74	126588324	11901404	138489727	580671431	NO	126.29511	11998.035	11.998035	28.0553698
96	11998.035	130410231	12155972	142566203	580671431	NO	126.29511	12124.3301	12.1243301	28.9558524
97	12124.33	134347528	12413234	146760762	580671431	NO	126.29511	12250.6252	12.2506252	29.8835221
98	12250.625	138403699	12673190	151076889	580671431	NO	126.29511	12376.9203	12.3769203	30.8391996
99	12376.92	142582332	12935840	155518172	580671431	NO	126.29511	12503.2154	12.5032154	31.8237306
100	12503.215	146887124	13201184	160088308	580671431	NO	126.29511	12629.5106	12.6295106	32.8379862
101	12629.511	151321885	13469221	164791107	580671431	NO	126.29511	12755.8057	12.7558057	33.8828638
102	12755.806	155890539	13739952	169630492	580671431	NO	126.29511	12882.1008	12.8821008	34.959288
103	12882.101	160597129	14013378	174610506	580671431	NO	126.29511	13008.3959	13.0083959	36.0682112
104	13008.396	165445817	14289497	179735314	580671431	NO	126.29511	13134.691	13.134691	37.2106146
105	13134.691	170440896	14568310	185009205	580671431	NO	126.29511	13260.9861	13.2609861	38.3875089
106	13260.986	175586784	14849816	190436600	580671431	NO	126.29511	13387.2812	13.3872812	39.5999357
107	13387.281	180888034	15134017	196022051	580671431	NO	126.29511	13513.5763	13.5135763	40.8489676
108	13513.576	186349339	15420911	201770250	580671431	NO	126.29511	13639.8714	13.6398714	42.1357097
109	13639.871	191975528	15710500	207686028	580671431	NO	126.29511	13766.1665	13.7661665	43.4613008
110	13766.167	197771582	16002782	213743364	580671431	NO	126.29511	13892.4616	13.8924616	44.8269135
111	13892.462	203742628	16297758	220040385	580671431	NO	126.29511	14018.7567	14.0187567	46.2337564
112	14018.757	209893949	16595427	226489377	580671431	NO	126.29511	14145.0518	14.1450518	47.6830741
113	14145.052	216230989	16895791	233126780	580671431	NO	126.29511	14271.3469	14.2713469	49.1761491
114	14271.347	222759355	17198848	239958203	580671431	NO	126.29511	14397.642	14.397642	50.7143024
115	14397.642	229484822	17504600	246989422	580671431	NO	126.29511	14523.9371	14.5239371	52.2988951
116	14523.937	236413342	17813045	254226387	580671431	NO	126.29511	14650.2322	14.6502322	53.9313293
117	14650.232	243551046	18124184	261675230	580671431	NO	126.29511	14776.5273	14.7765273	55.6130492
118	14776.527	250904248	18438017	269342265	580671431	NO	126.29511	14902.8225	14.9028225	57.3455431
119	14902.822	258479456	18754544	277234000	580671431	YES	126.29511	15029.1176	15.0291176	59.1303437

Table: Driveability analysis results for sandstone 2 rock properties, 75° cutting angle and 97WC-3Co toe.

B4: Derivation: Vertical Crack in Rock Cutting

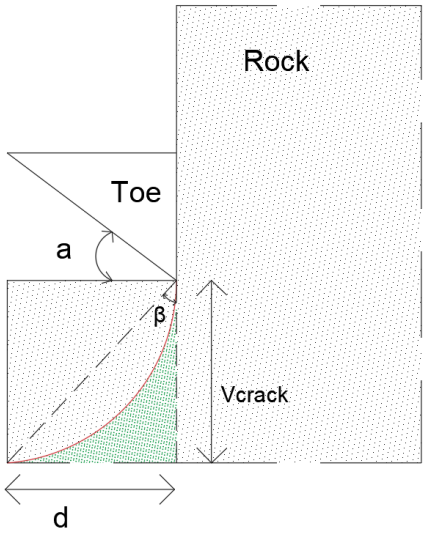

Rock cutting force by Evans:

$$F_c = \frac{\sigma_t * w * d * \sin\left(\frac{\pi}{4} - \frac{\alpha}{2} + \varphi\right)}{\sin\beta \cos\left(\frac{\pi}{4} - \frac{\alpha}{2} + \varphi + \beta\right)}$$

where, φ is the friction between tool and rock, w is the width of the tool, σ_t is the tensile strength of rock

According to the principle of minimum energy:

$$\frac{\partial F_c}{\partial \beta} = 0 => \frac{-c\left(\cos\beta \cos\left(\frac{\pi}{4} - \frac{\alpha}{2} + \varphi + \beta\right) - \sin\beta \sin\left(\frac{\pi}{4} - \frac{\alpha}{2} + \varphi + \beta\right)\right)}{\sin\beta \cos\left(\frac{\pi}{4} - \frac{\alpha}{2} + \varphi + \beta\right)} = 0$$

$$=> \cos\beta \cos\left(\frac{\pi}{4} - \frac{\alpha}{2} + \varphi + \beta\right) - \sin\beta \sin\left(\frac{\pi}{4} - \frac{\alpha}{2} + \varphi + \beta\right) = 0$$

$$=> \cos\left(2\beta + \frac{\pi}{4} - \frac{\alpha}{2} + \varphi\right) = 0$$

$$=> \beta = \frac{1}{2}\left(\frac{\pi}{4} + \frac{\alpha}{2} - \varphi\right)$$

where, $c = \sigma_t * w * d * \sin\left(\frac{\pi}{4} - \frac{\alpha}{2} + \varphi\right)$

$$\tan\beta = \frac{d}{v_{crack}} => v_{crack} = \frac{d}{\tan\beta} = \left[\frac{F_C\left(1 - \sin\left(\frac{\pi}{4} - \frac{\alpha}{2} + \varphi\right)\right)}{2\sigma_t w \sin\left(\frac{\pi}{4} - \frac{\alpha}{2} + \varphi\right)}\right] * \frac{1}{\tan\beta}$$

B5: Derivation: Pile Tip Force

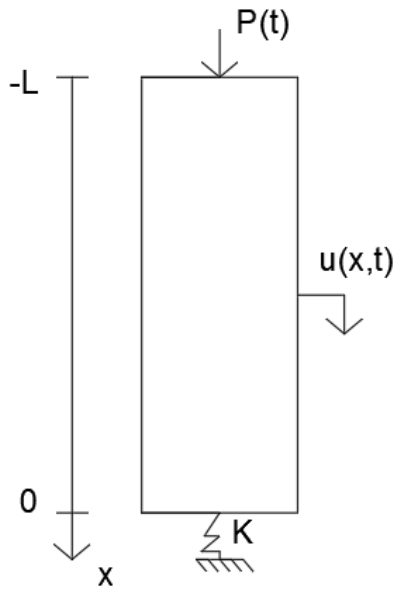

D'Alembert solution:

$$u = f(t - x/c) + g\left(t + \frac{x}{c}\right) = f(\tau^+) + g(\tau^-)$$

The spatial derivative is calculated:

$$\frac{\partial u}{\partial x} = \frac{\partial f}{\partial \tau^+} * \frac{\partial \tau^+}{\partial x} + \frac{\partial g}{\partial \tau^-} * \frac{\partial \tau^-}{\partial x} = \frac{\partial f}{\partial \tau^+} * \left(-\frac{1}{c}\right) + \frac{\partial g}{\partial \tau^-} * \left(\frac{1}{c}\right)$$

$$=> \frac{\partial u}{\partial x} = \frac{1}{c}\left(-\frac{\partial f}{\partial \tau^+} + \frac{\partial g}{\partial \tau^-}\right)$$

As mentioned in chapter 6.1, the time needed for the reflected wave to reach the top of the pile is t=0.038s. The duration of the pulse is t=0.0072s, meaning that the pulse can fully develop without interacting with the reflected wave.

Boundary condition at x=-L:

$$P(t) = -EA\frac{\partial u}{\partial x}|_{x=-L} => P(t) = \frac{EA}{c}\frac{\partial f(\tau^+)}{\partial t}|_{x=-L}$$

$$=> P(t) = \frac{EA}{c}\frac{\partial f(\tau^+)}{\partial t}|_{\hat{x}=0} = \frac{EA}{c}\frac{\partial f(t)}{\partial t} => f(t) = \frac{c}{EA}\int_0^t P(t)$$

*shift of coordinate system $\hat{x} = x - L$

Boundary condition at x=0:

$$EA\frac{\partial u}{\partial x}|_{x=0} + K * u|_{x=0} = 0 => \frac{EA}{c}\left(-\frac{\partial f}{\partial \tau^+} + \frac{\partial g}{\partial \tau^-}\right)|_{x=0} + K * \left(f(\tau^+) + g(\tau^-)\right)|_{x=0} = 0$$

$$=> Z\left(-\frac{\partial f(t)}{\partial t} + \frac{\partial g(t)}{\partial t}\right) + K * \left(f(t) + g(t)\right) = 0$$

$$=> \frac{\partial g(t)}{\partial t} + \frac{K}{Z}g(t) = \frac{\partial f(t)}{\partial t} - \frac{K}{Z}f(t)$$

The general solution to the equation above can be found below, considering that g(t)=f(t)=0 for t=0:

$$=> g(t) = \int_0^t \left(\frac{\partial f(\tau)}{\partial \tau} - \frac{K}{Z}f(\tau)\right)e^{-\frac{K}{Z}(t-\tau)}d\tau$$

$$=> g(t) = f(t) - \frac{2K}{Z}\int_0^t f(\tau)e^{-\frac{K}{Z}(t-\tau)}d\tau$$

where, Z is the impedance

Therefore, the D'Alembert solution is now known. Then, the pile tip force is equal to:

$$F_{tip} = EA\frac{\partial u}{\partial x}|_{x=0}$$

B6: GMNIA for granite properties

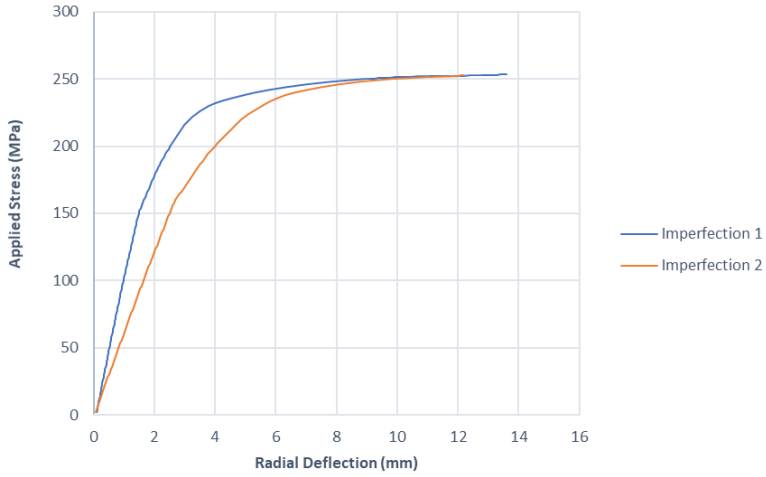

Graph: Non-linear buckling analysis for monopile-granite interaction, including rock borehole.

B7: GMNIA results for different imperfections

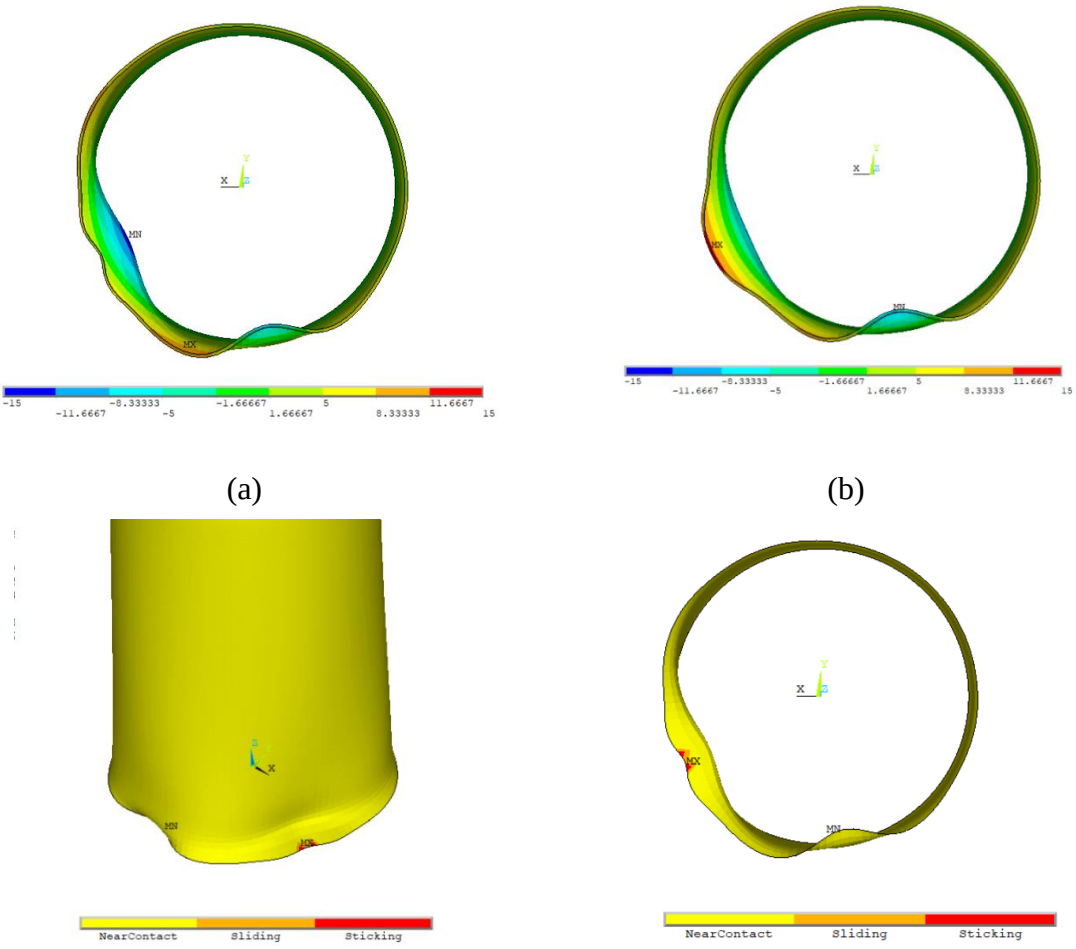

(a) (b)

(c)

Figure: 1st Imperfection GMNIA radial deflection results (mm). Including rock borehole (a). Without rock in the model (b). Rock-monopile contact status at the critical load (c).

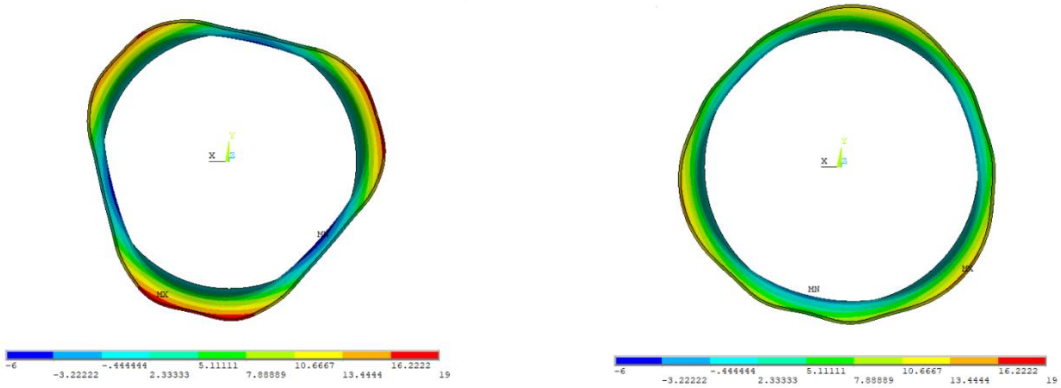

(a) (b)

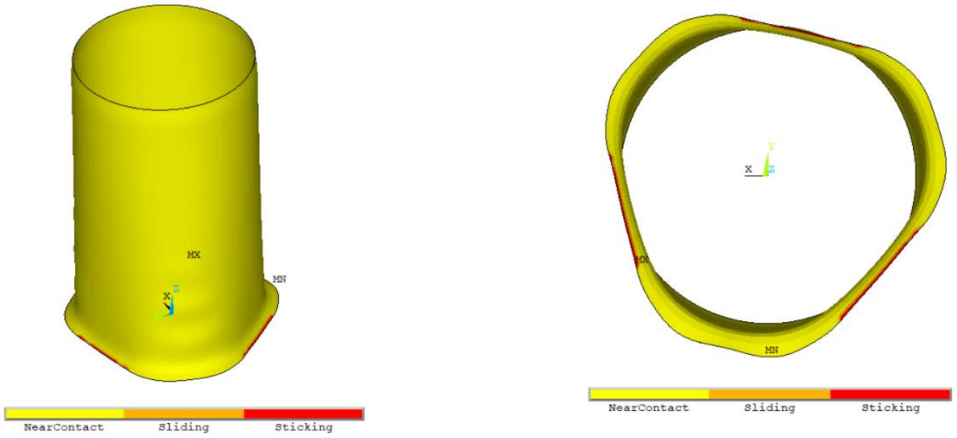

(c)

Figure: 4th Imperfection GMNIA radial deflection results (mm). Including rock borehole (a). Without rock in the model (b). Rock-monopile contact status at the critical load (c).

B8: Mesh sensitivity analysis of the toe-rock interaction model

In order to determine the appropriate size of the mesh, that would yield accurate results, a mesh sensitivity analysis was conducted for the axisymmetric ANSYS model of the toe penetrating the rock. An initial mesh size of 0.5x0.5mm was chosen for the rock mass below the toe tip. This size was reduced in half successively, and the resulting stiffness of the rock cutting operation was determined for each mesh size. The graph below shows that for each size step, a smaller than 1% reduction in stiffness occurs. Therefore, the initial mesh size of 0.5x0.5mm was selected. It is noted that at each size step the mesh of the toe tip is also reduced accordingly, creating a matching mesh for the two surfaces in contact.

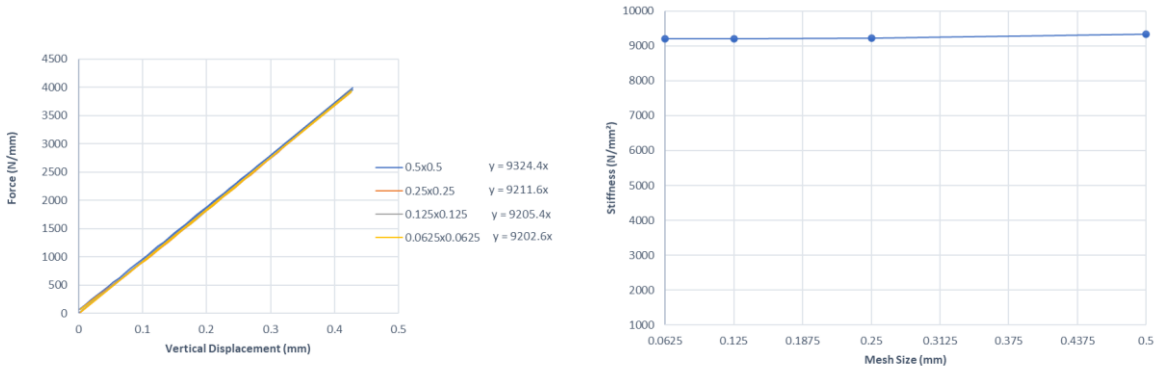

(a) (b)

Graph: Stiffness of the rock cutting operation for different rock mesh sizes.

B9: Mesh sensitivity analysis of the monopile

The appropriate mesh size for the buckling analysis of the monopile was investigated by gradually reducing it and comparing the results of eigen-buckling ANSYS analysis. In all cases, two elements over the monopile thickness were modelled. Linear spring elements with a stiffness of 500 kN/mm were attached in the circumference of the bottom cross-section. The results showed that a 200x200 mm mesh size is sufficiently small for the prediction of the local buckling behaviour.

Mesh size (mm)	Critical Buckling stress (Mpa)
200x200	1093.2
100x100	1093.3
50x50	1095.2

Table: Critical buckling stress for different mesh sizes